Politecnico di Torino

University of Colorado Boulder

Politecnico di Torino

Master of Science in Aerospace Engineering

A.a. 2025/2026

Graduation Session March 2026

Multi-Physics Modeling of Polymer Degradation: From Terrestrial Photo-Oxidation to Space Environment Erosion

Supervisors:
Prof. Alfonso Pagani
Prof. Maryam Shakiba

Candidate:
Giuseppe Caramanno

Abstract

This thesis is situated at the critical intersection between the physico-chemical understanding of degradation mechanisms in polymers and polymer composites and the development of robust constitutive models capable of predicting their physico-chemical and chemo-mechanical behavior across scales in aggressive space environments.

Environmental degradation, specifically UV photo-oxidation and erosion due to atomic oxygen (AO) in Low Earth Orbit (LEO), fundamentally alters the material's microstructural state, which in turn governs its mechanical performance. Consequently, accurate lifetime prediction requires a unified framework that explicitly couples these distinct degradation mechanisms. Following an introductory overview highlighting the industrial strategic relevance of these materials, the environmental degradation challenges, and the limitations of current empirical modeling approaches, the dissertation is organized into two distinct parts, each addressing a specific class of materials and degradation mechanisms.

Part I presents a comprehensive study on Low-Density Polyethylene (LDPE), selected as a fundamental prototype for semi-crystalline polymers. First, a novel physico-chemical model is introduced to resolve existing gaps in understanding the mass loss kinetics in nanometric range during photo-oxidation. Subsequently, this framework is extended to develop a thermodynamic constitutive model capable of capturing not only the viscoelastic response of this class of material, but also the fracture mechanics evolution under oxidative aging conditions.

Part II addresses material response in the Space extreme environment, focusing on polyhedral oligomeric silsesquioxane (POSS)-Polyimide nanocomposites. Here, a predictive model is developed to describe the unique self-passivation mechanism, where AO erosion in LEO triggers the formation of a protective silica shield. While validated on POSS-based systems, this modeling framework offers a generalized approach applicable to any material class exhibiting similar self-defense principles.

Experimental validation against literature datasets for LDPE, as well as in-situ flight records (MISSE-6) and ground experiments for POSS-polyimide, demonstrates the superior accuracy of these physics-based formulations compared to classical kinetic and empirical approaches. Ultimately, this thesis provides a set of validated computational tools that enable the design of polymer components with optimized durability for next-generation engineering and aerospace applications.

Acknowledgements

My sincere thanks go to my advisor, Prof. Alfonso Pagani, for his expert guidance during my academic journey at Politecnico di Torino. I am equally indebted to my co-advisor, Prof. Maryam Shakiba, for her outstanding mentorship and for welcoming me into the Mechanics of Complex Materials Lab at the University of Colorado Boulder. I also wish to acknowledge the entire research group for their unwavering support and for providing a highly dynamic and stimulating scientific environment.

A Mancuso. Sei con me ogni giorno.

Table of Contents

List of Figures

List of Tables

List of Abbreviations

Acronym	Definition
AO	Atomic Oxygen
DLO	Diffusion-Limited Oxidation
DSC	Differential Scanning Calorimetry
FEA	Finite Element Analysis
FEM	Finite Element Method
ISS	International Space Station
JWST	James Webb Space Telescope
LDPE	Low-Density Polyethylene
LEO	Low Earth Orbit
MD	Molecular Dynamics
MISSE	Materials International Space Station Experiment
MLI	Multi-Layer Insulation
M_w	Molecular Weight
ODE	Ordinary Differential Equation
PDE	Partial Differential Equation
PEEK	Polyaryletherketones
PE	Polyethylene
PI	Polyimide
POSS	Polyhedral Oligomeric Silsesquioxane
QCM-D	Quartz Crystal Microbalance With Dissipation
QSS	Quasi Steady-State
SLS	Standard Linear Solid
T_c	Ceiling Temperature
T_g	Glass Transition Temperature
T_m	Melting Temperature
UV	Ultraviolet
VLEO	Very-Low Earth Orbit

Chapter 1

Introduction

1.1 Polymer Composites in Modern Industry

Over the past several decades, the global industrial landscape has witnessed an exponential surge in interest towards the field of polymers and polymer composites. This trend spans across critical sectors, ranging from transport and civil construction to aerospace, defense and biomedical applications [1–5].

The reasons behind this surge in interest for such a specific class of materials are explained by the increasing demand for materials with superior performance. Historically, the drive to develop materials with enhanced mechanical strength, thermal stability, and chemical resistance, combined with a critical reduction in weight, has been the catalyst for the enormous development of composite materials. The underlying concept is straightforward: to combine two or more distinct constituents to create, through their synergistic effects, a composite with properties far superior to those of the individual components alone.

There is a broad consensus in the scientific literature that the pivotal moment for the development of this class of materials, which effectively determined their future trajectory, was World War II [2, 6, 7]. The urgent military demand for high-performance, lightweight materials accelerated research and production capabilities, serving as the definitive starting point for modern composites. In the immediate post-war era, this technology rapidly transferred from military to civilian applications, triggering a global expansion into major industrial sectors, most notably automotive and transportation. This widespread adoption was primarily driven by the need for high strength-to-weight ratios and corrosion resistance, which remain the key drivers for their ubiquity in modern vehicle manufacturing [3].

However, it is imperative to mention that the extensive industrial research into this class of materials is not driven solely by performance. Especially in the context of modern industry, the focus has broadened to align with the era of sustainable

technologies and ecological stewardship [8]. Consequently, the development of these materials is now inextricably linked to the strict requirements for environmental compliance. In fact, despite their high cost [9], these materials are highly sought-after because they align with circular economy principles, offering innovative pathways for reprocessing that satisfy the dual demand for high performance and environmental responsibility [10, 11]. Beyond these sustainability and initial performance metrics, the operational viability of any structural material is ultimately dictated by its long-term durability. Consequently, another crucial aspect, which will be extensively analyzed in this work, is the capability of polymers and composites to resist severe environmental degradation and "corrosion" phenomena. While traditional metallic structures are primarily plagued by electrochemical oxidation, polymers face a different set of aggressive physicochemical challenges, such as ultraviolet (UV) photo-oxidation, hydrolytic aging, and, particularly in space applications, erosion by atomic oxygen (AO) and outgassing effects. The intrinsic resilience of specific polymer matrices to these factors is the enabling factor that permits their utilization in extremely adverse operating environments, where traditional materials would rapidly fail or require heavy, impractical protective coatings [12, 13].

However, whether employed as standalone bulk materials or as the continuous phase in traditional fiber-reinforced composites, the base polymeric matrix remains highly vulnerable. Prolonged exposure to such extreme conditions inevitably leads to severe embrittlement or macroscopic mass loss, compromising the overall structural integrity. To bridge this performance gap, a key driver of modern materials innovation has been the introduction and subsequent development of nanocomposites. The transition from traditional macro- or micro-scale reinforcements to nanoparticles marks a paradigm shift in composite design. Due to their exceptionally high surface-area-to-volume ratio, nanoscale fillers can fundamentally alter the polymer network's behavior at very low volume fractions, avoiding the undesirable weight penalties associated with conventional fillers [14–16]. The incorporation of these nanoscale fillers serves a dual purpose. First, it significantly enhances the bulk chemo-mechanical properties of the base matrix, improving stiffness, thermal stability, and fracture toughness by restricting polymer chain mobility at the molecular level. Second, and crucially for the scope of this thesis, it enables the creation of active self-defense mechanisms against degradation [16]. Rather than acting merely as passive structural reinforcements or simple physical barriers against diffusion, specific nanoparticles, such as Polyhedral Oligomeric Silsesquioxanes (POSS) or other inorganic compounds, can dynamically interact with the aggressive environment. Upon the degradation of the outermost polymer layer, these nanofillers accumulate at the surface and undergo chemical transformations (e.g., oxidation) to form a continuous, ceramic-like passivation layer. This in-situ formed shield effectively blocks the further penetration of oxidative species and radiant energy into the bulk material, granting the composite an unprecedented, "smart" resistance

to environmental erosion.

1.2 Polymeric Systems and Architectures

Formally defined as composite materials in which at least one constituent is a polymer, polymer composites can be generally identified as a plastic continuous organic medium within which fibers or particles are embedded. In the vast majority of these systems, the polymer functions as the continuous matrix, while the discrete phase dispersed within it, whether fibers or particles, is referred to as the reinforcement. In this context, particular emphasis must be placed on the extensive variety of polymers available to serve as the matrix phase. The intrinsic versatility of these materials allows the selection to be tailored to a broad spectrum of design requirements, ranging from production costs and manufacturing techniques to the compatibility with specific reinforcement types and the environmental conditions expected during service [17–20].

Generally, polymer matrices are classified into two distinct categories based on their response to thermal stimuli and molecular architecture: thermosets and thermoplastics.

- *Thermosetting polymers (e.g., Epoxies, Phenolics, Polyurethanes)* are characterized by an irreversible polymerization process, known as curing, which transforms low-molecular-weight precursors into a rigid, three-dimensional covalently cross-linked network. Unlike thermoplastics, which rely on weak secondary intermolecular forces that temporarily dissociate upon heating, enabling the material to melt and flow, the cross-linking density in thermosets results in a theoretically infinite molecular weight, rendering the material infusible and insoluble [21, 22]. This specific molecular topology underpins their historical dominance in structural aerospace applications: the rigid network inhibits chain slippage, providing superior dimensional stability, high glass transition temperatures (T_g), and exceptional resistance to creep under sustained loads. However, this inherent chemical stability poses a significant limitation regarding end-of-life management; since the covalent network cannot be thermally dissociated without degradation, these materials are intractable and present severe challenges for recycling and reprocessing [23].
- *Thermoplastic polymers (e.g., Polyaryletherketones (PAEK/PEEK), Polyimides (PI), Polyethylene (PE))* consist of linear or branched macromolecular chains associated through weak intermolecular forces (e.g., Van der Waals forces, hydrogen bonding) and physical entanglements, devoid of permanent chemical cross-links. This topological freedom allows for a reversible phase transition: upon heating above their melting temperature (T_m) or glass transition (T_g), the thermal energy overcomes these secondary interactions, inducing

a transition from a solid to a viscous fluid state suitable for shaping [24] (it is however worth noting that certain high-performance pseudo-thermoplastics, such as traditional Polyimides, possess such extreme chain rigidity that their degradation temperature precedes their theoretical melting point, rendering them infusible). Mechanically, this structure imparts superior ductility and fracture toughness compared to brittle thermosets, as the chains can undergo significant plastic deformation and energy dissipation mechanisms (e.g., crazing or shear yielding) before failure. From an industrial perspective, this melt-processability not only facilitates rapid manufacturing techniques (e.g., injection molding, thermoforming) but also enables material recovery and recycling, aligning with modern sustainability requirements and circular economy principles [25].

Consequently, in recent years, the focus of the aerospace sector has increasingly shifted towards *high-performance thermoplastics*, such as PI and PEEK. These materials represent a strategic compromise, combining the manufacturing versatility of plastics with thermal stability and mechanical performance that, particularly in terms of strength-to-weight ratio, are comparable to metallic alloys [26, 27]. This trend is driven by the need to reduce structural mass without compromising integrity under extreme operating conditions.

While the choice of the matrix dictates the processability and thermal limit of the material, the ultimate performance of the composite is strictly dependent on the nature of the reinforcement and, more importantly, on its length scale.

Traditional composites (e.g., glass or carbon fiber reinforced polymers) rely on macroscopic reinforcements (micrometer scale). In these systems, the property enhancement is primarily mechanical and follows the classical *rule of mixtures* [28, 29]. According to the Voigt upper-bound model (iso-strain condition), the effective property of the composite, such as the elastic modulus (E_c), is predicted as the volume-weighted average of the constituent phases:

$$E_c = V_f E_f + (1 - V_f) E_m \tag{1.1}$$

where V_f is the fiber volume fraction, and E_f and E_m are the moduli of the fiber and matrix, respectively. This linear relationship assumes that the *interphase* region, the contact zone between filler and matrix, has a negligible volume compared to the bulk material. While this assumption holds true for macroscopic fibers, it breaks down for nanocomposites, where the ultra-high, specific surface area of the filler, typically orders of magnitude larger than that of its macroscopic counterparts, makes the interphase region a dominant factor in determining the final properties [30].

For these reasons, a paradigm shift occurs when the filler dimensions are reduced to the nanometer range. In polymer nanocomposites, the dramatic increase in

the surface-to-volume ratio of the nanofillers creates a massive interfacial area (or 'interphase') between the polymer and the particle. It is within this interaction zone that the bulk properties of the polymer are fundamentally altered. Even at very low loading fractions (typically $1 - 5\,wt\%$), nanofillers can impart functionalities, such as fire retardancy, gas barrier properties, and atomic oxygen resistance, that are unattainable with traditional micro-fillers, without compromising the lightweight nature of the host matrix [14].

1.3 Environmental Degradation: Mechanisms and Classification

Polymeric materials, despite their inherent durability, are susceptible to degradation when exposed to environmental stresses. This phenomenon is broadly defined as any irreversible evolution of the polymer structure, typically involving the scission of the macromolecular backbone, the alteration of pendant side groups or changes in cross-linking density. Ultimately, these molecular-level alterations translate into a reduction in molecular weight and the loss of critical macroscopic performance, ranging from mechanical strength to optical clarity, thereby compromising the material's service life [31–33]. From a phenomenological standpoint, degradation processes are traditionally categorized based on the nature of the primary external stressor driving the molecular alteration. The principal modes identified in the literature will be defined in the following part of this chapter.

1.3.1 Degradation Modes

Thermal Degradation

Thermal degradation is one of the most common failure modes, occurring when the polymer is exposed to temperatures exceeding the dissociation energy of its chemical bonds [34, 35]. The kinetic energy supplied by heat induces strong molecular vibrations that can lead to homolytic chain scission, generating highly reactive free radicals. This is particularly critical during processing or in high-temperature applications (e.g., engines, fire scenarios). This process can proceed via different pathways:

- *Depolymerization:* Often referred to as "unzipping", this mechanism involves the sequential detachment of monomeric units from the chain ends. It represents the thermodynamic reverse of the propagation reaction and occurs when the ceiling temperature (T_c) is exceeded.
- *Random Scission:* The backbone breaks at random points, causing a rapid decrease in molecular weight and mechanical strength (typical of Polyethylene).

The presence of oxygen at high temperatures accelerates this process significantly (thermo-oxidation), often acting as a catalyst for the formation of hydroperoxides, highly unstable intermediates that readily decompose to generate new free radicals, thereby driving an auto-accelerating degradation cycle.

Hydrolytic Degradation

Moisture plays a dual role in polymer aging: physical plasticization (reversible) and chemical hydrolysis (irreversible) [36]. *Hydrolysis* is a reaction where water molecules attack chemical bonds within the polymer backbone, leading to chain cleavage and a permanent reduction in mechanical properties [37]. This mechanism is particularly relevant for hetero-chain polymers containing functional groups such as esters, amides, and notably polyimides. Polyimides are known to be hygroscopic; absorbed water molecules can attack the imide ring, causing the opening of the ring and the reduction of the molecular weight. While this chemical degradation mechanism is crucial for biodegradable plastics, it inevitably leads to a severe loss of mechanical strength in structural engineering polymers, ultimately causing premature failure in humid environments. This sensitivity to moisture is a critical design factor, although modern aerospace grades (e.g., fluorinated polyimides) are chemically engineered to minimize this susceptibility by increasing hydrophobicity [26].

Chemical and Biological Degradation

Beyond water, polymers can interact with a wide range of aggressive substances (acids, bases, organic solvents). This interaction may be purely physical, such as the absorption of solvents causing swelling and plasticization based on solubility parameters [38], or strictly chemical, where aggressive agents cause bond scission, dissolution, or environmental stress cracking [39].

In terrestrial environments, *biodegradation* is also a relevant pathway, where the polymer acts as a carbon substrate for microorganisms, such as bacteria and fungi. This process is driven by extracellular enzymes that catalyze the hydrolysis and oxidation of the polymer backbone into lower molecular weight oligomers [40]. While crucial for the environmental sustainability of plastics on Earth, biological attack is kinetically inhibited in the external space environment due to the vacuum and extreme radiation, which prevent active microbial metabolism outside the spacecraft.

Mechanical Degradation

Mechanical degradation is induced by macroscopic stress (e.g., shear, tension, fatigue), where the input of mechanical energy can directly rupture molecular chains

(mechanochemistry) or accelerate other degradation modes like stress-cracking [33].

To conclude this classification, it is necessary to introduce the degradation pathways driven by high-energy radiation and extreme space-environmental interactions. These specific mechanisms, that will be discussed in detail in the respective parts and chapters of the thesis, constitute the core focus of this research work and are detailed in the following paragraphs.

Photo-oxidative and Radiolytic Degradation:

This degradation mode is driven by the absorption of high-energy radiation, ranging from UV light to gamma rays. The absorbed energy excites electrons within the polymer chains, generating free radicals that, in the presence of oxygen, initiate a self-sustaining auto-oxidation cycle known as the Bolland-Gee mechanism [41]. As will be extensively modeled in *Part I*, this process results in the scission of the macromolecular backbone. In semi-crystalline polymers, this chain scission triggers a phenomenon known as *chemo-crystallization*, where the cleaved chains reorganize into new crystalline domains. This leads to a paradoxical increase in density accompanied by severe mechanical embrittlement, a critical failure mode for structural integrity.

Atomic Oxygen Erosion

While thermal and photo-oxidative mechanisms typically drive bulk degradation, polymers operating in Low Earth Orbit (LEO) and Very-Low Earth Orbit (VLEO) are subject to a distinct, surface-limited phenomenon known as *AO erosion*. This degradation mode is caused by the bombardment of the spacecraft surface by high-energy oxygen atoms (~ 5 eV). Unlike the diffusive processes described above, AO attack results in "erosive oxidation": a combination of chemical reaction and physical sputtering that removes material layer-by-layer. This leads to macroscopic surface recession, mass loss, and changes in surface morphology (roughening). Since this specific mechanism represents a unique challenge requiring dedicated modeling approaches, a comprehensive analysis of the LEO environment challenges and the physics of AO interaction is provided in the theoretical background of *Part II* of this thesis.

1.4 The Need for Predictive Modeling

The widespread integration of advanced polymeric systems into critical engineering sectors is fundamentally contingent upon the ability to guarantee their reliability over extended timeframes. Regardless of the specific application, ranging from energy infrastructure to aerospace structures, a dramatic disparity exists between the required service life, often spanning several decades, and the feasible duration of laboratory qualification. Consequently, bridging this gap through the development of robust *lifetime prediction* methodologies has become a primary engineering challenge.

1.4.1 Limitations of Empirical Approaches

Historically, the estimation of polymer durability has relied heavily on empirical or semi-empirical correlations. The most ubiquitous method involves *accelerated aging tests*, where materials are exposed to elevated stress levels (temperature, irradiance, concentration) to speed up degradation, followed by an extrapolation to service conditions using Arrhenius-type laws or time-temperature superposition principles [42, 43].
While effective for simple, homogeneous materials, this "black-box" approach suffers from severe limitations when applied to modern complex systems:

- *Mechanism Shift:* It assumes that the degradation mechanism remains invariant across different temperatures, which is often incorrect for complex oxidative pathways.
- *Geometry and Scale Effects:* Empirical curves cannot account for physical phenomena that depend on the component size, such as the *Diffusion-Limited Oxidation (DLO)* profiles observed in thick cables or the thin-film anomalies discussed in *Part I*.
- *Synergistic Environments:* In scenarios like the space environment (*Part II*), where erosion and chemical attack occur simultaneously, simple correlations fail to capture the interplay between surface recession and the concurrent chemical evolution of the exposed interface.

1.4.2 The Physics-Based Approach

To overcome these limitations, this thesis advocates for a shift from empirical curve-fitting to *physics-based modeling*. The central philosophy of this work is that accurate prediction requires the explicit mathematical description of the underlying physical and chemical processes.

Instead of treating the material as a passive solid, the models developed herein treat degradation as a *multi-physics problem* governed by coupled differential equations:

1. *Chemical Kinetics:* Describing the rate of bond breaking and radical formation.

2. *Transport Phenomena:* Modeling the diffusion of oxygen or volatile byproducts within the matrix.

3. *Constitutive Mechanics:* Linking the chemical damage (molecular weight loss) to the macroscopic decay in stiffness, strength, and fracture toughness.

By solving these coupled equations, it becomes possible to predict the material state at any point in time and space, capturing phenomena, such as the formation of embrittled surface layers or protective silica shields, that empirical models overlook. This approach provides a number for the "time to failure" and a deep understanding of *why* and *how* the material fails, thereby transforming lifetime prediction from an empirical extrapolation into a rigorous computational science.

1.5 Research Objectives

The primary motivation of this research arises from the challenge of analyzing, elucidating, and modeling the complex degradation phenomena affecting the high-performance polymeric materials discussed in the previous section. Starting from the premise that environmental durability is the limiting factor for critical applications, this work aims to bridge the gap between experimental observation and predictive modeling. Specifically, the thesis is articulated around three distinct but interconnected case studies, describing three specific modeling challenges, each addressing a specific degradation mechanism or behavioral response:

- *Photo-oxidation of Low Density Polyethylene (LDPE) Films:* The first phase investigates the degradation of LDPE under UV radiation. A physical model is proposed to overcome the limitations of classical kinetic theories, addressing the failure of both the *homogeneous oxidation* assumption, which incorrectly predicts a mass loss ratio independent of sample thickness, and standard *DLO* models, which are often inapplicable in the nanometric regime, offering a more accurate explanation of the oxidative profiles and embrittlement mechanisms observed in semi-crystalline polymers. The objective is to propose a novel physical model based on the "Volatile Trapping" hypothesis, offering a rigorous explanation for the anomalous oxidative profiles observed in semi-crystalline LDPE.

- *Thermodynamic-Based Constitutive Modeling of Aging and Fracture:* The following phase establishes a *thermodynamically consistent numerical framework* designed to move beyond standard empirical failure criteria. The primary goal is to couple the photo-oxidative aging model with a viscoelastic constitutive law and a *phase-field* damage criterion, enabling the prediction of chemo-mechanical embrittlement and fracture initiation.
- *Erosion Kinetics of POSS-based Nanocomposites:* The final investigation defines a physico-chemical model for hybrid nanocomposites, specifically focusing on *POSS-reinforced polyimides* exposed to the LEO environment. The goal is to isolate the damage contribution of AO and define a physico-chemical model capable of predicting the material's lifetime. Crucially, this model quantifies the chemical reaction rates governing the characteristic formation of a silica passivation shield, linking the microscopic erosion to macroscopic mass loss.

1.6 Thesis Outline

To address the research objectives outlined above, this thesis is organized into two distinct parts, followed by a general conclusion.

Part I: Chemo-Mechanical Modeling of Bulk Degradation in Low-Density Polyethylene

The first part focuses on the degradation of semi-crystalline polymers in terrestrial environments, treating oxidation as a bulk diffusion-reaction problem coupled with mechanical embrittlement.

- *Chapter 2: Theoretical Background.* This chapter establishes the fundamental physical principles supporting the model. It provides a detailed overview of the Bolland-Gee photo-oxidation mechanism and introduces the continuum mechanics framework necessary to describe large-deformation viscoelasticity and phase-field approach to fracture. Specifically, it examines various viscoelastic constitutive models from both a theoretical and a computational modeling perspective, highlighting why classical linear elasticity is insufficient for these materials.
- *Chapter 3: Constitutive Modeling of Photo-Oxidative Degradation in LDPE Nanometric Films.* Here, the chemical kinetics of LDPE are analyzed starting from a reference experimental framework. The chapter introduces the novel *Volatile Trapping Hypothesis* to resolve the diffusion anomalies observed in nanometric films, providing a corrected prediction of mass loss compared to classical theories.

- *Chapter 4: Numerical Modeling of Viscoelastic Behavior and Fracture.* In this chapter a thermodynamically consistent viscoelastic model is implemented and augmented with a phase-field damage criterion to simulate the transition from ductile behavior to brittle fracture induced by photo-oxidative aging.

Part II: The Atomic Oxygen Challenge: Degradation Kinetics in Space Environment

The second part shifts the focus to the extreme conditions of LEO, treating degradation as a surface erosion phenomenon dictated by atomic interactions.

- *Chapter 5: Theoretical Background on Space Environment.* This chapter establishes the physical framework for Part II. It characterizes the LEO environment, identifying Atomic Oxygen as the dominant stressor for polymeric materials. The discussion details the phenomenology of erosion (linear mass loss, surface morphology) and introduces the physical principles of "self-passivation" in hybrid nanocomposites, setting the stage for the modeling phase.
- *Chapter 6: A Computational Percolation Framework for Atomic Oxygen Erosion in POSS-Nanocomposites.* Addressing the specific case of POSS-Polyimide nanocomposites, this chapter develops a novel semi-analytical framework. Starting from the analysis of reference experimental data, a *geometric percolation model* is proposed. This model mathematically describes the kinetics of the protective silica shield formation, quantifying the critical transition from an active erosion regime to a stable, passivated state.

Conclusions

- *Chapter 7: General Conclusions.* The final chapter summarizes the key findings from both parts, offering a comparative analysis of bulk vs surface degradation strategies and outlining future research directions for the "Materials-by-Design" approach.

Part I

Chemo-Mechanical Modeling of Bulk Degradation in Low-Density Polyethylene

Chapter 2

Theoretical Background

This chapter establishes the theoretical framework necessary to accurately describe the mechanical and chemical foundations underpinning this research. The discussion begins with an overview of continuum mechanics, providing the essential context for the material. Subsequently, the focus shifts to the physical and mechanical characterization of the polymer through the principles of viscoelasticity. Finally, the chapter concludes with an in-depth examination of photo-oxidation: this degradation process is analyzed not merely as a chemical reaction, but as the governing physical mechanism driving the LDPE degradation model proposed later in this study.

2.1 Continuum Mechanics and Phase-Field Fundamentals

In this section, we establish the notation, the fundamental kinematic relations and the conservation laws necessary to describe the large deformations typical of polymeric materials. To accurately describe the mechanical response of the polymer, a finite strain continuum mechanics formulation is adopted. The framework adopted follows the standard continuum mechanics theory [44, 45]. Furthermore, the theoretical basis of the phase-field formulation adopted for fracture modeling [46–48] is introduced, treating cracks not as geometric discontinuities but as a diffusive damage field. Before proceeding with the mathematical formulation, it is convenient to establish the notation employed throughout this manuscript. Standard tensor notation is adopted: scalars are denoted by lightface italic letters (e.g., J, ρ), vectors by bold lowercase letters (e.g., $\mathbf{u}$, $\mathbf{x}$), and second-order tensors by bold uppercase letters (e.g., $\mathbf{F}$, $\mathbf{P}$). When necessary, fourth-order tensors are identified by blackboard bold or calligraphic letters (e.g., $\mathbb{C}$). Throughout the chapters, the superimposed dot will indicate the material time derivative (or Lagrangian time derivative) with respect to the reference configuration. The standard tensor

operations, such as the dot product $(\cdot)$ and the double contraction $(:)$, follow standard continuum mechanics conventions.

2.1.1 Kinematics of Finite Deformations

Let $\Omega_0 \subset \mathbb{R}^3$ be a continuous body, identified with the portion of space it occupies in a fixed reference configuration at time $t = 0$, and let $\Omega_t \subset \mathbb{R}^3$ be the current configuration at time t. To establish the mathematical representation of the body, we first define $\mathbf{X}$ as the vector identifying the location of an arbitrary material point in the initial configuration Ω_0. The boundary of the reference domain Ω_0 is denoted by Γ_0, characterized at any point by the outward unit normal vector $\mathbf{m}$. Analogously, in the current configuration Ω_t, the domain is bounded by the surface Γ_t, whose orientation is defined by the outward unit normal vector $\mathbf{n}$. The motion is described by a smooth vector-valued function χ, that maps points from the reference to the current configuration over the time interval of interest:

$$\chi : \Omega_0 \times [0, T] \to \mathbb{R}^3 \tag{2.1}$$

In this setup, as illustrated in Figure 2.1 we can define a one-to-one motion mapping, defining the response of the body to externally applied mechanical stimuli, as:

$$\mathbf{x} = \chi(\mathbf{X}, t) \tag{2.2}$$

which provides the exact spatial position $\mathbf{x}$ in the current configuration Ω_t for a given particle $\mathbf{X}$ for a given time $t \in \mathbb{R}$.

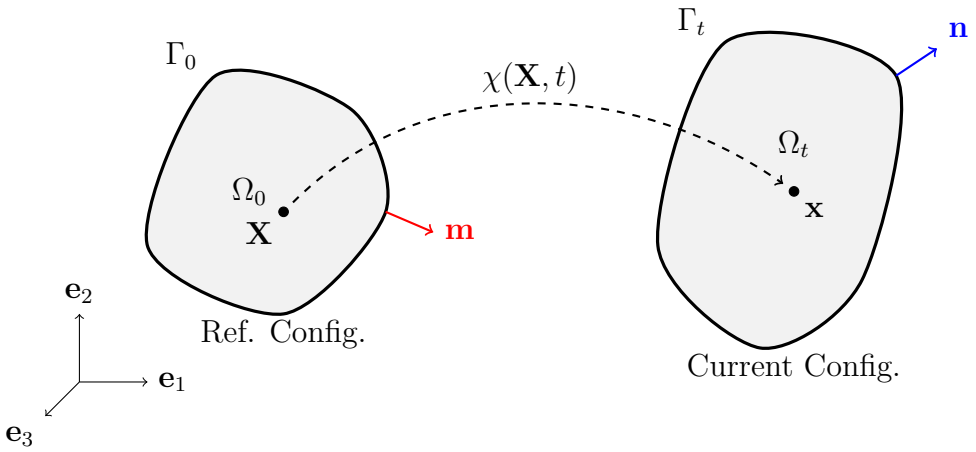

Figure 2.1: Kinematics of finite deformation. The non-linear map χ transforms the material point $\mathbf{X}$ in the reference configuration Ω_0 to the spatial position $\mathbf{x}$ in the current configuration Ω_t.

Consequently, the displacement field $\mathbf{u}(\mathbf{X}, t)$, representing the vector connecting the reference and current positions, is defined as:

$$\mathbf{u}(\mathbf{X}, t) = \mathbf{x} - \mathbf{X} \tag{2.3}$$

To define the boundary value problem, the solid body is assumed to be under the influence of a distributed body force field $\mathbf{b}$, defined per unit mass. The total surface Γ_0 is partitioned into two distinct subsets: the Dirichlet boundary Γ_{0u}, where the displacement field $\bar{\mathbf{u}}$ is enforced, and the Neumann boundary Γ_{0t}, subject to natural boundary conditions. These regions are mutually exclusive and collectively exhaustive, satisfying the topological conditions $\Gamma_{0u} \cup \Gamma_{0t} = \Gamma_0$ and $\Gamma_{0u} \cap \Gamma_{0t} = \emptyset$.

Given these formal notations, to build the basis for the governing equations used, we introduce the fundamental measure of local deformation, the deformation gradient tensor $\mathbf{F}$, which maps infinitesimal material line elements $d\mathbf{X}$ from Ω_0 to spatial line elements $d\mathbf{x}$ in Ω_t. It is obtained as the gradient of the motion with respect to the reference coordinates:

$$\mathbf{F} = \nabla_{\mathbf{X}} \chi(\mathbf{X}, t) = \frac{\partial \mathbf{x}}{\partial \mathbf{X}} = \mathbf{I} + \nabla_{\mathbf{X}} \mathbf{u} \tag{2.4}$$

where $\mathbf{I}$ denotes the second-order identity tensor. To ensure the physical admissibility of the motion (i.e., preventing the material from penetrating itself), the Jacobian determinant $J = \det(\mathbf{F})$, representing the local volume ratio between the current and reference configurations, must be strictly positive:

$$J = \det \mathbf{F} > 0$$

For constitutive modeling in the Lagrangian framework, it is necessary to define strain measures that are independent of rigid body rotations. To this end, the right Cauchy-Green deformation tensor $\mathbf{C}$ is introduced:

$$\mathbf{C} = \mathbf{F}^T \mathbf{F} \tag{2.5}$$

which is symmetric and positive definite.

2.1.2 Geometric Representation of Phase-Field Fracture

In addition to the deformation of the bulk material, the kinematic description must explicitly account for the presence of discontinuities. Specifically, the externally applied mechanical stimuli mentioned before, may result in the nucleation and subsequent propagation of cracks within the polymer matrix, locally violating the continuity of the medium. As shown in Figure 2.2, in the phase-field approach the body Ω_0 contains a sharp crack δ_0, which is approximated by a smeared localization

band $\mathcal{B} \subseteq \Omega_0$. Within this band, a scalar phase-field variable (or damage field) $d(\mathbf{X}, t)$ is defined.

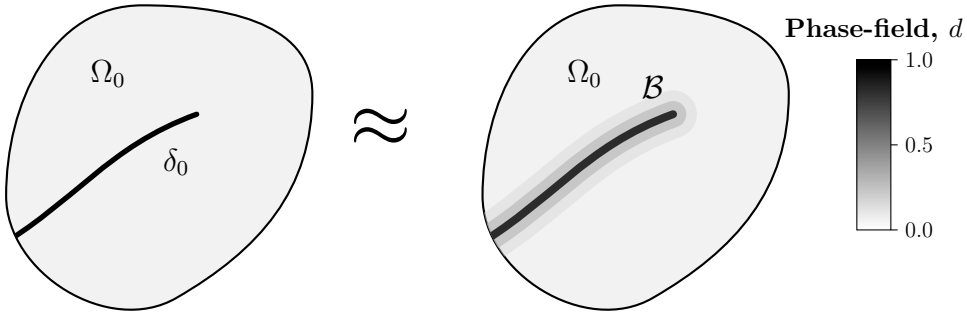

(a) Initial configuration with a sharp crack **(b)** Initial configuration with a crack band representation

Figure 2.2: Phase-field approximation of fracture. (a) A sharp crack surface δ_0 is a geometric discontinuity in the body Ω_0. (b) The phase-field approach regularizes the crack into a diffusive crack band $\mathcal{B}$, where the damage level is described by the continuous scalar field $d \in [0, 1]$. Adapted from [46, 49].

The localization band is delimited by the external boundary $\partial\mathcal{B}$, characterized by the outward unit normal vector $\mathbf{m}_{\mathcal{B}}$. Phase-field constraints are enforced on two distinct subsets: essential (Dirichlet) boundary conditions are applied on $\partial\mathcal{B}_d$, while natural (Neumann) boundary conditions are imposed on the complementary portion $\partial\mathcal{B}_p$. Following standard continuum damage mechanics principles, the damage fields assume values of $d(\mathbf{X}, t) = 0$, accounting for an intact, ideal material without damage, and $d(\mathbf{X}, t) = 1$, representing the completely fractured state, and therefore, the damage field can assume just real values in the range $d \in [0,1]$.

Having established the kinematic measures required to describe both bulk deformation and fracture, we now proceed to formulate the fundamental balance laws. The mechanical response of the continuum is governed by the conservation of linear momentum coupled with the evolution of the damage field, as detailed in the following section.

2.1.3 Balance Laws and Governing Equations

The mechanical response of the continuum is governed by a coupled system of partial differential equations (PDEs) representing the balance of linear momentum and the evolution of the damage field.

Mechanical Equilibrium and Stress Measures

Neglecting inertial effects (quasi-static assumption), the equilibrium equation in the reference configuration (for the constitutive modeling of solids, it is often convenient to work in the reference configuration) is given by:

$$\mathrm{Div}(\mathbf{P}) + \bar{\mathbf{b}} = \mathbf{0} \quad \text{in } \Omega_0 \tag{2.6}$$

where $\bar{\mathbf{b}}$ represents the body force vector per unit volume. The tensor $\mathbf{P}$ denotes the First Piola-Kirchhoff stress, which relates forces in the current configuration to the reference area. The adoption of $\mathbf{P}$, rather than the Cauchy stress $\boldsymbol{\sigma}$, is necessitated by the *finite strain* nature of the problem characterizing soft polymers like LDPE. In this regime, the geometric distinction between the reference and current configurations is non-negligible, making the Lagrangian formulation essential for consistent numerical time-integration. The relation between the two stress measures is given by the push-forward operation:

$$\boldsymbol{\sigma} = J^{-1}\mathbf{P}\mathbf{F}^T \tag{2.7}$$

This equilibrium equation is complemented by the boundary conditions acting on the previously defined surfaces. Specifically, on the Neumann boundary Γ_{0t}, the stress projection must balance the prescribed traction vector $\bar{\mathbf{t}}$:

$$\mathbf{P}\mathbf{m} = \bar{\mathbf{t}} \quad \text{on } \Gamma_{0t} \tag{2.8}$$

Phase-Field Evolution Equation

Coupled to the mechanical equilibrium, the degradation of the material is described by the evolution of the scalar phase-field variable d. The governing equation for the damage field is derived from the minimization of the total potential energy functional. By defining $\alpha(d)$ as the geometric crack function and $\omega(d)$ as the degradation function, the resulting Euler-Lagrange equation describing the diffusive crack topology is given by the following formulation [50]:

$$\frac{G_c}{c_\alpha}\left(\frac{\alpha'(d)}{l_c} - 2l_c\Delta_{\mathbf{X}}d\right) + \omega'_{(d)}\psi_{0(\mathbf{C})} = 0 \quad \text{, in } \mathcal{B} \subseteq \Omega_0 \tag{2.9}$$

In this expression, $\psi_{0(\mathbf{C})}$ represents the strain energy density of the undamaged viscoelastic material, acting as the driving force for the damage evolution. The parameter G_c denotes the critical energy release rate, while l_c is the length scale parameter that regularizes the width of the damage band. The constant c_α is a normalization factor defined by the integral of the geometric function. To complete the boundary value problem for the damage field, a natural boundary condition is enforced on the crack surface boundary $\partial\mathcal{B}_p$, ensuring no flux of damage across the boundary:

$$\frac{2l_c G_c}{c_\alpha}\nabla_{\mathbf{X}} d \cdot \mathbf{m} = 0 \quad \text{on } \partial\mathcal{B}_p \tag{2.10}$$

2.1.4 Thermodynamic Principles and Constitutive Requirements

To close the system of equations, constitutive relations linking the stress $\mathbf{P}$ to the kinematic variables are required. However, these relations cannot be chosen arbitrarily; they must be strictly compatible with the fundamental principles of thermodynamics. Specifically, the model must satisfy the Second Law, expressed locally by the Clausius-Duhem inequality:

$$\mathcal{D}_{int} = \mathbf{P} : \dot{\mathbf{F}} - \dot{\Psi} \geq 0 \tag{2.11}$$

where $\Psi(\mathbf{C}, d)$ is the Helmholtz free energy density describing the material state. Physically, this inequality enforces the condition of *thermodynamic admissibility*: it ensures that the internal dissipation ($\mathcal{D}_{int}$) remains non-negative for any evolution of the system. A violation of this condition ($\mathcal{D}_{int} < 0$) would imply a spontaneous decrease in entropy (or creation of energy), which is physically impossible. To guarantee that this constraint is satisfied for *any* arbitrary admissible process (i.e., for any rate of deformation $\dot{\mathbf{F}}$), we apply the standard Coleman-Noll procedure [51, 52]. Since the inequality must hold regardless of the kinematic path, the coefficient of the deformation rate term must vanish, identifying the stress tensor as the variable energetically conjugate to the deformation. Thus, the general constitutive relation is defined as:

$$\mathbf{P} = \frac{\partial \Psi}{\partial \mathbf{F}} \tag{2.12}$$

This relation establishes the thermodynamic basis for the model. The specific form of the free energy potential Ψ, capturing the viscoelastic behavior and the degradation of the LDPE, will be explicitly derived in Chapter 4. The discussion now moves to the crucial concept of viscoelasticity; understanding these mechanics is a prerequisite for interpreting the full potential of the constitutive model utilized in this research.

2.2 Fundamentals of Viscoelasticity

The formalization and extensive application of linear and non-linear viscoelastic concepts have become imperative in recent decades, driven by the ubiquitous adoption of polymeric materials in engineering. Unlike idealized continuum media, polymeric materials exhibit a complex constitutive response that cannot be adequately captured by the classical theories of pure elasticity or viscosity. The following theoretical framework and the distinction between elastic, viscous, and viscoelastic responses are primarily based on the classical treatment by Christensen [53]. To clarify this distinction, it is useful to refer to the thermodynamic principles governing the two classical limit theories:

- *Theory of Elasticity:* Describes materials possessing the capacity to store mechanical energy (potential energy) with no dissipation. Upon unloading, the deformation work is fully recovered. The response to an applied load is instantaneous and fully reversible. The stress σ is directly proportional to the strain ε ($\sigma = E\varepsilon$). A mechanical spring is the standard analog.

- *Theory of Viscosity:* Describes Newtonian fluids which, particularly in a non-hydrostatic stress state, possess the capacity to dissipate energy through internal friction but lack the ability to store it. The response is time-dependent and irreversible. The stress is proportional to the *rate* of strain $\dot{\varepsilon}$ ($\sigma = \eta\dot{\varepsilon}$). A hydraulic dashpot is the standard analog.

Consequently, a more comprehensive framework is required for polymers, as they represent a class of materials where only a fraction of the work done during deformation is recoverable. They possess a fundamental *dual nature*, exhibiting a hysteretic response with the simultaneous capacity to store and dissipate mechanical energy. This hybrid thermodynamic character translates directly into a distinct kinematic response, which becomes evident when considering a specific loading history: a suddenly applied stress state maintained constant thereafter. In this scenario, a purely elastic material would respond instantaneously with a fixed deformation that remains constant over time. Conversely, a Newtonian fluid would respond to a uniform shear stress with a steady flow process. Polymeric materials, however, combine features of both theories: upon loading, they exhibit an instantaneous elastic effect (immediate deformation) followed by a time-dependent flow process. This delayed response, known as *creep*, implies that the deformation continues to evolve over time. The terminal behavior depends intrinsically on the molecular structure: cross-linked networks restrict macroscopic chain slippage, leading to an asymptotic equilibrium limit, whereas linear chains can continuously disentangle, resulting in an indefinite viscous flow. It is instructive to generalize this observation by considering a sequence of loading events, representing a superimposition of surface tractions.

Suppose a material exhibiting the aforementioned instantaneous elasticity and creep characteristics is subjected to two *non-simultaneously applied* sudden changes in uniform stress. After the first application, but prior to the second, the material responds in a time-dependent manner governed by the magnitude of the first stress state. Crucially, if we consider the situation at an arbitrary time interval after the sudden application of the *second* stress state, the response reveals the unique nature of viscoelasticity. The material not only experiences the instantaneous response to the second load increment, but it also exhibits a *continuing time-dependent response* due to the first applied level of stress. This linear additivity of responses physically underpins the well-known *Boltzmann Superposition Principle*. This behavior stands in stark contrast to an ideal elastic material, which would respond solely to the *total* stress level at that specific instant, independent of loading sequence.

Thus, this class of materials possesses a characteristic descriptively referred to as a *memory effect*. The material response is not merely determined by the current state of stress (as in elasticity) or the current rate of strain (as in viscosity), but is functionally dependent on the *entire history* of past stress states. By duality, a similar situation exists if the deformation history is specified: the current stress depends upon the entire past history of deformation.
This behavior is termed *viscoelasticity*. Viscoelastic polymers lie between these two limits. Physically, this is rooted in their macromolecular structure: the "elastic" component arises from the reversible stretching of bond angles and lengths, while the "viscous" component results from the irreversible slippage and disentanglement of polymer chains (e.g., reptation mechanisms) and the time-dependent rearrangement of molecular conformations [54]. Consequently, a viscoelastic material possesses a "fading memory" of its deformation history.

2.2.1 Phenomenology: Creep and Stress Relaxation

The macroscopic manifestation of the time-dependent behavior described above is traditionally characterized through two fundamental experimental protocols: *creep* and *stress relaxation*. These tests isolate the response of the material to a step input in stress or strain, respectively, providing the "fingerprint" of its viscoelastic properties.

Creep (Time-Dependent Deformation)

Creep is the slow, progressive deformation of a material under constant stress. It occurs when a material is subjected to a persistent force over an extended period, resulting in a time-evolving strain even if the load remains unchanged. In a creep test, a constant stress σ_0 is instantaneously applied to the specimen at time $t = 0$ and maintained constant thereafter ($\sigma(t) = \sigma_0 \cdot \mathcal{H}(t)$, where $\mathcal{H}(t)$ is the Heaviside

step function, defined as zero for t less than zero, one for t greater than zero, and 1/2 for t = 0.). The material responds with an initial, instantaneous elastic deformation ε_0, followed by a time-dependent increase in strain known as *creep strain*. This evolution reflects the slow reorientation, disentanglement, and slippage of polymer chains towards a new equilibrium configuration.

The input (Stress) and output (Strain) of this test are visually summarized below:

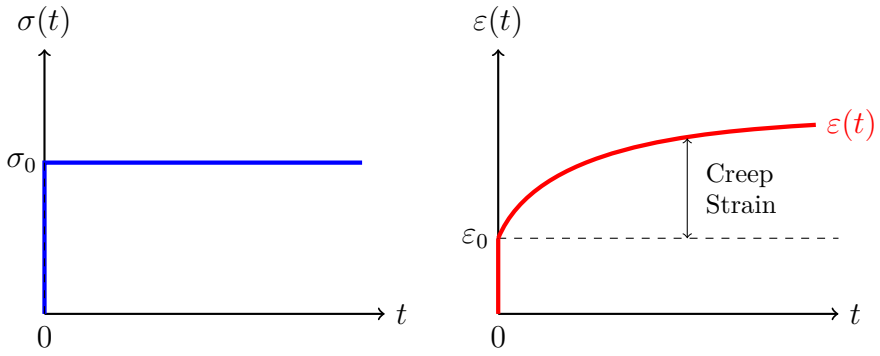

(a) Input: Constant Stress **(b) Output:** Time-Dependent Strain

Figure 2.3: Schematic representation of a creep test. (a) The applied stress history (Heaviside step at $t = 0$). (b) The resulting strain response, showing the instantaneous elastic part (ε_0) and the delayed viscoelastic component.

To generalize this behavior beyond the specific stress level applied in the test, we must introduce a material property that is independent of the load magnitude. Assuming the material operates within the range of *linear viscoelasticity* (where doubling the stress simply results in doubling the strain), we can normalize the response. We define the *creep compliance* $J(t)$, which physically represents the "softness" or "flexibility" of the material over time (the inverse of stiffness):

$$J(t) = \frac{\varepsilon(t)}{\sigma_0} \tag{2.13}$$

It describes how much strain is generated per unit of applied stress as time progresses. The typical evolution of the compliance for a viscoelastic solid is depicted in Figure 2.4.

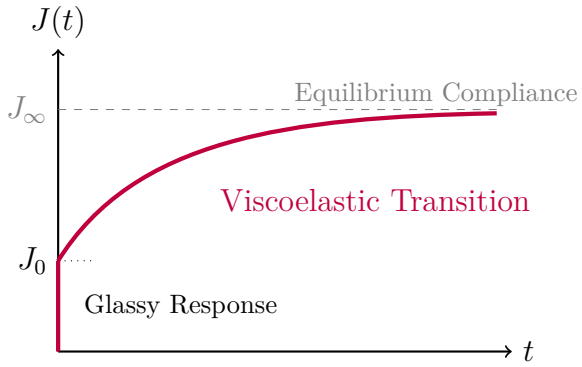

Figure 2.4: Typical creep compliance curve $J(t)$ for a viscoelastic solid. J_0 represents the instantaneous elastic compliance (known as glassy response), while J_∞ represents the long-term equilibrium compliance reached when the polymer chains have fully rearranged.

The initial response of the LDPE specimen is characterized by the instantaneous compliance J_0, representing the purely elastic (glassy) deformation. This parameter is related to the initial elastic modulus E_0 by the relation $J_0 = 1/E_0$, defining the material state before the onset of viscous dissipation. We observe that for a viscoelastic solid (e.g., cross-linked polymers), $J(t)$ increases but eventually approaches an asymptotic value (J_∞, equilibrium compliance). Conversely, for viscoelastic fluids (e.g., thermoplastics above T_g), $J(t)$ may increase indefinitely due to irreversible viscous flow.

Stress Relaxation (Time-Dependent Stress Decay)

Stress relaxation represents the dual phenomenon to creep. While creep measures the change in dimension under a fixed load, stress relaxation measures the reduction in resistance (stress) under a fixed dimension. In a stress relaxation test, a constant deformation ε_0 is instantaneously imposed on the specimen at time $t = 0$ and held fixed thereafter ($\varepsilon(t) = \varepsilon_0 \cdot \mathcal{H}(t)$). Unlike an ideal elastic solid, where the induced stress would remain constant ($\sigma = E\varepsilon_0$) indefinitely, a viscoelastic material exhibits a characteristic monotonic decay of stress over time. The input (Strain) and output (Stress) of this test are visually summarized in Figure 2.5:

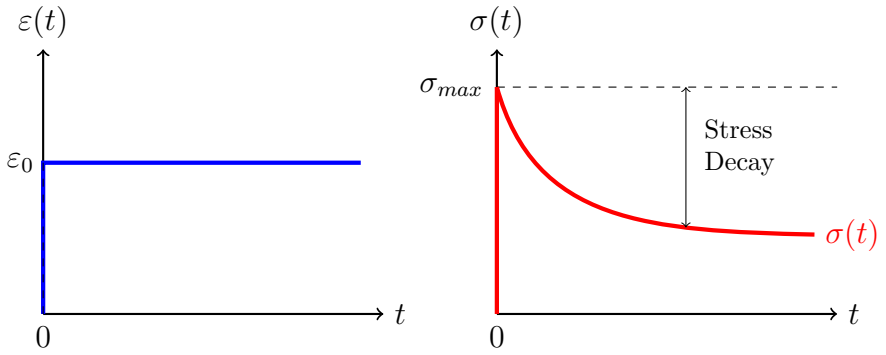

(a) Input: Constant Deformation **(b) Output:** Time-Dependent Stress

Figure 2.5: Schematic representation of a stress relaxation test. (a) The imposed strain history (Heaviside step). (b) The resulting stress response, showing the peak instantaneous resistance and the subsequent decay as the material relaxes.

Physically, this decay occurs because the polymer chains are initially stretched into a non-equilibrium conformation. At $t = 0^+$, the material reacts with its "glassy" stiffness, offering maximum resistance. As time progresses, the molecular chains gradually disentangle, slip past one another, and reorganize (via conformational changes) to relieve the internal tension, dissipating the stored elastic energy into heat. Crucially, this happens without any change in the macroscopic shape of the specimen.

Similar to the definition of compliance for creep, we introduce a material property that is independent of the magnitude of the applied strain. Assuming linear viscoelasticity, we define the *relaxation modulus* $E(t)$:

$$E(t) = \frac{\sigma(t)}{\varepsilon_0} \tag{2.14}$$

$E(t)$ represents the "stiffness history" of the material. As illustrated in Figure 2.6, it starts at a high value (E_0 or glassy modulus) and decays over time. The terminal behavior depends on the molecular architecture:

- *Viscoelastic Solids (Cross-linked):* The stress decays to a non-zero equilibrium value (σ_∞), leading to an *equilibrium modulus* E_∞. This indicates that the chemical cross-links prevent complete flow, maintaining a residual elastic network.

- *Viscoelastic Fluids (Linear chains):* The stress may relax completely to zero given sufficient time ($E(t) \to 0$), as the chains can fully disentangle and flow.

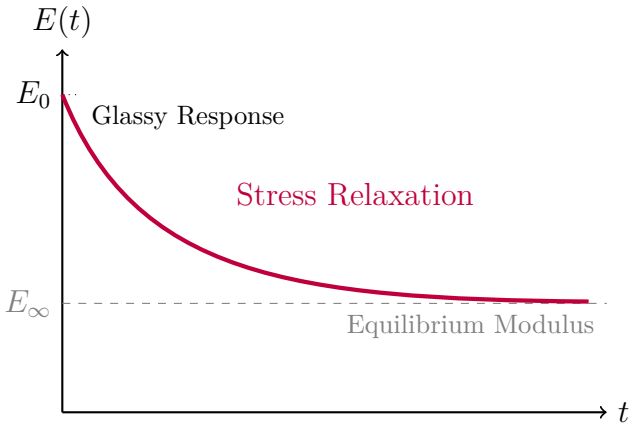

Figure 2.6: Typical relaxation modulus curve $E(t)$ for a viscoelastic solid. It is a parameter that represents the material transitions from a rigid, glassy response (E_0) to a softer, rubbery equilibrium state (E_∞).

2.2.2 Mathematical Models for Linear Viscoelastic Response

To mathematically describe the linear viscoelastic behavior, it is customary to utilize rheological models constructed from combinations of two fundamental lumped-parameter elements: *linear elastic springs* and *linear viscous dashpots*. This approach provides a convenient method for developing the ordinary differential equations that describe the characteristic time dependence of the viscoelastic response, while also facilitating the visualization of molecular motions employing "spring-dashpot" analogies. The visual representation and constitutive definitions of these fundamental elements are illustrated in Figure 2.7.

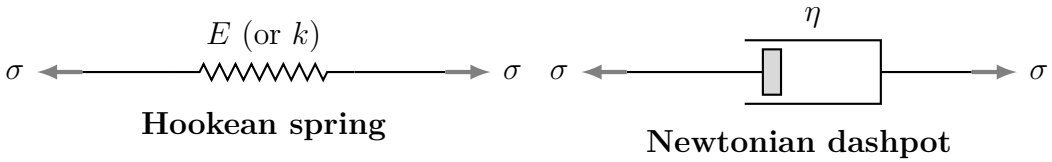

Figure 2.7: Fundamental rheological elements: the Hookean spring (left) representing elastic energy storage, and the Newtonian dashpot (right) representing viscous energy dissipation.

- The *Hookean spring* represents the elastic component (E). It obeys Hooke's law:

$$\sigma = E\varepsilon \tag{2.15}$$

where σ and ε are analogous to the spring force and displacement, respectively. The spring constant E (often denoted as k in general mechanics) has units of $\mathrm{N/m^2}$ and corresponds to the Young's modulus. Physically, the spring models the instantaneous bond deformation of the material, and its magnitude is related to the fraction of mechanical energy stored reversibly as strain energy.

- The *Newtonian dashpot* represents the viscous component (η). It obeys Newton's law of viscosity, in which the stress produces not a strain but a strain rate:

$$\sigma = \eta\dot{\varepsilon} \tag{2.16}$$

Here, the overdot denotes time differentiation (d/dt) and η is the viscosity with units of $\mathrm{Pa \cdot s}$ (equivalent to $\mathrm{N \cdot s/m^2}$). Physically, this element captures the fluid-like nature of the entropic uncoiling process and chain slippage.

In many of the relations to follow, it will be convenient to employ the ratio of viscosity to stiffness:

$$\tau = \frac{\eta}{E} \tag{2.17}$$

The unit of τ is time, and it will be seen that this ratio represents a fundamental timescale of the material, serving as a useful measure of the response speed (relaxation or retardation) of the viscoelastic system.

By arranging these elements in series or parallel, constitutive equations describing the time-dependent relationship between stress and strain can be derived.

The Maxwell Spring-Dashpot Model

The Maxwell model consists of a Hookean spring and a Newtonian dashpot connected in *series*. The spring should be visualized as representing the elastic or energetic component of the response, while the dashpot represents the conformational or entropic component. The schematic representation of this configuration is shown in Figure 2.8.

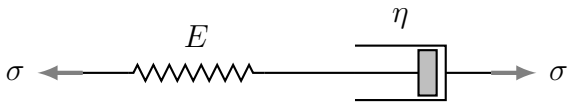

Figure 2.8: The Maxwell model: a spring and dashpot connected in series.

In this configuration, equilibrium requires that the stress on each element is the same and equal to the imposed stress:

$$\sigma = \sigma_s = \sigma_d \tag{2.18}$$

Conversely, the total strain is the sum of the individual strains in each element:

$$\varepsilon = \varepsilon_s + \varepsilon_d \tag{2.19}$$

where the subscripts s and d denote the spring and dashpot, respectively. In seeking a single constitutive equation relating the total stress to the total strain, it is convenient to differentiate the strain equation with respect to time. Recalling that for the spring $\varepsilon_s = \sigma/E$ and for the dashpot $\dot{\varepsilon}_d = \sigma/\eta$, we obtain:

$$\dot{\varepsilon} = \dot{\varepsilon}_s + \dot{\varepsilon}_d = \frac{\dot{\sigma}}{E} + \frac{\sigma}{\eta} \tag{2.20}$$

Multiplying by the stiffness E (or k) and introducing the characteristic time constant $\tau = \eta/E$:

$$E\dot{\varepsilon} = \dot{\sigma} + \frac{1}{\tau}\sigma \tag{2.21}$$

This expression represents the governing constitutive equation for a Maxwell material. Note that it contains time derivatives, implying that a simple constant of proportionality between stress and strain does not exist.

This model is particularly effective at describing *stress relaxation*. For a constant strain ε_0 applied at $t = 0$ (where $\dot{\varepsilon} = 0$ for $t > 0$), the differential equation simplifies to $\dot{\sigma} + \sigma/\tau = 0$, whose solution yields an exponential decay of stress:

$$\sigma(t) = \sigma_0 e^{-t/\tau} \tag{2.22}$$

Here, τ is the *Relaxation Time*, the critical parameter mentioned before, defining the timescale of the material's memory. However, the Maxwell model possesses a major limitation: under constant stress (creep), the term σ/η leads to a constant strain rate, predicting a linear unbounded deformation ($\varepsilon(t) \propto t$). Since it flows indefinitely like a liquid, it is often referred to as a *viscoelastic fluid*.

The Kelvin-Voigt Model

The Kelvin-Voigt model consists of a Hookean spring and a Newtonian dashpot connected in *parallel*. In this arrangement, the physical constraint is purely kinematic: the two elements are forced to deform together. The schematic representation is illustrated in Figure 2.9.

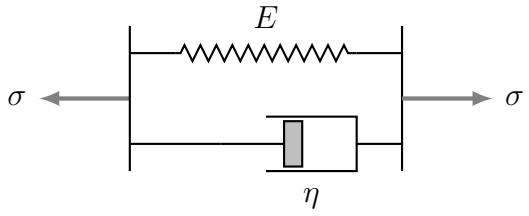

Figure 2.9: The Kelvin-Voigt model: a spring and dashpot connected in parallel, enforcing equal strain on both elements.

Due to the parallel connection, the strain in each element is identical and equal to the total strain of the system:

$$\varepsilon = \varepsilon_s = \varepsilon_d \tag{2.23}$$

Conversely, the total stress is supported by both components, meaning the total stress is the sum of the stresses in the spring and the dashpot:

$$\sigma = \sigma_s + \sigma_d \tag{2.24}$$

Substituting the constitutive laws for each element ($\sigma_s = E\varepsilon$ and $\sigma_d = \eta\dot{\varepsilon}$), we arrive at the governing differential equation:

$$\sigma = E\varepsilon + \eta\dot{\varepsilon} \tag{2.25}$$

Dividing by E and utilizing the time constant $\tau = \eta/E$:

$$\frac{\sigma}{E} = \varepsilon + \tau\dot{\varepsilon} \tag{2.26}$$

This model successfully captures the phenomenon of *creep*. If a constant stress σ_0 is applied at $t = 0$, the solution to the differential equation is:

$$\varepsilon(t) = \frac{\sigma_0}{E}\left(1 - e^{-t/\tau}\right) \tag{2.27}$$

Here, the strain does not occur instantaneously but grows asymptotically towards the elastic limit σ_0/E. The parameter τ in this context is called the *Retardation Time*, as it describes the delay in the elastic response. However, the Kelvin-Voigt model possesses significant limitations. First, it is incapable of describing *Stress Relaxation*: physically, the rigid parallel connection prevents the spring from relaxing if the total strain is held constant; mathematically, an instantaneous step strain would require an infinite strain rate, implying a theoretical infinite stress in the dashpot singularity. Second, the model fails to capture the *instantaneous elastic deformation* upon loading, as the viscous element retards any immediate movement. Finally, since it predicts strictly solid-like behavior with full strain recovery (no permanent set) upon unloading, it is distinctively referred to as a *viscoelastic solid*, making it unsuitable for describing flow in uncrosslinked polymers.

The Standard Linear Solid (SLS)

Since neither the Maxwell nor the Kelvin-Voigt models can simultaneously predict both creep and relaxation accurately for real polymers, a three-element model known as the *Standard Linear Solid (SLS) (or Zener model)* is employed. Constructed by placing a spring in parallel with a Maxwell arm (or, alternatively, a spring in series with a Kelvin-Voigt unit), it provides the simplest realistic representation of a polymer. Physically, this architecture acknowledges that conformational changes are eventually limited by the network of entanglements or permanent junction points, requiring a more elaborate spring-dashpot arrangement than simple binary models. The "Maxwell form" of the SLS is illustrated in Figure 2.10.

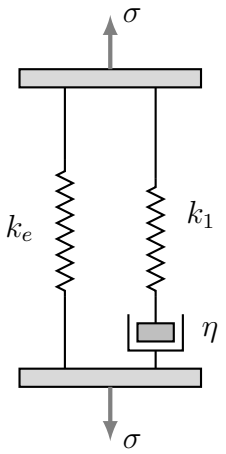

Figure 2.10: The Standard Linear Solid (SLS) in its Maxwell form. The isolated spring k_e provides the long-term equilibrium stiffness.

In this configuration, the parallel spring is denoted by stiffness k_e. It is termed the *equilibrium stiffness* because it provides the "rubbery" restoring force that remains after the stresses in the Maxwell arm have fully relaxed. Mechanically, the Maxwell arm and the parallel spring k_e experience the same strain (ε), and the total stress σ is the sum of the stresses in each arm:

$$\sigma = \sigma_e + \sigma_m \tag{2.28}$$

Solving for σ_m in the time domain is often cumbersome due to the coupling of stress and its time derivative. To overcome this, the *Laplace transformation* is frequently employed, reducing linear differential equations to algebraic ones. Denoting the transformed functions with an overline and explicitly indicating their dependence on the Laplace variable s (e.g., $\mathcal{L}\{\dot{\varepsilon}(t)\} = s\bar{\varepsilon}(s)$), the constitutive law for the Maxwell

arm becomes:

$$\bar{\sigma}_m(s) = \frac{k_1 s}{s + \frac{1}{\tau}} \bar{\varepsilon}(s) \tag{2.29}$$

where $\tau = \eta/k_1$ is the relaxation time of the arm. Adding the contribution of the equilibrium spring ($\bar{\sigma}_e(s) = k_e \bar{\varepsilon}(s)$), the total stress in the Laplace domain is:

$$\bar{\sigma}(s) = \left(k_e + \frac{k_1 s}{s + \frac{1}{\tau}} \right) \bar{\varepsilon}(s) \tag{2.30}$$

This result allows defining the *associated viscoelastic constitutive equation*, reminiscent of Hooke's law ($\bar{\sigma}(s) = \bar{E}(s)\bar{\varepsilon}(s)$), where the complex modulus $\bar{E}(s)$ is defined as:

$$\bar{E}(s) = \frac{k_e(s + 1/\tau) + k_1 s}{s + 1/\tau} \tag{2.31}$$

This complex modulus effectively captures the "dual nature" of polymers without the need to revert to a cumbersome time-domain differential equation. Physically, the model exhibits instantaneous elasticity upon loading (governed by the unrelaxed modulus $k_e + k_1$), delayed elasticity (primary creep), and stress relaxation, eventually settling to a non-zero equilibrium modulus determined strictly by k_e.

Owing to this capacity to decouple the equilibrium elastic response from the transient dissipative decay, this specific rheological architecture is adopted as the physical baseline for the advanced damage-coupled thermodynamic framework developed in Chapter 4.

The Generalized Maxwell Model (Wiechert Model)

While the SLS introduces the concept of a relaxation time, a real polymer rarely relaxes with a single characteristic time constant. Physically, this deviation arises because the macromolecular structure is complex: molecular segments of varying lengths and degrees of entanglement contribute differently to the relaxation process, with shorter, mobile segments relaxing much faster than longer, entangled chains. Consequently, a discrete distribution of relaxation times is observed, producing a relaxation process spread over a much wider logarithmic time scale than can be accurately modeled by a single τ.

To rigorously capture this broad relaxation spectrum, the *Wiechert Model* (also known as the Generalized Maxwell Model) is employed. As illustrated in Figure 2.11, this model generalizes the SLS by placing an arbitrary number (N) of Maxwell elements in parallel with the equilibrium spring k_e.

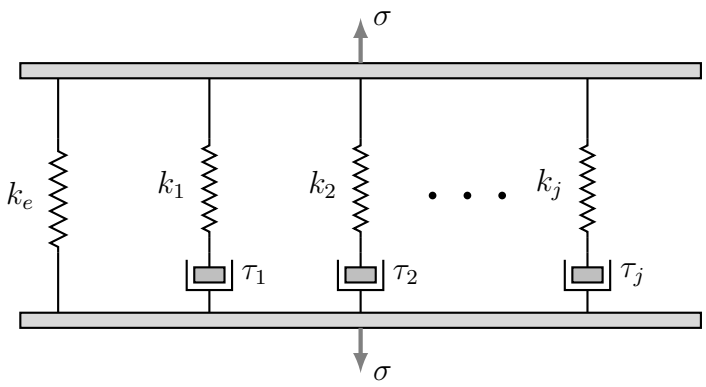

Figure 2.11: The Wiechert model (generalized Maxwell model), composed of an equilibrium spring k_e and N Maxwell elements in parallel to approximate the distribution of relaxation times.

Mechanically, the total stress σ transmitted by the model is the sum of the stress in the isolated equilibrium spring (k_e) and the stresses in each of the N Maxwell spring-dashpot arms (σ_j). Extending Equation (2.29) to the j-th element, the transformed stress in a single Maxwell arm is given by:

$$\bar{\sigma}_j(s) = \frac{k_j s}{s + \frac{1}{\tau_j}} \bar{\varepsilon}(s) \tag{2.32}$$

Consequently, the constitutive equation for the entire array in the Laplace domain is obtained by summation:

$$\bar{\sigma}(s) = \bar{\sigma}_e(s) + \sum_{j=1}^{N} \bar{\sigma}_j(s) = \left(k_e + \sum_{j=1}^{N} \frac{k_j s}{s + \frac{1}{\tau_j}} \right) \bar{\varepsilon}(s) \tag{2.33}$$

The quantity in the parentheses represents the *viscoelastic modulus operator* $\bar{E}(s)$ extended to the Wiechert model. In the time domain, this corresponds to expressing the relaxation modulus $E(t)$ as a *Prony series*, which is the standard format used in Finite Element Analysis (FEA) software to define viscoelastic material properties:

$$E(t) = E_e + \sum_{j=1}^{N} E_j e^{-t/\tau_j} \tag{2.34}$$

where E_e (corresponding to the equilibrium spring k_e) is the long-term equilibrium modulus, and the pairs (E_j, τ_j), corresponding to the stiffness and relaxation time of each Maxwell arm, define the discrete relaxation spectrum.

While the concept of viscoelasticity defines the material's mechanical response under stress, this behavior is not static but evolves due to environmental exposure. To account for this, the final section examines photo-oxidation: the fundamental chemical mechanism responsible for altering the polymer's structure and, consequently, its mechanical integrity.

2.3 Physico-Chemical Background: Photo-Oxidation of LDPE

The physical rationale underpinning the Volatile Trapping Model requires a detailed examination of the macromolecular processes driving PE photo-oxidation. From a theoretical standpoint, an ideal PE chain consists exclusively of saturated $-CH_2-$ bonds, which are transparent to ultraviolet radiation (wavelength of $\lambda > 290$ nm) and therefore inherently stable. However, commercial-grade LDPE inevitably contains manufacturing imperfections, such as hydroperoxides, carbonyl groups, and traces of metallic catalysts, along with structural unsaturations like C=C double bonds. As established by Bolland et al. [55, 56], these olefinic sites are critical as they promote the generation of hydroperoxides. These irregularities function as extrinsic chromophores, sensitizing the material to light absorption [57, 58].

Consequently, when exposed to UV radiation in an aerobic environment, these reactive sites trigger an auto-oxidative radical chain reaction. It is crucial to note that this degradation mechanism is spatially selective: it occurs predominantly within the oxygen-permeable amorphous regions of the semi-crystalline matrix, while the dense crystalline lamellae act as diffusion barriers and remain initially unaffected by the oxidative attack [59].

2.3.1 The Oxidative Cycle and Autocatalysis

The kinetic evolution of LDPE degradation follows the well-established auto-oxidation mechanism originally proposed by Bolland and Gee [55, 56]. While initially derived for olefinic rubbers, this closed-loop radical scheme constitutes the universal paradigm for polyolefin degradation and comprises three fundamental phases:

- *Initiation:* As previously discussed, the pristine polyethylene backbone is photo-stable. Photo-initiation relies entirely on manufacturing defects, specifically hydroperoxides ($POOH$) and carbonyl groups ($C=O$), acting as extrinsic chromophores. Consequently, the formation of primary macroradicals ($P^{\bullet}$) occurs via specific photochemical pathways rather than direct bond scission:

  - *Hydroperoxide Photolysis:* UV radiation causes the homolytic cleavage of the weak $O-O$ bond in pre-existing hydroperoxides, generating alkoxy ($PO^{\bullet}$) and hydroxyl ($^{\bullet}OH$) radicals. These intermediates serve as vectors: they do not propagate the chain directly but react immediately by abstracting a hydrogen atom from a labile tertiary carbon on a neighboring chain (PH), effectively converting the absorbed energy into a propagation radical ($P^{\bullet}$):

$$POOH \xrightarrow{h\nu} PO^{\bullet} + {}^{\bullet}OH \tag{2.35}$$

$$PO^{\bullet} + PH \rightarrow POH + P^{\bullet} \tag{2.36}$$

  - *Carbonyl Excitation:* Similarly, carbonyl moieties act as sensitizers. Upon absorbing UV photons, they transition to an excited biradical state. This excited species extracts a hydrogen atom from the surrounding matrix, initiating new polymer alkyl radicals ($P^{\bullet}$) ready to enter the propagation loop.

- *Propagation (Chain Growth):* This phase constitutes the core cycle responsible for oxygen consumption and proceeds in two distinct steps. First, the alkyl radical ($P^{\bullet}$) reacts rapidly with molecular oxygen to form a peroxy radical ($POO^{\bullet}$). This reaction is virtually instantaneous and limited only by oxygen diffusion:

$$P^{\bullet} + O_2 \rightarrow POO^{\bullet} \quad \text{(Fast)} \tag{2.37}$$

  Second, the peroxy radical attacks the polymer backbone (PH), specifically targeting tertiary carbons at branching points. This hydrogen abstraction regenerates the alkyl radical ($P^{\bullet}$) and yields a Hydroperoxide ($POOH$). This step represents the rate-limiting step of the entire oxidative process:

$$POO^{\bullet} + PH \rightarrow POOH + P^{\bullet} \quad \text{(Rate Determining)} \tag{2.38}$$

- *Branching (Autocatalytic Acceleration):* From a modeling perspective, the critical feature of this scheme is the fate of the hydroperoxides accumulated during propagation. As described by Bolland, $POOH$ species are thermally and photochemically unstable. Under UV exposure, their decomposition acts as a branching step rather than a termination. The cleavage yields two new active radicals ($PO^{\bullet}$ and $^{\bullet}OH$) from a single parent molecule [60]:

$$POOH \xrightarrow{h\nu} PO^{\bullet} + {}^{\bullet}OH \tag{2.39}$$

  This mechanism creates a positive feedback loop: as the reaction progresses, the concentration of initiating species increases, leading to an exponential rise in the radical population. This physico-chemical reality results in a characteristic

sigmoidal kinetic profile (an induction time followed by auto-acceleration), which provides the physical justification for adopting the *autocatalytic Prout-Tompkins model* (detailed later in Eq. 3.8) to describe the evolution of the internal damage variable ξ. While this parameter will be rigorously defined in the subsequent chapter, it is introduced here as the quantitative index of the degradation process advancement.

2.3.2 Chain Scission and Volatile Generation (Norrish Reactions)

The observable mass reduction, which serves as the primary experimental metric in this first part of the work, stems directly from the fragmentation of the macromolecular backbone. In this context, the Carbonyl moieties ($C = O$) accumulated during the oxidative cycle play a pivotal role. Acting as photo-active centers, they drive the chain scission process through specific photochemical pathways known as *Norrish reactions* [60]:

- *Norrish Type I:* This mechanism entails the homolytic cleavage of the carbon-carbon bond adjacent to the carbonyl group (α-cleavage). This radical fragmentation process frequently yields low-molecular-weight oxygenated byproducts (such as carbon monoxide, short-chain alkanes, or carboxylic acids). Being sufficiently small to diffuse and desorb, these volatile fragments contribute directly to the recorded mass loss.

- *Norrish Type II:* This pathway proceeds via an intramolecular rearrangement involving the abstraction of a γ-hydrogen. The excited state undergoes β-scission, resulting in the formation of a terminal double bond (olefin) and a shortened polymer chain, without necessarily generating immediate radical fragments.

Collectively, these scission events induce a monotonic decrease in the polymer's average molecular weight (M_w). The fragmented "debris" produced by these reactions represent the physical manifestation of the *volatile species (C_v)* explicitly modeled in the Volatile Trapping Hypothesis. Within the context of thin films, the evolution of mass loss is ultimately governed by the kinetic competition between the rate of chemical generation of these volatiles (via Norrish photolysis) and the rate of their physical diffusion towards the free surface.

2.3.3 Chemi-crystallization Phenomenon and Embrittlement

Parallel to the mass reduction phenomena and chemicalchanges, the degradation process in semi-crystalline polymers like LDPE induces significant microstructural rearrangements. In fact, the material undergoes a drastic alteration in its mechanical response, characterized by significant stiffening accompanied by severe embrittlement. This behavior is physically attributed to the phenomenon of *chemi-crystallization* [61, 62]. From a microstructural perspective, the oxidative attack is not uniform but heavily biased towards the disordered phase. Since chain scission events are localized predominantly within the entangled amorphous regions, the tie-molecules that bridge adjacent crystallites are systematically severed. The cleavage of these chains releases shorter macromolecular segments which, liberated from their topological constraints, acquire the necessary mobility to reorganize into a thermodynamically more stable ordered state. Unlike the original long and entangled chains, these shorter segments are free to fold and crystallize onto existing crystal surfaces, forming new, secondary lamellae (lamellar thickening), as shown in Figure 2.12.

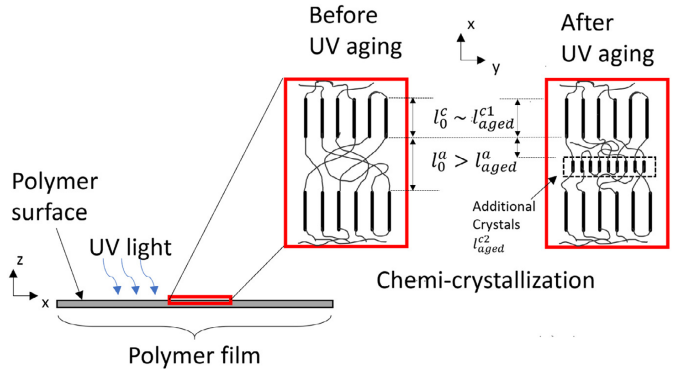

Figure 2.12: Schematic illustration comparing the semi-crystalline microstructure before and after oxidative degradation. The initial state (left) is characterized by a network of entangled tie-molecules that mechanically interconnect adjacent crystalline lamellae. In the degraded state (right), oxidative chain scission severs these inter-lamellar links, causing a loss of connectivity. Simultaneously, the shorter and more mobile chain segments undergo secondary crystallization, resulting in lamellar thickening and an overall increase in material density. Courtesy of Ref. [**63**]

This structural rearrangement leads to a measurable increase in both the overall degree of crystallinity and the material density. However, this densification induces a dual effect:

- It enhances the elastic modulus (stiffness) due to the higher crystalline fraction;
- It critically compromises the material's toughness. The destruction of the inter-lamellar connectivity network (the tie-molecules) removes the mechanism responsible for transferring stress between crystallites, ultimately precipitating macroscopic brittle failure.

Chapter 3

Constitutive Modeling of Photo-Oxidative Degradation in LDPE Nanometric Films

3.1 Introduction and State of Art

Predicting the durability and long-term performance of semi-crystalline polymers represents a critical engineering challenge with implications spanning diverse industrial sectors. The stochastic nature of their morphological evolution under environmental stress imposes severe limitations on the reliability of current predictive models. In this context, the present study specifically targets LDPE. While these materials have long been ubiquitous in terrestrial applications, ranging from photovoltaic encapsulation to agricultural films [64–66], their critical reliance has recently expanded into highly specialized infrastructure and healthcare domains [67, 68]. In the energy sector, polyethylene-based insulation has established itself as the industry standard for high voltage direct current submarine cables, owing to its superior dielectric properties and cost-effectiveness. In this context, minimizing material degradation is paramount for ensuring the reliability of long-distance power transmission [69–71]. Recent investigations have underscored how thermal aging and space charge accumulation, phenomena intrinsically linked to species transport within the polymer matrix, directly compromise the dielectric breakdown strength [72, 73]. Parallel challenges arise in the biomedical field, where the oxidative stability of polymers dictates the clinical lifespan of joint replacements made from ultra-high molecular weight polyethylene [74]. As highlighted in recent literature,

oxidative degradation in these implants drives chain scission and the generation of wear debris, necessitating a profound understanding of diffusion-limited degradation mechanisms in vivo [75, 76]. However, in recent years, the strategic relevance of these materials has found its apex in the aerospace sector. In this extreme frontier, hydrogen-rich polymers like PE are increasingly identified as the optimal matrix for galactic cosmic ray shielding, as well as for critical electrical insulation, protective coatings, and lightweight structural elements, roles established for decades in the industry [77–79]. Yet, as demonstrated by Laurenzi et al. [80], while PE nanocomposites offer superior radiation protection compared to aluminum, their structural integrity remains strictly dependent on their ability to withstand the harsh space environment. Consequently, across these high-stakes sectors, polymer components are mandated to maintain operational reliability over decades despite continuous exposure to oxidative and environmental stressors. In this context, the ability to accurately predict service life transcends economic sustainability, becoming a critical matter of public safety.

Despite the diversity of specific applications, the fundamental degradation phenomenology remains consistent. During their operational service life, these materials are inevitably subjected to harsh environmental drivers, most notably high-intensity UV radiation and atmospheric oxygen. This exposure precipitates *photo-oxidative degradation* [41, 81], driving a complex and irreversible evolution of the material's physico-chemical state. This process is governed by a cascade of competing microscopic mechanisms, described in detail in Section 2.3, including oxidation reactions, free radical formation, chain scission, chemi-crystallization, and cross-linking. Over time, these cumulative molecular alterations lead to a severe deterioration of mechanical integrity, manifesting macroscopically as embrittlement, significant mass loss, the development of internal stresses, and ultimately, surface cracking and catastrophic component failure [82, 83].

To address these complex degradation pathways, the scientific community has shifted towards developing robust constitutive models capable of rigorously capturing the coupling between chemical evolution and changes in physical properties. In recent years, substantial progress has been achieved in establishing thermodynamically consistent frameworks for such coupled chemo-mechanical problems. Notably, the contributions of Alkhoury and Chester [84] and Konica and Sain [85] have set the benchmark in this domain. These works have established rigorous theories for modeling photo-oxidation and oxidative aging, explicitly accounting for the concurrent effects of species diffusion, chemical kinetics, and finite strain deformations. In parallel, foundational frameworks for damage evolution in porous media, such as those proposed by Shakiba et al. [86], have provided the theoretical scaffolding that has inspired similar multiphysics approaches within the specific field of polymer mechanics. To address these durability challenges, the scientific community has devoted significant effort to understanding the kinetics of polymer

degradation. Extensive reviews by Celina and George [42, 58] have documented the fundamental mechanisms of heterogeneous oxidation. However, translating this phenomenological understanding into predictive constitutive models suitable for the thin film regime remains an open challenge.

Currently, existing modeling frameworks are largely bifurcated into two distinct categories:

- *Classical 0D Models:* These approaches typically assume a homogeneous degradation state throughout the material volume. While computationally efficient, they inherently fail to account for the complex transport gradients of reactants and products that arise even within thin layers, leading to inaccurate predictions of the spatial evolution of damage [42, 58].

- *Standard Diffusion-Limited Oxidation (DLO) Models:* Conversely, these models introduce spatial dependency but focus almost exclusively on the limitation of oxygen diffusion into the material. They operate on the premise that the reaction rate in the bulk is throttled by oxygen scarcity, typically resulting in a heterogeneous oxidation profile characterized by a degraded surface and a pristine core [87, 88].

While the standard DLO framework successfully rationalizes the behavior of thicker, millimetric specimens, recent experimental investigations by Najmeddine et al. [63] have highlighted a distinct anomaly in LDPE nanometric films that defies conventional theory. In studying films with a thickness L in the range of $146 - 200\ nm$, the authors observed a severe, non-linear inverse dependency of the mass loss rate on film thickness. Specifically, thicker films were observed to degrade significantly slower per unit mass than thinner ones. This observation presents a fundamental *paradox*. Given the nanoscale dimensions of these specimens, the characteristic diffusion time for oxygen is negligible, ensuring rapid and uniform saturation across the entire cross-section. Under such conditions of homogeneous oxygen availability, standard 0D theory would predict a degradation rate strictly independent of thickness (i.e., a linear scaling). Simultaneously, the fact that the bulk reacts slower than the surface, despite being fully oxygenated, renders the traditional oxygen-DLO assumption invalid for this regime. Instead, this anomaly strongly indicates that the reaction kinetics are being throttled by a transport phenomenon *other* than oxygen ingress, pointing towards the existence of a distinct, overlooked physio-chemical mechanism, identified here as *volatile trapping*, that inhibits the reaction within the bulk material.

To the best of the author knowledge, no constitutive model currently exists in the literature that accounts for the thickness-dependent mass loss kinetics of polymer films in the nanometric regime. Consequently, the non-linear inverse scaling of degradation rate with thickness observed in recent experiments remains

mathematically undescribed and unquantified by current theories.
This work addresses this anomaly by proposing a novel semi-analytical model driven by three specific goals:

1. *Resolving the Thickness-Dependency Anomaly:* The primary objective is to rationalize the counter-intuitive experimental observation that thicker nanometric films degrade significantly slower than thinner ones, a phenomenon physically inexplicable by standard kinetic theories. This trend contradicts classical DLO theories, which are inapplicable in this regime due to the rapid oxygen saturation of the nanometric film. This fundamental mismatch compels the introduction of a novel limiting mechanism independent of oxygen availability.

2. *Formulation of The Volatile Trapping Hypothesis:* To explain the observed inverse thickness dependence, the second objective is to propose and formalize a new physical mechanism based on *product egress*. We introduce the "Volatile Trapping Hypothesis," positing that the rate-limiting transport mechanism is not the ingress of reactants (oxygen), but the outward diffusion of volatile degradation byproducts (e.g., short-chain oligomers). We hypothesize that the local accumulation of these volatiles within the polymer matrix creates a chemical inhibition, consistent with Le Chatelier's principle, effectively throttling the degradation kinetics in the bulk of thicker films.

3. *Establishment of a Quantitative Physical Link for Mass Loss:* Finally, this work aims to elevate the modeling of mass loss from empirical curve-fitting to a robust, physics-based formulation. We develop a semi-analytical model that couples an intrinsic autocatalytic kinetic law (Prout-Tompkins) with analytical solutions for two competing transport processes: light attenuation (Beer-Lambert law) and volatile diffusion (Helmholtz equation). By successfully capturing the degradation kinetics through physically meaningful parameters, specifically the light attenuation coefficient (σ) and the Thiele Modulus for volatiles (Φ), we establish a quantitative link between the macroscopic observable and the underlying microstructure.

3.2 Reference Experimental Framework

As the predictive capability of the computational framework hinges strictly on the accurate representation of the degradation kinetics, the model calibration and validation are grounded on high-quality experimental data available in the literature. Specifically, the experimental campaign detailed by Najmeddine and Shakiba [63] has been selected as the *benchmark dataset*. This choice is motivated by the comprehensive nature of their study, which provides a consistent set of

data linking the photo-oxidative aging conditions, the mechanical response at finite strains, and the fracture behavior.

The following subsections summarize the material properties, the aging protocols, and the mechanical testing procedures adopted in the reference study, which define the physical boundaries of our numerical simulations. For a more comprehensive description of the experimental setup and microstructural characterization, the reader is referred to the original work [63].

Material Identification and Specimen Preparation

The material selected for the reference experimental campaign is a commercial grade LDPE supplied by Sigma-Aldrich. In its pristine state, the polymer is characterized by a density of $\rho = 0.93$ g/cm^3 and a melting temperature of $T_m = 116°$C. Two distinct sets of specimens were prepared to fully characterize the material's behavior. The first set consists of thin films produced via compression molding, resulting in thicknesses in the range of $L \in [30, 80]$ μm. As explicitly stated in the reference study, this specific thickness range was originally selected to ensure homogeneous oxidation across the cross-section (preventing DLO phenomena) while maintaining sufficient structural integrity for mechanical testing (tensile tests) and bulk property analysis. This geometric feature is particularly advantageous for the numerical framework proposed in this thesis, as it allows us to decouple the oxygen diffusion problem (assumed constant) from the volatile species diffusion problem. In parallel, a second set of specimens in the nanometric thickness range was prepared via spin-coating. These ultra-thin films were specifically utilized for Quartz Crystal Microbalance measurements. While the oxidation is assumed homogeneous in both sets, these nanometric samples were necessary to precisely monitor the minute mass loss evolution during aging. Crucially, the experimental data derived from these tests were used to identify the kinetic parameters of the degradation model. These parameters, calibrated exclusively on the nanometric range of the films, particularly, for the 200 nm, were then directly implemented to simulate the degradation behavior of the thicker (30-80 μm) specimens during the mechanical analysis, under the assumption of size-independent oxidation kinetics at this scale.

UV Aging Protocol and Boundary Conditions

The experimental aging was performed in a controlled environment designed to simulate accelerated photo-oxidation while strictly decoupling thermal effects. The samples were exposed to a monochromatic UV source characterized by a wavelength of $\lambda = 254$ nm, specifically selected to activate the Norrish photolysis reactions characteristic of the polyethylene backbone.

The governing parameter for the reaction kinetics, the *UV irradiance intensity*,

was set to a constant value of:

$$I_0 \approx 125\,\mathrm{W/m^2} \tag{3.1}$$

This specific energy flux serves as the primary external driver for the degradation model presented in the following sections.

Throughout the exposure, the specimen temperature was actively maintained at an isothermal condition of $T = 25°\mathrm{C}$. This boundary condition is fundamental for the numerical framework, as it allows for the assumption of constant diffusion coefficients, independent of thermal fluctuations, isolating photo-oxidative effects from pure thermal degradation. The degradation kinetics were monitored over a total exposure period of 112 hours, with intermediate characterization steps performed at $t = 24, 48,$ and 72 hours. This specific aging setup induced the chemical and microstructural changes described in Chapter 2 (chain scission, chemi-crystallization, etc...), leading to the progressive embrittlement of the samples.

Characterization of Damage Metrics

To calibrate the internal state variables of the damage model, specifically the degree of crystallinity (χ_c) and the mass loss ratio (ω), the reference study employed two complementary characterization techniques.

- *Differential Scanning Calorimetry (DSC):* Experiments were performed on *bulk samples* ($30 - 80\,\mu\mathrm{m}$) to quantify the evolution of the degree of crystallinity during the degradation process. Functionally, this technique measures the difference in heat flow required to increase the temperature of the sample compared to a reference. By integrating the endothermic melting peak observed during the heating ramp, the enthalpy of fusion is obtained, which is then normalized against the theoretical enthalpy of 100% crystalline PE to determine the scalar value χ_c, whose evolution over the exposure time is reported in Figure 3.1. The use of bulk thickness ensures the measurement represents the global material behavior, unaffected by surface artifacts.

- *Quartz Crystal Microbalance with Dissipation (QCM-D):* To rigorously validate the Volatile Trapping Model, this high-sensitivity gravimetric technique was employed to monitor the real-time mass loss of ultra-thin films (ranging from 146 to 200 nm). This technique operates as a highly sensitive gravimetric sensor based on the piezoelectric effect: changes in the mass of the polymer film coated on the quartz sensor induce a shift in its resonance frequency. This frequency shift is directly proportional to the mass variation. Hereafter, we define this dimensionless minute mass ratio $\omega = \frac{m(t)}{m_0}$, representing the ratio between the mass at a specific aging time and the initial mass of the

unaged specimen, allowing for the precise, real-time tracking of volatile species release (see Figure 3.2). The use of varying nano-metric thicknesses in this test provides the experimental evidence required to assess the diffusion-limited nature of the phenomenon.

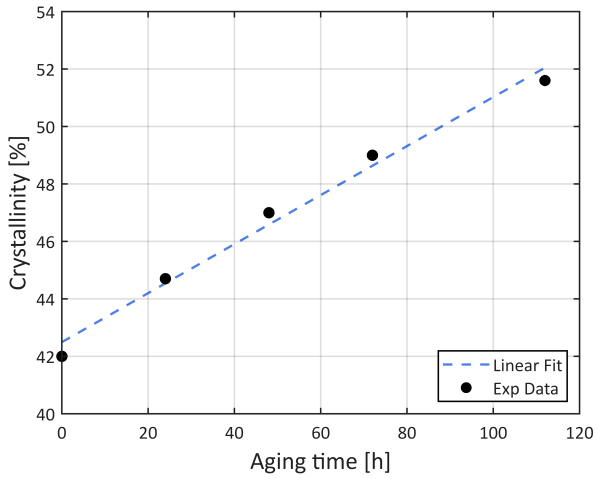

Figure 3.1: Evolution of the degree of crystallinity (χ_c) as a function of UV exposure time, measured via DSC on bulk samples. Adapted from [49].

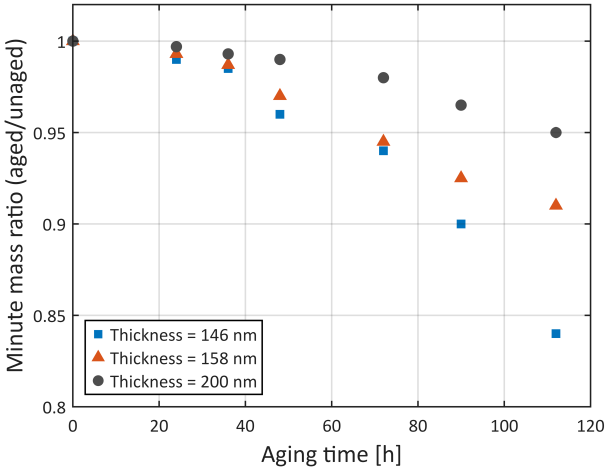

Figure 3.2: Time-dependent mass loss ratio (ω) recorded via QCM-D analysis for thin film specimens. Adapted from [49].

Mechanical Characterization and Failure Analysis

To capture the macroscopic evolution of the material behavior, uniaxial tensile tests were performed until rupture on standardized dumbbell-shaped specimens, strictly adhering to the *ASTM D-638* protocol. This experimental dataset is pivotal for the numerical framework, serving a dual objective: it allows for the calibration of the *viscoelastic constitutive law* and provides the critical threshold values required to validate the *phase-field damage predictions* (elongation at break and fracture energy), that will be discussed in detail in the next chapter. The tests were conducted under displacement control to ensure a stable quasi-static response, imposing a constant nominal strain rate of:

$$\dot{\varepsilon} = 4 \times 10^{-3} \, [\mathrm{s}^{-1}] \tag{3.2}$$

Experimental reproducibility was guaranteed by performing a minimum of three repetitions for each aging condition on both pristine and photo-oxidized films. Crucially, the resulting stress-strain curves reported in the reference article [63] document the progressive loss of ductility, manifesting as a transition from extensive necking to brittle failure. As discussed later in Chapter 4, these results provide the *empirical ground truth* against which the computational model will be benchmarked.

3.3 The Volatile Trapping Hypothesis

The constitutive framework developed in this chapter is a semi-analytical, physics-based model designed to rigorously quantify the relationship between photo-chemical degradation processes and the primary macroscopic observable: the mass loss (ω). As detailed in the previous section, the experimental data reveals a severe thickness dependency in nanometric films that classical reaction-limited or diffusion-limited assumptions fail to capture.

3.3.1 Conceptual Framework and Constitutive Assumptions

To resolve this anomaly, the model relies on a specific set of physical postulates that define the "Volatile Trapping" mechanism:

1. *Homogeneous Oxygen Saturation:* Given the nanometric scale of the films, we explicitly assume that oxygen diffusion is non-limiting. As supported by literature [63, 89–91], the oxygen concentration is considered uniform across the film thickness. This effectively decouples the oxidation kinetics from oxygen transport.

2. *Product-Limited Kinetics:* We posit that the rate-limiting step for mass loss is the subsequent mass transport (diffusion) of *volatile degradation products* out of the polymer matrix.

3. *Inhibition via Accumulation:* The model couples the intrinsic chemical kinetics with analytical solutions for volatile diffusion. In thicker films, the longer diffusion path causes a local accumulation of volatiles. This accumulation acts as a chemical inhibitor (via Le Chatelier's principle), retarding the forward reaction rate compared to thinner films where volatiles escape instantaneously.

3.3.2 Physical Justification: Analogies with Diffusion-Limited Systems

While the specific modeling of volatile trapping in LDPE represents a novel contribution, the fundamental physical principle, that reaction kinetics can be rate-limited by the diffusion of their own byproducts, is a well-established phenomenon in analogous reactive systems. Validation of this mechanism can be found across diverse fields:

- *Biodegradable Polymers (Autocatalysis via Product Accumulation):* Strong experimental evidence exists in the hydrolysis of biodegradable polymers like Poly(lactic-co-glycolic) Acid, more commonly known as PLGA. As discussed by Han and Voinova et al. [92], the degradation rate of bulk specimens is often controlled not merely by water ingress, but by the outward diffusion of acidic oligomers. The accumulation of these reaction products within the core creates distinct core-shell degradation profiles strictly governed by sample thickness.

- *Biological Systems (Physical Barrier Inhibition):* In biochemical engineering, Pereira et al. [93] provided explicit evidence of mass transfer limitations caused by product accumulation during the anaerobic biodegradation of fatty acids. They demonstrated that the buildup of long chain fatty acids creates a physical barrier that hinders substrate transfer, effectively throttling the reaction kinetics.

- *Biomedical Implants (Depth-Dependent Oxidation):* Similarly, the oxidation of ultra-high molecular weight polyethylene implants in vivo exhibits depth-dependent profiles that cannot be explained solely by oxygen diffusion. Currier et al. [75] showed that oxidation patterns suggest a complex interplay where product accumulation modifies the reaction environment deep within the material.

- *Electrochemical Systems (Gas Diffusion Electrodes):* Furthermore, "product inhibition" models are standard in electrochemistry. Kopljar [94] highlights

that in gas diffusion electrons, the accumulation of reaction products within the porous structure becomes the rate-limiting step at high currents, hindering transport and reducing overall efficiency.

By extending these validated physical concepts to the photo-oxidation of LDPE, we provide a sound physical basis for the mathematical formulation presented in the following section.

3.4 Mathematical Formulation

3.4.1 Governing Equation: The Volatile Mass Balance

The core of the Volatile Trapping Hypothesis is that the local degradation rate is physically controlled by the transient concentration of its own reaction byproducts. Therefore, the mathematical foundation of this framework is the law of conservation of mass applied to these volatile species. The spatio-temporal evolution of the local volatile concentration, $C_v(z,t)$, which is treated as a dynamic field, is governed by a one-dimensional partial differential equation (PDE) of the reaction-diffusion type. This mass balance equation states that the rate of accumulation of volatiles at any depth z is the sum of the net diffusive transport flux and the local generation rate:

$$\underbrace{\frac{\partial C_v}{\partial t}}_{\text{Accumulation term}} = -\frac{\partial J_{flux}}{\partial z} + \text{Generation term} \tag{3.3}$$

Assuming a transport mechanism based on Fick's law, the equation is specified as follows:

$$\frac{\partial C_v}{\partial t} = \underbrace{D_{vol}\frac{\partial^2 C_v}{\partial z^2}}_{\text{Diffusion (Fick's Law)}} + \underbrace{\gamma \cdot \text{Rate}_{real}(z,t)}_{\text{Generation Source}} \tag{3.4}$$

Where the primary transport parameters are:

- D_{vol}: The effective diffusion coefficient of the volatile byproducts through the polymer matrix.
- γ: A stoichiometric generation coefficient that links the reaction extent rate to the volumetric production rate of C_v.
- $\text{Rate}_{real}(z,t)$: The actual, local rate of the degradation reaction, which acts as the source term for volatiles.

3.4.2 Constitutive Laws: Coupling Generation and Inhibition

The mass balance equation (Eq. 3.4) requires a robust constitutive definition for the source term, Rate_{real}. Unlike simple diffusion problems characterized by constant generation, the degradation rate in this framework is strictly coupled to the local physics. We posit that the actual reaction rate is the result of a competition between a *"driving force"* (derived from potential chemistry and UV energy) and a *"resistive force"* (derived from volatile inhibition).

The Inhibition Mechanism (Le Chatelier's Principle)

As mentioned before, the central tenet of the Volatile Trapping Hypothesis is that the degradation kinetics are physically throttled by the accumulation of their own reaction byproducts. We postulate that the local, transient concentration of volatile species, $C_v(z,t)$, creates a "back-pressure" that hinders the forward progress of the reaction. This inhibitory mechanism is modeled as a direct phenomenological application of *Le Chatelier's Principle*. To formalize this, we introduce a linear inhibition factor based on the local volatile concentration relative to a material-specific saturation concentration, C_{sat}. The actual local rate of reaction, $\text{Rate}_{real}(z,t)$, is thus defined as the potential rate penalized by this factor:

$$\text{Rate}_{real}(z,t) = \text{Rate}_{pot}(z,t) \cdot \underbrace{\left(1 - \frac{C_v(z,t)}{C_{sat}}\right)}_{\text{Inhibition Factor}} \tag{3.5}$$

Physically, this constitutive relation enforces a thermodynamic limit on the kinetics. In the limit of vanishing volatile concentration ($C_v \ll C_{sat}$), the system operates in a purely kinetically-controlled regime ($\text{Rate}_{real} \to \text{Rate}_{pot}$). Conversely, as the local concentration approaches the saturation threshold ($C_v \to C_{sat}$), the net reaction rate asymptotically vanishes, reflecting a state of local equilibrium where the chemical driving force is effectively nullified.

The Driving Force: Potential Rate and Light Attenuation

The term $\text{Rate}_{pot}(z,t)$ represents the ideal reaction rate that would occur at a specific depth z if no volatile inhibition existed (i.e., if all byproducts were instantaneously removed). Since the reaction is photo-initiated, this potential rate is modulated by the local light intensity $I(z)$, which attenuates as it penetrates the material according to the *Beer-Lambert law*:

$$I(z) = I_0 \cdot exp[-\sigma(L - z)] \tag{3.6}$$

Here, L represents the film thickness, I_0 is the incident intensity at the exposed surface ($z = L$), and σ is the light absorption coefficient. Consequently, the spatially-dependent driving force is defined as:

$$\text{Rate}_{pot}(z,t) = \text{Rate}_{chem}(\xi) \cdot \frac{I(z)}{I_0} \tag{3.7}$$

Internal State Variable and Intrinsic Kinetics

Finally, the term $\text{Rate}_{chem}(\xi)$ describes the inherent reactivity of the polymer matrix. The framework is built upon the definition of a primary *internal state variable*, denoted as ξ, representing the *internal reaction extent*. A fundamental hypothesis of this formulation is the decoupling of this intrinsic chemical process from the macroscopic, observable metric of mass loss. We posit that ξ represents the true local progress of the underlying photo-oxidative mechanisms (e.g., chain scission, chemi-crystallization), whereas mass loss is a secondary, transport-limited consequence. Measurable mass loss only occurs when the volatile byproducts generated by ξ successfully diffuse and escape from the free surface. The evolution of ξ is governed by a constitutive kinetic law based on the *Prout-Tompkins autocatalytic model* [95, 96]. The intrinsic chemical rate is defined as:

$$\text{Rate}_{chem}(\xi) = \dot{\xi} = K_{chem} \cdot (\xi + \xi_{init})^g \cdot (1 - \xi)^n \tag{3.8}$$

Where K_{chem} is the intrinsic chemical rate constant. While generally following an Arrhenius temperature dependency, the experimental data utilized in this work were obtained under strictly isothermal conditions (Section 3.2). Under this constraint, K_{chem} is treated as a single, lumped scalar parameter to be calibrated. Furthermore, to focus purely on the autocatalytic generation phase where the polymer substrate is in vast excess, we simplify the model by setting the depletion exponent $n = 0$ and the autocatalytic exponent $g = 0.5$. This leads to the final constitutive form for the intrinsic chemistry:

$$\text{Rate}_{chem}(\xi) = \dot{\xi} = K_{chem} \cdot (\xi + \xi_{init})^{0.5} \tag{3.9}$$

The system described by Eq. 3.9, Eq. 3.5, and Eq. 3.4 forms a fully coupled PDE-ODE problem, where the generation term depends on both the diffusing species (C_v) and the evolving microstructure (ξ) of the material.

3.4.3 Analytical Simplification via Quasi-Steady-State (QSS) Assumption

As mentioned previously, the coupled PDE-ODE system presents a significant computational challenge. Solving it directly would require a fine spatial discretization and complex transient solvers. Therefore, the objective of this work is not to develop a full numerical simulation, but rather to propose a semi-analytical, physics-based framework. Crucially, this approach seeks to move beyond empirical curve-fitting; the governing parameters are rigorously derived from thermodynamic principles to bridge the gap between:

1. *Classical 0D Models:* Which fail to capture the thickness-dependent physics.
2. *Full PDE Models:* Which are computationally intensive and obscure the relationship between parameters and macroscopic response.

To create the simplest possible model that captures the dominant mechanisms (light attenuation and volatile trapping), we introduce a critical simplification: the *QSS assumption* for volatile transport. This is based on a separation of timescales: the characteristic time for volatile diffusion ($\tau_{diff} \approx L^2/D_{vol}$) is significantly shorter than the timescale of the oxidative reaction (τ_{chem}). This implies that the volatile concentration profile $C_v(z,t)$ instantaneously adapts to the current reaction rate. Mathematically, this allows us to set the accumulation term in the PDE (Eq. 3.4) to zero:

$$\frac{\partial C_v}{\partial t} \approx 0 \tag{3.10}$$

Physically, this QSS assumption elegantly decouples the spatial and temporal domains: the spatial diffusion problem is solved statically to evaluate the geometric penalty imposed by the film thickness, while the chemical degradation is allowed to evolve dynamically over time. By substituting the constitutive law for the reaction rate (Eq. 3.5) into this steady-state diffusion equation, and introducing the dimensionless *availability factor* $u(z) = \left(1 - \frac{C_v(z)}{C_{sat}}\right)$, we arrive at the standard *modified Helmholtz equation*:

$$\frac{d^2u}{dz^2} = \frac{\Phi^2}{L^2}u(z) \tag{3.11}$$

Here, Φ is the *Thiele modulus*, a critical dimensionless parameter representing the competition between reaction and diffusion. By expliciting the geometric dependence on the film thickness L, the modulus can be expressed as:

$$\Phi = \sqrt{\frac{\tau_{diff}}{\tau_{chem}}} = L\sqrt{\frac{\gamma \cdot \text{Rate}_{pot}}{D_{vol} \cdot C_{sat}}} = \phi_0 \cdot L \tag{3.12}$$

where ϕ_0 is introduced as the *Thiele modulus constant*. This parameter isolates the intrinsic material and kinetic properties from the macroscopic geometry:

$$\phi_0 = \sqrt{\frac{\gamma \cdot \text{Rate}_{pot}}{D_{vol} \cdot C_{sat}}} \tag{3.13}$$

Here, Rate_{pot} acts as a characteristic, constant reference rate (strictly proportional to K_{chem}) rather than the instantaneous dynamic rate. This ensures that ϕ_0 evaluates the baseline severity of the diffusion barrier independently of the current reaction extent. Because ϕ_0 remains invariant across different film thicknesses under the same environmental conditions, it serves as an ideal global parameter to be identified via model calibration.

3.4.4 Analytical Solution via Linearization and Boundary Conditions

To obtain a closed-form analytical solution, we introduce the linearization assumption that the Thiele modulus, Φ, can be treated as a constant parameter across the film thickness. This simplification lumps the spatially-dependent competition between reaction and diffusion into a single effective parameter, capturing the mean-field behavior of the system. Solving Eq. 3.11 with the physical boundary conditions ($u(L) = 1$ at the free surface, $du/dz|_{z=0} = 0$ at the impermeable substrate) yields the exact solution for the reaction availability profile:

$$u(z) = \frac{\cosh(\Phi \cdot z/L)}{\cosh(\Phi)} \tag{3.14}$$

This function describes the physical profile of inhibition: the reaction is fully active at the surface ($u(L) = 1$) and maximally inhibited at the substrate ($u(0) = 1/\cosh(\Phi)$).

3.4.5 The Diffusive Effectiveness Factor (η_{diff})

To link the local inhibition profile to the macroscopic mass loss, we define the *diffusive effectiveness factor* (η_{diff}) as the ratio of the average real rate to the potential rate across the film thickness:

$$\eta_{diff} = \frac{\overline{\text{Rate}}_{real}}{\text{Rate}_{pot}} = \frac{1}{L}\int_0^L u(z)dz \tag{3.15}$$

Integrating the solution $u(z)$ (Eq. 3.14) yields the classic effectiveness factor for a flat plate geometry [97]:

$$\eta_{diff}(\Phi) = \frac{\tanh(\Phi)}{\Phi} \tag{3.16}$$

This single dimensionless parameter quantifies the total impact of volatile trapping. If $\Phi \to 0$ (fast diffusion), $\eta_{diff} \to 1$ (no inhibition). If $\Phi \to \infty$ (slow diffusion), $\eta_{diff} \to 0$ (severe inhibition).

3.4.6 The Light Effectiveness Factor (η_{light})

In parallel, we homogenize the non-uniform UV distribution by defining the *light effectiveness factor* (η_{light}), calculated by integrating the Beer-Lambert law across the thickness:

$$\begin{aligned}\eta_{\text{light}}(L) = \frac{\text{Average Light Intensity}}{\text{Maximum Light Intensity}} = \frac{1}{L}\int_0^L \frac{I(z)}{I_0} dz = \\ = \frac{1}{L}\int_0^L \exp[-\sigma(L-z)]dz = \frac{1-\exp(-\sigma L)}{\sigma L}\end{aligned} \tag{3.17}$$

This factor quantifies the reduction in global rate due to light attenuation.

3.4.7 The Final Analytical Model

We now formulate the final constitutive model considering the average extent of reaction rate ($\dot{\xi}_{avg}$). The global rate is modeled as the intrinsic autocatalytic potential, penalized by the two physical efficiency factors acting in series:

$$\dot{\xi}_{avg} = \underbrace{K_{chem}(\xi_{avg} + \xi_{init})^{0.5}}_{\text{Intrinsic Chemistry}} \cdot \underbrace{\eta_{light}(L)}_{\text{Light Attenuation}} \cdot \underbrace{\eta_{diff}(\Phi(L))}_{\text{Volatile Trapping}} \tag{3.18}$$

This allows us to define a single *effective rate constant*, K_{eff}, which encapsulates all physical inhibitions and depends explicitly on the film thickness L:

$$K_{eff}(L) = K_{chem} \cdot \eta_{light}(L) \cdot \eta_{diff}(\Phi(L)) \tag{3.19}$$

Substituting this into the kinetic law, the complex PDE-ODE system is reduced to a single 0D ODE for the evolution of the average reaction extent:

$$\dot{\xi}_{avg}(t) = K_{eff}(L) \cdot (\xi_{avg} + \xi_{init})^{0.5} \tag{3.20}$$

Finally, the predicted mass loss $\omega(t)$ is linearly linked to the internal state variable via a scaling factor $A_{\max}$, which statistically accounts for the mass loss recorded for the same material under identical degradation conditions:

$$\omega_{pred}(t) = 1 - A_{max} \cdot \xi_{avg}(t) \tag{3.21}$$

The model is thus governed by four key physical parameters to be determined via calibration: K_{chem} (intrinsic chemical rate), σ (light absorption coefficient), ϕ_0 (Thiele modulus constant), and A_{max} (mass loss scaling factor).

3.5 Model Validation and Results

The complete semi-analytical model, defined by the coupling of the ODE governing the average reaction extent (3.20) and the macroscopic mass loss linkage (3.21), was calibrated against the experimental dataset provided by Najmeddine et al. [63]. The primary objective of this validation procedure was to identify the optimal set of the four governing physical parameters that simultaneously minimizes the error between the predicted mass loss and the experimental data points across all three investigated film thicknesses (146 nm, 158 nm, and 200 nm). The optimization was executed using a standard non-linear least squares algorithm. The resulting optimal parameter set is detailed in Table 3.1.

Parameter	**Symbol**	**Value**	**Unit**	**Description**
Intrinsic Chemical Rate	K_{chem}	3.73×10^{-1}	h^{-1}	Base reaction rate constant
Light Absorption Coeff.	σ	4.73×10^{7}	m^{-1}	Beer-Lambert absorption coeff.
Thiele Modulus Const.	ϕ_0	2.85×10^{7}	m^{-1}	Thiele constant ($\Phi = \phi_0 \cdot L$)
Mass Loss Amplitude	A_{max}	0.2757	–	Max. mass loss scaling factor

Table 3.1: Optimized physical parameters for the Volatile Trapping Model.

The calibrated parameters exhibit strong physical consistency with the phenomenology of accelerated photo-oxidation. Specifically, the high magnitude of the Thiele modulus constant (ϕ_0) confirms that the process operates in a strongly diffusion-limited regime ($\Phi > 1$) even at the nanometric scale, validating the central hypothesis of volatile trapping. Furthermore, the intrinsic reaction rate constant (K_{chem}) aligns with typical timescales of accelerated aging tests reported in literature [98], indicating that the model correctly captures the chemical kinetics without requiring unphysical adjustment factors. These optimized parameters were

subsequently employed in the forward (predictive) model to simulate the mass loss evolution for each thickness. The resulting model predictions are plotted against the experimental data in Figure 3.3.

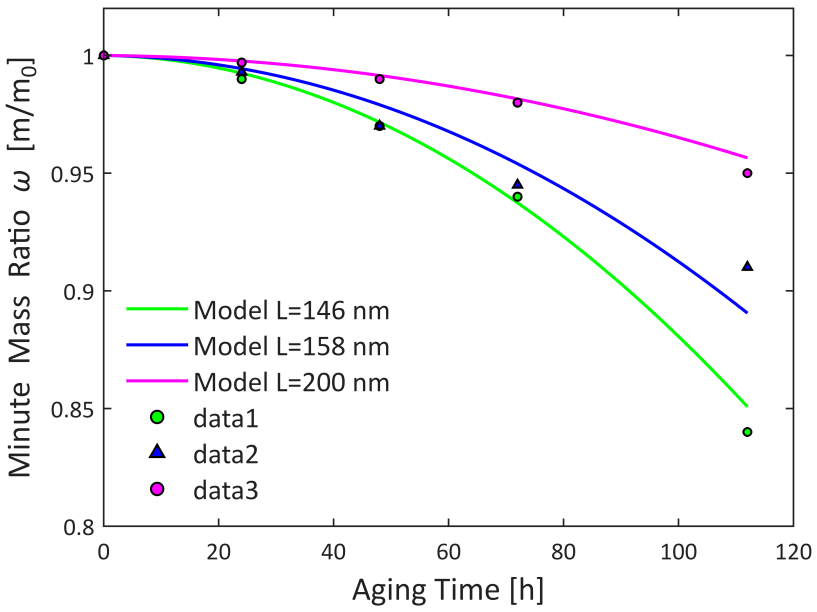

Figure 3.3: Validation of the final Volatile Trapping Model. Lines represent the model predictions (Eq. 3.21) using the single set of parameters from Table 3.1. Solid markers represent the experimental data points from [63] for 146 nm, 158 nm, and 200 nm films.

The results demonstrate an excellent agreement between the model predictions and the experimental observations. Crucially, the model successfully captures the strong, non-linear thickness dependency of the mass loss, the primary anomaly this work aimed to resolve. The curves correctly reproduce the physical behavior where thicker films (e.g., 200 nm) exhibit significantly slower degradation kinetics compared to thinner films (e.g., 146 nm). This successful validation confirms the central tenet of this framework: the anomalous thickness-dependency in these thin films is governed by the coupled competition between two physical mechanisms: *light attenuation* (quantified by σ) and *volatile trapping* (quantified by ϕ_0).

3.6 Concluding Remarks

In this chapter, we presented a physics-based semi-analytical framework to model the anomalous thickness-dependent photo-oxidation kinetics observed in nanometric LDPE films. Standard kinetic theories, based on the DLO, fail to predict the behavior of films in this geometric regime, where oxygen saturation is instantaneous and homogeneous. Contrary to classical expectations, experimental evidence revealed that thicker films degrade significantly slower per unit mass than thinner ones. To resolve this discrepancy, we introduced the *Volatile Trapping Hypothesis*. We demonstrated that the rate-limiting transport mechanism is not the ingress of reactants, but the egress of volatile reaction byproducts generated by chain scission. By coupling intrinsic autocatalytic kinetics (Prout-Tompkins) with an analytical solution for product diffusion (Helmholtz equation), we derived a new dimensionless group, the *Thiele modulus*, which quantifies the competition between volatile generation and their diffusive removal. The model was successfully calibrated and validated against experimental data, accurately capturing the non-linear thickness dependency that standard models could not explain. This result confirms that the local accumulation of degradation products creates a thermodynamic inhibition (Le Chatelier effect) that effectively "traps" the reaction in the bulk of the material. This study bridges a critical gap in the literature, providing the first constitutive link between microscopic chemical kinetics and the macroscopic mass loss observable for thin films. By defining mass loss as a function of the *internal state variable* (ξ), this framework lays the foundation for the chemo-mechanical analysis. With the degradation kinetics physically described, the focus now shifts to the numerical prediction of structural failure. The following Chapter 4 introduces the phase-field fracture framework, explicitly coupled with the viscoelastic constitutive theories discussed earlier in this chapter. While the full implementation of the chemical kinetic model is reserved for future developments, the computational strategy presented next, unifying time-dependent bulk mechanics with diffuse crack propagation, provides the essential mechanical solver required to predict the embrittlement and service-life of polymer components.

Chapter 4

Numerical Modeling of Viscoelastic Behavior and Fracture

4.1 State of the Art in Constitutive Modeling of Polymers

The constitutive modeling of semi-crystalline polymers has undergone significant evolution, transitioning from classical linear viscoelasticity to sophisticated frameworks capable of capturing finite deformations, hysteresis, and environmental degradation. Modern constitutive theories are grounded in the kinematics of finite deformations, where the material response is typically decomposed into an equilibrium hyperelastic branch and a non-equilibrium viscous branch. To capture the rate-dependent behavior combined with large strains, the standard kinematic assumption involves the multiplicative decomposition of the deformation gradient ($\mathbf{F} = \mathbf{F}_e\mathbf{F}_v$) in an elastic and viscous part, a concept originally formalized by Lee [99] and successfully implemented in the seminal works of Reese and Govindjee [100] and Bergstrom and Boyce [101]. These foundational frameworks established the ability to predict complex mechanical histories but were originally limited to chemically stable microstructures, treating material parameters as time-invariant or solely temperature-dependent. In recent years, however, the modeling literature has focused on extending finite-strain theories to capture 'active' material behaviors, with particular attention devoted to coupled theories for shape memory polymers, dielectric elastomers, and gels, to mention some, where mechanical deformation is intrinsically driven by non-mechanical stimuli. Foundational work on the rigorous thermodynamic coupling of transport phenomena and large deformations was established by Chester and

Anand, whose contributions on fluid permeation [102, 103] and thermo-mechanical coupling [104] defined the standard for deriving constitutive laws directly from the dissipation inequality involving species concentration and temperature. This thermodynamic rigor has been extensively adopted to model phase transitions in active materials. Early consistent approaches, such as those by Baghani et al. [105], established the energetic basis for shape memory cycles. Subsequent works refined the kinematic description: for instance, Park et al. [106] and Li et al. [107] successfully extended the multiplicative decomposition framework to isolate shape-memory strains from the viscoelastic response. More recently, this field has seen further advancements with Xue et al. [108], who introduced a thermodynamic model based on phase transition kinetics, and with Rezaei et al. [109] and Zhang and Hu [110], who explored complex couplings between viscoelasticity and soft elasticity. While these frameworks demonstrate the power of the thermodynamic approach in capturing the multi-physics behavior of polymeric materials, their scope remains fundamentally limited. Specifically, they are primarily designed to describe *reversible* physical transitions, thereby lacking the necessary formulations to account for the *irreversible* chemical degradation and permanent embrittlement associated with environmental aging. This limitation is critical, as polymers in real-world applications are rarely chemically inert. As highlighted in recent literature reviews, the scope of constitutive modeling must necessarily expand to include the wide array of chemical reactions that occur during service life. Significant efforts have been directed towards modeling degradation processes, such as hydrolytic degradation [111–113], thermal degradation [114, 115], and specifically photo-oxidative degradation [42, 85, 116, 117], including recent contributions on oxidation-induced embrittlement [63, 118]. From a foundational theoretical perspective, modeling these chemically reacting polymers requires sophisticated tools. Based on robust frameworks like those of Gurtin et al. [45], it is becoming increasingly apparent that in reacting systems, the Second Law of Thermodynamics requires careful treatment. As foresighted by Truesdell and Toupin [119], the change in entropy cannot be solely attributed to heat flow; other phenomena, most notably the transport of species due to diffusion, must actively contribute to the entropy inequality. Recent efforts have successfully formalized this concept. Long and co-workers [120] formulated a kinetic framework that accounts for entropy changes induced by radiative transfer, while other studies focused on developing thermodynamically consistent transport-reaction-mechanics models for materials undergoing small and large deformations with species trapping, incorporating the effect of species transport on the entropy imbalance [121, 122]. Despite these theoretical advances, engineering applications have historically relied closer on phenomenological approaches to handle damage and aging. Notably, the work of Westbrook et al. [123] provided a comprehensive 3D constitutive model for amorphous polymers, capturing yield behavior accurately. In the specific context of oxidative degradation, Najmeddine et al. [49, 63] and

Sain et al. [124] have set the engineering benchmark. By introducing experimentally calibrated damage functions, these models achieve remarkable accuracy in reproducing stress-strain data of photo-oxidized polymers. Nevertheless, these phenomenological models often lack the rigorous thermodynamic foundation discussed above. They describe the macroscopic effects of aging without explicitly modeling the energetic cause, which limits their extensibility to complex fracture problems where the calculation of energy release rates is paramount. To bridge this specific gap, combining the thermodynamic consistency of active material models with the irreversible physics of degradation, the present thesis adopts a strategy inspired by recent chemo-mechanical developments [125]. We propose a framework where the oxidative kinetics (Chapter 3) directly inform the free energy of the system, extending the approach to encompass not only viscoelastic bulk degradation but also the nucleation and propagation of cracks through a phase-field approach.

4.2 Statement of the Coupled Boundary Value Problem

As extensively derived in section 2.1, the mechanical response and the fracture evolution of the polymer are governed by a coupled system of PDEs. For the sake of clarity in the subsequent numerical formulation, we summarize here the strong form of the boundary value problem in the reference configuration Ω_0. Neglecting inertial effects, the coupled chemo-mechanical problem is defined by the simultaneous satisfaction of the linear momentum balance and the phase-field evolution equation:

$$\begin{cases} \mathrm{Div}(\mathbf{P}) + \bar{\mathbf{b}} = \mathbf{0} \\ \dfrac{G_c}{c_\alpha}\left(\dfrac{\alpha'(d)}{l_c} - 2l_c\Delta_{\mathbf{X}} d\right) + \omega'(d)\psi_{0(\mathbf{C})} = 0 \end{cases}, \text{ in } \Omega_0 \tag{4.1}$$

Here, the first equation represents the mechanical equilibrium, where $\mathbf{P}$ is the First Piola-Kirchhoff stress tensor and $\bar{\mathbf{b}}$ is the body force vector. The second equation governs the diffusive crack topology, where G_c is the critical fracture toughness, l_c is the regularization length scale, and $\psi_{0(\mathbf{C})}$ represents the energetic driving force (strain energy density of the undamaged solid).

This system is completed by the following set of boundary conditions on the boundary $\partial\Omega_0 = \Gamma_u \cup \Gamma_t \cup \Gamma_d$:

- **Mechanical:** $\mathbf{u} = \bar{\mathbf{u}}$ on Γ_u and $\mathbf{P}\mathbf{m} = \bar{\mathbf{t}}$ on Γ_t.
- **Phase-Field:** $\nabla_{\mathbf{X}} d \cdot \mathbf{m} = 0$ on $\partial\Omega_0$ (homogeneous Neumann condition).

4.2.1 Specific Constitutive Choices for Fracture

To render the governing equations system (Eq. 4.1) solvable, the constitutive functions characterizing the fracture topology and the material degradation must be specified. In fact, these are the 2 parameters that differentiate the different versions of the phase-field. In this study, we adopt a linear geometric crack function $\alpha(d) = d$ (often referred to as the AT1 model). This specific formulation is critical as it allows the material to develop purely elastically up to a defined critical energy threshold, avoiding the non-physical artifact of premature damage evolution before crack nucleation. This choice is physically driven by the fracture mechanics of the polymer systems under investigation. Even unaged elastomers typically exhibit a purely nonlinear elastic response up until rupture; damage does not commence until the material reaches a critical energy state where enough load-bearing chains are broken. Crucially, this threshold-based behavior becomes even more pronounced under severe chemical aging: as the material undergoes embrittlement, it tends to show an almost linear elastic response (under quasi-static loading) until it reaches the critical capacity, resulting in abrupt fracture nucleation due to bond breakage. By adopting $\alpha(d) = d$, our model accurately captures this "elastic-then-brittle" transition [50, 126], preventing the artificial softening at low strains that is characteristic of alternative phase-field formulations (e.g., $\alpha(d) = d^2$). Complementarily, the degradation function is defined as $\omega(d) = (1 - d)^2$. This quadratic form ensures a monotonic and smooth decay of the material's load-bearing capacity as the phase-field parameter evolves from zero (intact state) to unity (fully fractured state). Consequently, the normalization constant c_α, which scales the regularized dissipated energy to match the critical fracture toughness G_c, is computed as follows:

$$c_\alpha = 4 \int_0^1 \sqrt{\alpha_{(\beta)}}\, d\beta \tag{4.2}$$

Within the proposed thermodynamic framework, the elastic contribution to the free energy is derived assuming a non-Gaussian chain statistics. To link the microscopic chain stretch to the macroscopic deformation invariants, we adopt the kinematic assumption of the eight-chain topology. Consequently, the structural parameter c_α is set to 8/3, ensuring isotropic averaging of the network response. Finally, the length scale parameter l_c serves as the regularization term defining the width of the smeared crack band. Within this framework, l_c is not treated merely as a numerical artifact for mesh objectivity, but as an intrinsic material property that may evolve with the aging conditions, reflecting the changing internal structure of the polymer.

4.3 Constitutive Framework Coupling Viscoelasticity and Phase Field for Photo-Oxidated Semicrystalline Polymers

The system of partial differential equations presented in Section 4.2 provides the general kinematic and topological shell for the problem. However, to transform this into a predictive tool for aging polymers, the abstract energetic terms appearing in Eq.(4.1) must be specialized. Specifically, we need to define the explicit functional forms of the *Helmholtz free energy density* $\psi(\mathbf{C}, \dots)$, which dictates the viscoelastic stress response, and the *critical energy release rate* G_c, which establishes the fracture threshold.

In this section, we advance a constitutive formulation specifically tailored for semicrystalline polymers undergoing photo-oxidative aging. A distinct feature of this framework is its departure from purely empirical and phenomenological approaches often found in the literature. Rather than adopting ad-hoc phenomenological decay functions to describe the loss of stiffness or toughness over time, we propose a *thermodynamically consistent strategy*. Here, the material properties are treated as intrinsic functions of the physio-chemical state of the material ensuring that the mechanical degradation is energetically driven by the underlying macromolecular scission. Furthermore, to ensure the model remains computationally efficient and applicable to engineering components without demanding prohibitive experimental calibration, we introduce a *streamlined constitutive model*. By focusing on the dominant deformation mechanisms, this formulation retains the theoretical rigor of full-network theories (mainly based on the extensive body of work developed by Oscar Lopez-Pamies' research group [125, 127]) while significantly reducing the number of material parameters required.

4.3.1 Two Potentials Formalism

To consistently describe the rate-dependent behavior of the semicrystalline polymer under finite strains, the constitutive formulation is grounded in the framework of thermodynamics with internal variables evolution. This approach is adopted to ensure that the constitutive laws inherently satisfy the Second law of Thermodynamics, specifically the Clausius-Duhem dissipation inequality mentioned previously. Furthermore, using scalar potentials to derive the stress response provides a robust method to capture both the energy storage mechanisms (elasticity) and the dissipative processes (viscosity) characteristic of the material. Accordingly, we postulate the existence of two thermodynamic potentials [125, 128–131], under the assumption to consider our material homogeneous and isotropic. The first potential is the Helmholtz free energy density per unit undeformed volume, ψ,

which acts as the potential for the viscoelastic stress response and describes how the elastomer stores energy through elastic deformation. To distinguish between the equilibrium response of the polymer network and the transient relaxation effects, ψ is decomposed additively into an equilibrium part (ψ^{Eq}) and a non-equilibrium part (ψ^{NEq}):

$$\psi(\mathbf{F}, \mathbf{C}^v) = \psi^{\mathrm{Eq}}(I_1, J) + \psi^{\mathrm{NEq}}(I_1^e, J) \tag{4.3}$$

where we recall that $\mathbf{F}$ is the deformation gradient described before, $I_1 = tr\mathbf{C}$ is the first invariant of the right Cauchy-Green tensor, $\mathbf{C} = \mathbf{F}^T\mathbf{F}$, and $J = \det \mathbf{F}$ is the Jacobian determinant. Physically, formulating the energy in terms of these invariants ensures an objective, coordinate-independent measure of the deformation, satisfying the principle of material frame indifference. Crucially for the present formulation, the variable $\mathbf{C}^v$ represents the viscous second-order right Cauchy-Green tensor, which acts as the internal variable describing the inelastic deformation of the microstructure, standing for a measure of the viscous part of the deformation gradient $\mathbf{F}$. Consequently, $I_1^e = \mathrm{tr}(\mathbf{C}(\mathbf{C}^v)^{-1})$ represents the elastic invariant associated with the non-equilibrium branch.

This additive decomposition allows for a straightforward rheological interpretation. Consistent with the mathematical models discussed in section 2.2, the material response can be visualized as a finite-strain generalization of the *Zener model (or SLS)*. It consists, as shown in Figure 4.1, of a non-linear equilibrium spring (representing ψ^{Eq}) in parallel with a Maxwell element. The Maxwell element itself comprises a non-linear non-equilibrium spring (representing ψ^{NEq}) in series with a dashpot, whose behavior is governed by the dissipation potential described below.

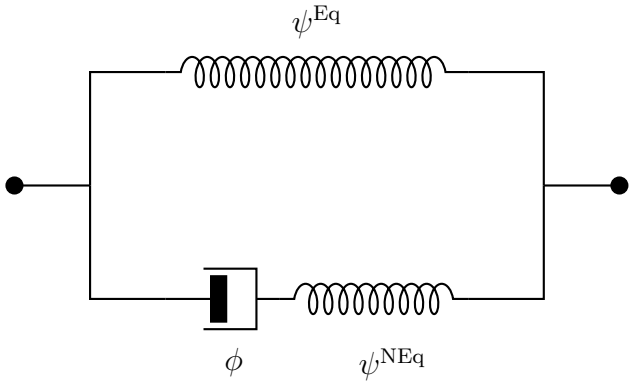

Figure 4.1: Rheological representation of the two-potential viscoelastic model. The top branch represents the equilibrium hyperelastic response (ψ^{Eq}), while the bottom branch combines the dissipative potential (ϕ) in series with the non-equilibrium energy storage (ψ^{NEq}).

The second potential is the dissipation potential ϕ, which governs the evolution of the internal variables (i.e., the viscous flow rule) and describes how the elastomer dissipates energy through viscous deformation. This potential is formulated to enforce the incompressibility of the viscous flow ($\det \mathbf{C}^v = 1$) and is expressed as:

$$\phi(\mathbf{F}, \mathbf{C}^v, \dot{\mathbf{C}}^v) = \begin{cases} \frac{1}{2}\dot{\mathbf{C}}^v \cdot \mathcal{A}(\mathbf{F}, \mathbf{C}^v)\dot{\mathbf{C}}^v & \text{if } \det \mathbf{C}^v = 1 \\ +\infty & \text{else} \end{cases} \tag{4.4}$$

with the viscosity tensor defined as:

$$\mathcal{A}_{ijkl}(\mathbf{F}, \mathbf{C}^v) = \frac{\eta(I_1^e, I_2^e, I_1^v)}{2} C_{ik}^{v\,-1} C_{jl}^{v\,-1} \tag{4.5}$$

where $I_2^e = \frac{1}{2}\left((I_1^e)^2 - \operatorname{tr}\left((\mathbf{C}\mathbf{C}^{v^{-1}})^2\right)\right)$ and $I_1^v = \operatorname{tr}(\mathbf{C}^v)$ and η represent the second invariant of the elastic deformation, the first invariant of the viscous deformation, and the viscosity parameter, respectively. This specific form of ϕ ensures that the energy dissipation is non-negative and is driven by the viscous parameters of the material.
Consequently, it follows that the first Piola-Kirchhoff stress tensor P is given by the relation [125, 130]:

$$\mathbf{P}(\mathbf{X}, t) = \frac{\partial \psi}{\partial \mathbf{F}}(\mathbf{F}, \mathbf{C}^v), \tag{4.6}$$

where $\mathbf{C}^v$ is implicitly defined by the evolution equation

$$\begin{cases} \dfrac{\partial \psi}{\partial \mathbf{C}^v}(\mathbf{F}, \mathbf{C}^v) + \dfrac{\partial \phi}{\partial \dot{\mathbf{C}}^v}(\mathbf{F}, \mathbf{C}^v, \dot{\mathbf{C}}^v) = \mathbf{0} \\ \mathbf{C}^v(\mathbf{X}, 0) = \mathbf{I} \end{cases} \tag{4.7}$$

Using the formalism expressed in 4.3 and 4.4, and using the seguent notation:

$$\begin{cases} \psi_{I_1}^{\mathrm{Eq}} = \dfrac{\partial \psi^{\mathrm{Eq}}(I_1, J)}{\partial I_1} \\ \psi_{J}^{\mathrm{Eq}} = \dfrac{\partial \psi^{\mathrm{Eq}}(I_1, J)}{\partial J} \\ \psi_{I_1^e}^{\mathrm{NEq}} = \dfrac{\partial \psi^{\mathrm{NEq}}(I_1^e, J)}{\partial I_1^e} \\ \psi_{J}^{\mathrm{NEq}} = \dfrac{\partial \psi^{\mathrm{NEq}}(I_1^e, J)}{\partial J} \end{cases} \tag{4.8}$$

we can express the First Piola expression more explicitly as:

$$\mathbf{P}(\mathbf{X}, t) = 2\psi_{I_1}^{\mathrm{Eq}}\mathbf{F} + 2\psi_{I_1^e}^{\mathrm{NEq}}\mathbf{F}\mathbf{C}^{v-1} + \left(\psi_J^{\mathrm{Eq}} + \psi_J^{\mathrm{NEq}}\right) J\mathbf{F}^{-T} \tag{4.9}$$

in which $\mathbf{C}^v$ is solution of this form of the evolution equation:

$$\begin{cases} \dot{\mathbf{C}}^v(\mathbf{X},t) = \dfrac{2\psi^{\mathrm{NEq}}_{I_1^e}}{\eta(I_1^e, I_2^e, I_1^v)} \left(\mathbf{C} - \dfrac{1}{3}(\mathbf{C}\cdot\mathbf{C}^{v-1})\mathbf{C}^v \right) \\ \mathbf{C}^v(\mathbf{X},0) = \mathbf{I} \end{cases} \tag{4.10}$$

It is worth remarking that the constitutive framework defined above is admittedly general and encompasses several classical behaviors as limiting cases [125]. Specifically, by setting the viscosity function to limiting values ($\eta \to 0$ or $\eta \to \infty$), the model recovers the behavior of a *non-Gaussian elastic solid*, which includes isotropic linear elasticity as a special case. Conversely, setting the equilibrium energy ψ^{Eq} to zero and the non-equilibrium energy ψ^{NEq} to infinity (rigid limit) yields the response of an incompressible *non-Newtonian fluid*. This further simplifies to a classical *Newtonian fluid* if the viscosity η is assumed constant. Consequently, the present model can be viewed as a unified framework capable of transitioning between solid-like and fluid-like responses depending on the material parameters.

4.3.2 General Constitutive Realization

The general framework presented above allows for arbitrary forms of the potential functions. Following Lopez-Pamies, a robust realization capable of describing non-Gaussian elasticity and shear-thinning viscosity is obtained by defining the potentials as sums of power-law terms:

$$\begin{cases} \psi^{\mathrm{Eq}}(I_1, J) = \displaystyle\sum_{r=1}^{2} \frac{3^{1-\alpha_r}}{2\alpha_r}\mu_r \left(I_1^{\alpha_r} - 3^{\alpha_r}\right) - \sum_{r=1}^{2} \mu_r \ln J + \frac{\kappa}{2}(J-1)^2 \\ \psi^{\mathrm{NEq}}(I_1^e, J) = \displaystyle\sum_{r=1}^{2} \frac{3^{1-\beta_r}}{2\beta_r}\nu_r \left(I_1^{e\beta_r} - 3^{\beta_r}\right) - \sum_{r=1}^{2} \nu_r \ln J \\ \eta(I_1^e, I_2^e, I_1^v) = \tilde{\eta}(I_1^v, \mathcal{J}_2^{\mathrm{NEq}}) = \eta_\infty + \dfrac{\eta_0 - \eta_\infty + K_1\left(I_1^{v\gamma_1} - 3^{\gamma_1}\right)}{1 + \left(K_2 \mathcal{J}_2^{\mathrm{NEq}}\right)^{\gamma_2}} \end{cases} \tag{4.11}$$

where the invariant governing shear-thinning is

$$\mathcal{J}_2^{\mathrm{NEq}} = \left(\frac{I_1^{e2}}{3} - I_2^e \right) \left(\sum_{r=1}^{2} 3^{1-\beta_r} \nu_r I_1^{e\beta_r - 1} \right)^2 . \tag{4.12}$$

This results in the final constitutive relation:

$$\begin{aligned}\mathbf{P}(\mathbf{X},t) = &\sum_{r=1}^{2} 3^{1-\alpha_r}\mu_r I_1^{\alpha_r-1}\mathbf{F} + \sum_{r=1}^{2} 3^{1-\beta_r}\nu_r I_1^{e\beta_r-1}\mathbf{F}\mathbf{C}^{v-1} \\ &- \left(\sum_{r=1}^{2}\frac{\mu_r+\nu_r}{J} - \kappa(J-1)\right) J\mathbf{F}^{-T}\end{aligned} \tag{4.13}$$

with the evolution equation for $\mathbf{C}^v$:

$$\begin{cases}\dot{\mathbf{C}}^v(\mathbf{X},t) = \dfrac{\sum_{r=1}^{2} 3^{1-\beta_r}\nu_r I_1^{e\beta_r-1}}{\tilde{\eta}(I_1^v, \mathcal{J}_2^{\mathrm{NEq}})}\left(\mathbf{C} - \dfrac{1}{3}(\mathbf{C}\cdot\mathbf{C}^{v-1})\mathbf{C}^v\right) \\ \mathbf{C}^v(\mathbf{X},0) = \mathbf{I}\end{cases} \tag{4.14}$$

In total, the constitutive prescription (4.14) and (4.13) encompasses fifteen material constants. Five of them, $\mu_1, \mu_2, \kappa, \alpha_1, \alpha_2$, serve to characterize the initial and the large-deformation non-Gaussian elasticity of the polymer at states of thermodynamic equilibrium. Another four, $\nu_1, \nu_2, \beta_1, \beta_2$, characterize the initial and the large-deformation non-Gaussian elasticity of our LDPE at non-equilibrium states. Finally, the remaining six constants $(\eta_0, \eta_\infty, K_1, \gamma_1, K_2, \gamma_2)$ generally serve to characterize the nonlinear deformation-dependent shear-thinning viscosity often observed in polymers [101, 132]. Although the mathematical framework described so far introduces these fifteen parameters as phenomenological coefficients, the adopted formulation is intrinsically linked to the polymer's microstructure. The decomposition of the model into parallel networks (equilibrium and non-equilibrium networks) is not a mere curve-fitting expedient, but directly reflects the heterogeneity of the macromolecular chain dynamics. Specifically, the equilibrium parameters $(\mu_1, \mu_2, \kappa, \alpha_1, \alpha_2)$ describe the response of the primary polymer network, consisting of strong entanglements or crystalline regions in the case of LDPE, whose density and stiffness dictate the long-term hyperelastic behavior. As demonstrated by Lopez-Pamies [127], this invariant-based formulation is fundamentally rooted in non-Gaussian statistical mechanics and can be directly correlated to the well-known Arruda-Boyce 8-chain model [133]. Rather than being simple mathematical weights, these parameters possess a distinct physical significance derived from the Langevin statistics of the underlying polymer chains. The exponents α_i capture the macroscopic strain-stiffening effect caused by the macromolecular chains reaching their finite extensibility limit. Concurrently, the moduli μ_i are intrinsically linked to the cross-link density and the thermal energy of the network. Thus, the macroscopic material constants inherently reflect the underlying microstructural and thermodynamic state of the polymer. Following the exact same conceptual framework, the non-equilibrium constants $(\nu_1, \nu_2, \beta_1, \beta_2)$ govern the transient response of the secondary network. It is crucial to note that these parameters share the same

physical meaning as their equilibrium counterparts, with ν_i representing the shear moduli and β_i capturing the finite extensibility, but they specifically characterize the secondary chains that are free to reorganize under stress. Rather than directly governing viscous dissipation, they define the non-linear stiffness of the viscoelastic branch. Finally, the set of viscous parameters $(\eta_0, \eta_\infty, K_i, \gamma_i)$ models the dissipation mechanisms driven by intermolecular friction: the dependence of viscosity on the strain rate (shear-thinning) finds physical justification in the progressive alignment and disentanglement of polymer chains along the loading direction, as described by the reptation theory. For clarity, the physical significance and macroscopic role of all the introduced constitutive parameters are summarized in Table 4.1.

Parameter	Macroscopic Role	Physical / Microstructural Meaning
	Equilibrium Network (Non-Gaussian Hyperelasticity)	
μ_1, μ_2	Small-strain shear moduli	Stiffness of the primary network; proportional to cross-link/entanglement density and thermal energy.
κ	Bulk modulus	Resistance to volume change (captures the near-incompressibility of the polymer).
α_1, α_2	Non-Gaussian parameters	Capture strain-stiffening; inversely proportional to the number of rigid links per chain, reflecting finite extensibility.
	Non-Equilibrium Network (Viscoelasticity)	
ν_1, ν_2	Viscous shear moduli	Stiffness of the transient secondary network; define the magnitude of stress relaxation.
β_1, β_2	Viscous non-Gaussian parameters	Chain stiffening within the non-equilibrium branch at large deformations.
	Viscous Dissipation (Shear-Thinning)	
η_0	Zero-shear viscosity	Initial viscous resistance associated with polymer chains in their highly entangled, resting state.
η_∞	Infinite-shear viscosity	Residual resistance when chains are fully aligned in the direction of flow.
K_1, K_2	Consistency multipliers	Control the transition between the Newtonian plateau and the shear-thinning region.
γ_1, γ_2	Shear-thinning exponents	Govern the rate of viscosity drop; linked to the kinetics of chain disentanglement and molecular slip.

Table 4.1: Summary of the constitutive model parameters and their micro-mechanical and macroscopic significance.

To accurately capture the complex response of the LDPE material within the numerical simulations presented in this study, the two-term ($r = 1, 2$) power-law structure is specifically retained. This multi-term expansion is strictly necessary: the first power-law term governs the small-to-moderate strain regime and the characteristic 'knee' transition, while the second term accounts for the pronounced strain-stiffening effect at larger stretches. Furthermore, to ensure numerical stability during computational implementation and parameter identification, if any network exponent approaches zero ($\alpha_r \to 0$ or $\beta_r \to 0$), the corresponding power-law term smoothly transitions to its exact neo-Hookean logarithmic limit via L'Hôpital's rule (e.g., yielding $\frac{3\mu_r}{2} \ln\left(\frac{I_1}{3}\right)$ for the equilibrium part, since $\lim_{\alpha\to 0}(x^\alpha - 1)/\alpha = \ln x$).

While Table 4.1 outlines the full set of parameters for the generalized constitutive theory, a practical simplification was required for the present analysis. Although it is well-established that LDPE exhibits non-Newtonian, shear-thinning behavior over a wide range of deformation rates, the experimental characterization in this study was restricted to a single strain rate. Consequently, the rate-dependence of the viscosity could not be uniquely identified. To ensure the robustness of the calibration and avoid overfitting, the viscosity function was simplified to a constant value ($\eta = \eta_0$), effectively treating the viscous dissipation as Newtonian within the investigated regime and setting the shear-thinning coefficients (K_1, K_2, etc.) to zero. While this represents a simplification of the general constitutive theory, it provides an accurate phenomenological description of the material response for the specific strain rate employed. Consistent with this reduction, the viscous evolution is governed by this simplified flow rule:

$$\begin{cases} \dot{\mathbf{C}}^v(\mathbf{X}, t) = \dfrac{\sum_{r=1}^{2} 3^{1-\beta_r} \nu_r I_1^{e\beta_r - 1}}{\eta_0} \left(\mathbf{C} - \dfrac{1}{3}(\mathbf{C} \cdot \mathbf{C}^{v-1})\mathbf{C}^v \right) \\ \mathbf{C}^v(\mathbf{X},0) = \mathbf{I} \end{cases} \tag{4.15}$$

It is worth noting that while non-Gaussian elasticity theories are traditionally derived for rubber-like materials (where hardening is purely entropic), they are employed here to capture the marked strain-hardening observed in LDPE at large deformations. Although in semi-crystalline polymers this phenomenon is physically driven by the irreversible orientation and unfolding of crystalline lamellae rather than reversible chain stretching, the mathematical structure of the non-Gaussian model proves to be an excellent phenomenological tool to describe the macroscopic stress upswing.

4.4 Calibration Strategy and Numerical Optimization

The predictive capability of the constitutive model relies on the accurate identification of the material parameters defined in the previous section. However, not all parameters were treated as free variables in the optimization process. To ensure physical consistency and reduce the complexity of the inverse problem, the stiffness-related parameters μ_1, ν_1, and κ were determined a priori. Specifically, the bulk modulus κ was fixed to a value consistent with standard literature data for semi-crystalline LDPE of this grade. Regarding the shear stiffness parameters μ_1 and ν_1, their values were derived from the reference work by Najmeddine et al. [63]. In the strictly theoretical Lopez-Pamies framework, the initial infinitesimal shear modulus is dictated by the sum of all shear moduli across the expansion series. However, to decouple the parameter identification process and reduce the complexity of the inverse problem, a physically motivated simplifying assumption was introduced in this work. It was assumed that the first terms of the series (μ_1 and ν_1) entirely dominate the initial small-strain linear response. Conversely, the second terms (μ_2 and ν_2) were treated as purely non-linear macroscopic contributors, physically associated with the limiting chain extensibility, and thus assumed to activate predominantly at larger stretches to capture the strain-stiffening effect. Under this assumption, the contribution of μ_2 and ν_2 to the initial infinitesimal stiffness is considered negligible ($G_0 \approx \mu_1 + \nu_1$) [127, 134]. Consequently, utilizing the Young's modulus (E) and Poisson's ratio (ν) reported by Najmeddine et al. [60], the parameter ν_1 was calculated analytically as:

$$G_0 = \frac{E}{2(1+\nu)} \approx \mu_1 + \nu_1 \quad \longrightarrow \quad \nu_1 = \frac{E}{2(1+\nu)} - \mu_1 \tag{4.16}$$

This approach ensures consistency with the macroscopic linear elastic properties found in the literature while preserving the necessary degrees of freedom to fit the highly non-linear, large-deformation regime.
Since the remaining non-linear parameters cannot be measured directly, an inverse analysis approach is adopted, fitting the model response to the experimental stress-strain data obtained from the uniaxial tensile tests on the unaged LDPE samples.

4.4.1 Optimization Framework

To automate the calibration process, a dedicated numerical optimizer was developed. The problem is formulated as the minimization of a scalar objective function $\mathcal{C}(\mathbf{p})$, defined as the discrepancy between the experimental engineering stress (P_{exp}), also extracted from the work of Najmeddine et al. [63], and the numerical counterpart (P_{num}) predicted by the model derived in the previous section:

$$\mathcal{C}(\mathbf{p}) = \sum_{i=1}^{N} \left(P_{\text{exp}}(\lambda_i) - P_{\text{num}}(\lambda_i, \mathbf{p}_0)\right)^2 \tag{4.17}$$

where N is the number of experimental data points and $\mathbf{p}_0$ is the vector of unknown material parameters. To ensure the physical and mathematical consistency of the constitutive model, the optimization process is subjected to strict inequality constraints. Following the foundational theoretical restrictions of the adopted hyperelastic framework [127, 130], sufficient conditions for strict polyconvexity and strong ellipticity (which guarantee macroscopic material stability), dictate that all shear moduli must be strictly positive ($\mu_r > 0$, $\nu_r > 0$) and the non-Gaussian network exponents must be greater than one-half ($\alpha_r > 1/2$, $\beta_r > 1/2$). Furthermore, to ensure thermodynamic consistency and a non-negative rate of mechanical dissipation, the viscosity parameter is constrained to be strictly positive ($\eta > 0$).

4.4.2 Calibration results

Consistent with the objective of developing a robust physics-based model and minimizing the number of empirical parameters lacking clear physical interpretation, the full calibration via the optimization algorithm is performed exclusively for the *unaged condition*. This preliminary step is fundamental to identify the baseline material parameters vector $\mathbf{p}_0$, which serves as the physical reference state for the material prior to any degradation. A representative example of the fitting quality achievable with this numerical tool is illustrated in Figure 4.2. Here, the macroscopic response is plotted in terms of nominal stress versus applied stretch (λ), which is kinematically linked to the strain invariants used in the constitutive formulation. Finally, Table 4.2 reports the corresponding optimized parameter vector $\mathbf{p}_0$.

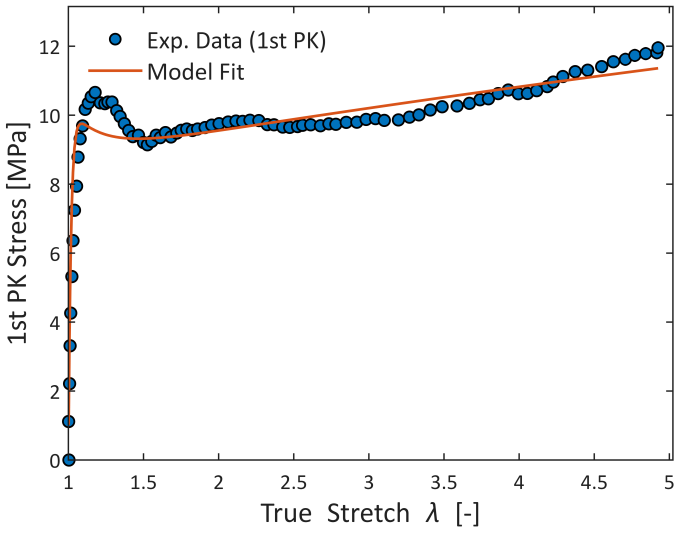

Figure 4.2: Representative result of the calibration procedure: comparison between the experimental stress-strain curve (dots) and the optimized model prediction (solid line) for the unaged material.

Parameters	**Reference Eq.**	**Value**
Equilibrium Branch		
Shear modulus, μ_1 [MPa]	[63]	2.3
Shear modulus, μ_2 [MPa]	(4.17)	2.5604
Stiffening exponent, α_1 [-]	(4.17)	0.51
Stiffening exponent, α_2 [-]	(4.17)	0.72073
Bulk modulus, κ [MPa]	[135, 136]	1700
Non-Equilibrium Branch		
Shear modulus, ν_1 [MPa]	(4.16)	196
Shear modulus, ν_2 [MPa]	(4.17)	1
Stiffening exponent, β_1 [-]	(4.17)	0.51
Stiffening exponent, β_2 [-]	(4.17)	0.51
Viscous Flow		
Viscosity, η_0 [MPa·s]	(4.17)	600.2

Table 4.2: Identified material parameters for the unaged LDPE specimen. The calibration is performed using the constitutive formulation defined in Eq. (4.13) and (4.15).

4.5 Constitutive Parameter Evolution and Aging Laws

To capture the mechanical degradation induced by photo-oxidation without performing independent phenomenological fits for each aging state, the evolution of the unaged material parameters is formulated as a direct function of the internal microstructural changes, specifically, variations in crystallinity and mass loss, which are physically driven by the UV exposure. This approach ensures that the modifications in the constitutive response are physically consistent and directly linked to the aging mechanisms, avoiding the redundancy of purely numerical fitting for every experimental curve.

4.5.1 Dependency on Crystallinity and Effective Stress

As discussed in section 2.3, the exposure to UV leads to a chemo-crystallization process, resulting in an increase of the crystalline fraction χ_c. Since the crystalline lamellae act as stiff reinforcing fillers within the amorphous matrix, the material stiffness is expected to increase. In the numerical implementation, this is modeled by scaling the entire set of viscoelastic parameters. Unlike a simple linear rule of mixtures, we adopt a power-law scaling to capture the non-linear reinforcement effect of the crystalline phase. Furthermore, to account for the reduction in cross-sectional area due to mass loss while working with continuum quantities, we use the mass ratio $\omega(t) = m(t)/m_0$ as a scaling factor for the effective stress.

The evolution laws for the equilibrium and non-equilibrium moduli are thus formulated as:

$$\begin{cases} \mathcal{P}^{\mathrm{Eq}}(t) = \mathcal{P}_0^{\mathrm{Eq}} \cdot \left(\frac{\chi_c(t)}{\chi_c(0)}\right)^{p_{\mathrm{crys}}^{\mathrm{Eq}}} \cdot \frac{1}{\omega(t)} \\ \mathcal{P}^{\mathrm{NEq}}(t) = \mathcal{P}_0^{\mathrm{NEq}} \cdot \left(\frac{\chi_c(t)}{\chi_c(0)}\right)^{p_{\mathrm{crys}}^{\mathrm{NEq}}} \cdot \frac{1}{\omega(t)} \end{cases} \tag{4.18}$$

where $\mathcal{P}$ represents any shear modulus or stiffness parameter of the equilibrium or non-equilibrium branch (μ_1, α_1, ν_1, etc.), $\chi_c(0)$ is the initial crystallinity, and the exponents p_{crys} are calibrated to match the stiffening trend observed in the experimental stress-strain curves.

4.5.2 Viscosity Evolution

In semicrystalline polymers, the crystalline phase acts mechanically as a set of rigid inclusions dispersed within a viscous and deformable amorphous matrix. During degradation, chain scission leads to an overall mass loss, while the apparent crystallinity increases. Consequently, the spatial confinement experienced by the

amorphous phase depends not only on the absolute crystalline fraction $\chi_c(t)$, but on the effective crystalline fraction (ϕ_{eff}), defined as the ratio between the volume of the crystals and the residual mass fraction of the polymer network, $\omega(t)$:

$$\phi_{eff}(t) = \frac{\chi_c(t)}{\omega(t)} \tag{4.19}$$

The increase in this effective fraction drastically reduces the mobility of the amorphous chains. To model the resulting divergence of the macroscopic viscosity $\eta(t)$, we move from the fundamental rheological framework of the Krieger-Dougherty equation [137], which quantifies the stiffening caused by solid inclusions. However, unlike disordered suspensions of spheres that undergo steric jamming at a geometric fraction of 64% (random close packing), the crystalline lamellae of polymers are intrinsically ordered structures capable of structural interconnection. Theoretically, they can pack to occupy the entire volume of the material ($\phi_{max} \to 1$) [138].

Consequently, the mobility of the entangled amorphous chains is not limited by a jamming of spherical particles, but scales directly with the physically available inter-lamellar amorphous space, namely $(1-\phi_{eff}(t))$. To accurately capture this behavior and normalize it against the unaged reference state, an exact micromechanical formulation derived from Mooney's equation for concentrated suspensions [139] was adopted. By setting the theoretical maximum packing limit to $\phi_{max} = 1$, the following constitutive equation is obtained:

$$\eta(t) = \eta_0 \cdot \left(\frac{1 - \phi_{eff}(0)}{1 - \phi_{eff}(t)} \right)^{2.5} \tag{4.20}$$

The rigorous nature of this formulation lies in the complete absence of parameters calibrated on experimental macroscopic data. The exponent 2.5 in Equation (4.20) is not numerically fitted; rather, it represents the universal theoretical constant (intrinsic viscosity $[\eta]$) originally derived by Einstein [140] to describe the increase in viscous dissipation induced by solid inclusions in a continuous medium. The application of this equation analytically demonstrates that the experimentally measured macroscopic stiffening is the exact thermodynamic consequence of the contraction of the amorphous free volume. Thus, the decay of the mechanical properties is predicted exclusively through the micromechanical evolution of the polymer, completely eliminating the need for empirical thresholds.

It is worth noting that the material degradation framework is formulated to scale only the stiffness-related moduli (μ_r, ν_r, K) and the macroscopic viscosity (η), while the non-Gaussian network exponents (α_r, β_r) are kept constant at their unaged values. This physically motivated assumption implies that the photo-oxidative aging primarily increases the effective crosslink density and restricts bulk mobility, thus stiffening the material, without fundamentally altering the intrinsic limiting

extensibility of the polymer chains. Furthermore, maintaining constant exponents ensures robust numerical stability across all aging steps, avoiding non-physical exponential stress amplifications.

4.5.3 Evolution of G_c: The Ductile-to-Brittle Transition

In semi-crystalline polymers such as LDPE, the macroscopic fracture toughness is fundamentally dictated by the interplay between the crystalline domains and the highly deformable amorphous phase. To physically justify the ductile-to-brittle transition observed during photo-oxidative degradation, it is essential to decouple the critical strain energy release rate, G_c, into its fundamental micro-mechanical components:

$$G_c = \Gamma_0 + \Gamma_{diss} \tag{4.21}$$

Here, Γ_0 represents the intrinsic fracture energy, the theoretical thermodynamic work required solely for the scission of the polymer main-chain bonds (C-C) to create two new fracture surfaces, without any background plasticity [141]. Conversely, Γ_{diss} represents the energy dissipated through localized plastic yielding, chain disentanglement, and viscous flow occurring primarily within the amorphous regions ahead of the crack tip. For the pristine, unaged material, the amorphous domains are highly mobile, allowing the plastic dissipation term to overwhelmingly dominate the total fracture work ($\Gamma_{diss} \gg \Gamma_0$). Therefore, the baseline fracture energy ($G_{c,0} = 1.7$ kJ/m^2), consistent with the local effective separation energy identified by Kroon et al. [142] via cohesive zone modeling, is heavily governed by this plastic contribution occurring within the amorphous regions ahead of the crack tip. However, photo-oxidative degradation drastically alters this microstructural balance. As UV exposure progresses, the combination of chain scission and cross-linking reactions leads to a macroscopic increase in the degree of crystallinity. Physically, this corresponds to a volumetric reduction and severe embrittlement of the amorphous phase. Because the amorphous network is the primary vehicle for plastic yielding, its continuous depletion implies that the plastic dissipation contribution to the overall fracture work progressively tends to zero ($\Gamma_{diss} \to 0$). Ultimately, when the material reaches a critical structural embrittlement, macroscopic plasticity is entirely suppressed, forcing the overall fracture toughness to collapse toward its fundamental atomic lower bound ($G_c \approx \Gamma_0$). To physically capture this degradation cascade, the evolution of the critical fracture energy G_c is formulated not as a continuous phenomenological fit, but as a multi-stage micro-mechanical process governed by a structural crystallinity threshold. To physically capture this degradation cascade, the evolution of the critical fracture energy G_c must account for the gradual exhaustion of the amorphous network. Rather than a harsh numerical step, the ductile-to-brittle transition is physically modeled as a continuous, statistically distributed microstructural process. To this end, a logistic

sigmoid function was formulated. This approach perfectly captures the non-linear collapse of the macroscopic toughness driven by the evolving crystallinity $\chi_c(t)$, smoothly transitioning toward the fundamental atomic lower bound:

$$G_c(\chi_c(t)) = K_{brittle} + \frac{G_{c,0} - K_{brittle}}{1 + \exp\left(\alpha \cdot (\chi_c(t) - \chi_{c,trans})\right)} \cdot \omega \tag{4.22}$$

where:

- $G_{c,0}$ is the pristine baseline fracture energy;
- $K_{brittle}$ represents the residual macroscopic toughness of the fully embrittled material, acting mathematically as the lower asymptote of the sigmoidal collapse. Crucially, rather than being an arbitrary fitting parameter, it is established *a priori* within a predictive framework to match the theoretical thermodynamic limit Γ_0. Following Lake and Thomas [141], the minimal energy strictly required for the homolytic scission of the macromolecular main-chain bonds (C-C), without any background plasticity, lies in the range of $\Gamma_0 \approx 40 - 100$ J/m^2. To physically enforce this intrinsic boundary, the residual threshold is defined as a specific percentage of the initial pristine toughness ($G_{c,0} = 1700$ J/m^2). By setting $K_{brittle}$ to 2.5% of the initial energy, the model bounds the fully degraded state to $G_{c,residual} \approx 0.025 \cdot 1700$ J/m^2 $= 42.5$ J/m^2. This rigorously guarantees that the macroscopic fracture energy collapses precisely toward the theoretical pure bond-scission limit, preventing it from unphysically dropping to zero;
- $\chi_c(t)$ is the current crystallinity percentage driving the embrittlement;
- $\chi_{c,trans}$ represents the critical microstructural threshold (the inflection point of the transition);
- α is a shape parameter dictating the abruptness of the physical embrittlement cascade.
- ω denotes the minute mass ratio, as previously defined in the text;

As demonstrated by the experimental data (Figure 4.3), this sigmoidal framework provides an excellent phenomenological description of the degradation process. It enforces the strict thermodynamic restriction of Γ_0 at high degradation states, while accurately predicting the rapid collapse of plastic dissipation once the crystallinity approaches the critical threshold $\chi_{c,trans}$.

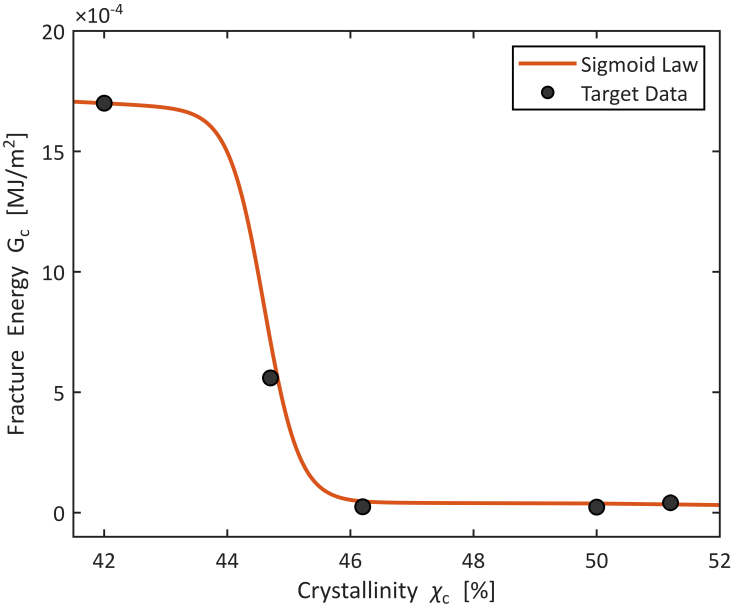

Figure 4.3: Evolution of the critical fracture energy G_c as a function of the evolving crystallinity χ_c. The experimental data (black markers) are accurately captured by the proposed logistic sigmoid model (red solid line), highlighting the smooth ductile-to-brittle transition towards the intrinsic atomic lower bound Γ_0.

4.5.4 Phase-Field Regularization and Length Scale Identification

Unlike the viscoelastic parameters identified above, which describe the physical constitutive response, the phase-field length scale l_c serves primarily as a geometric regularization parameter. As discussed in Section 4.2, l_c dictates the width of the diffuse crack band and ensures the mesh objectivity of the numerical solution, while concurrently influencing the critical stress required for crack nucleation. Before proceeding with the full simulations, a parametric sensitivity analysis was conducted to select an appropriate value for l_c. For the LDPE unaged investigated in this study, the critical energy release rate was fixed to a literature value of $G_{c,0} = 1{,}7\,\mathrm{kJ/m^2}$, as mentioned before. The study involved a series of uniaxial tension simulations on a monotonic unit element, varying l_c within the range of 0.5 to 0.006 mm to evaluate its effect on the macroscopic constitutive response. The results of this sensitivity analysis, illustrated in Figure 4.4, reveal a direct correlation between the length scale parameter and the predictive accuracy of the model. Two competing trends were clearly identified:

- *High predictive error for large l_c*: As l_c increases, the specific fracture energy

that the material can dissipate per unit volume (which analytically scales with G_c/l_c) is artificially reduced. Consequently, the constitutive element reaches the critical damage threshold prematurely at lower strain energy levels. This distorts the global energy balance, leading to a severe underestimation of the macroscopic ductility and predicting an unphysically early onset of fracture.

- *High accuracy for small l_c*: Conversely, as l_c decreases, the volumetric dissipation capacity correctly increases, allowing the material point to sustain higher deformations before localizing damage. The model correctly converges toward the experimental failure strain, exhibiting high physical fidelity. However, it is worth anticipating that while this small length scale is easily handled in a 0D/1D constitutive framework, its implementation in structural Boundary Value Problems (FEM) would come at a drastic computational cost, requiring a prohibitively refined mesh to accurately resolve such a narrow damage band.

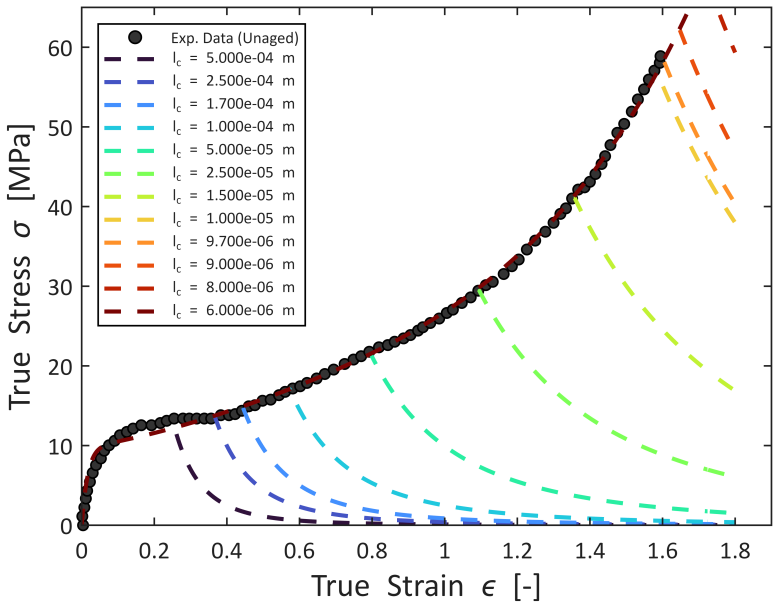

Figure 4.4: Parametric study of the phase-field length scale (l_c). The curves illustrate the sensitivity of the macroscopic constitutive response and the failure onset as the internal length scale parameter is varied.

Consequently, a value of $l_c = 0.0097$ mm was selected as the optimal compromise. This choice ensures a mesh-independent solution that correctly dissipates the fracture energy G_c without inducing spurious compliant artifacts. Crucially, this value is maintained constant for all subsequent aging analyses, as the geometric

regularization of the crack is assumed to be an intrinsic property of the modeling scale rather than a variable of the degradation process.

4.6 Summary of the Predictive Strategy

In summary, the proposed numerical framework constitutes a sequential multi-scale approach, bridging the gap between microstructural degradation and macroscopic mechanical performance. The computational workflow proceeds through four distinct logical steps:

1. *Reference State Calibration:* The baseline constitutive vector $\mathbf{p}_0$ is uniquely identified by minimizing the error between the model prediction and the experimental response of the *unaged* material. This defines the reference physical state of the polymer network prior to degradation.

2. *Microstructural Coupling:* For any specific aging duration, the scalar internal variables governing the structural evolution, the crystallinity ratio ($\chi_c(t)$) and the minute mass loss ratio ($\omega(t)$), are directly injected into the simulation framework from the experimental dataset.

3. *Constitutive Update:* The material parameters are evolved from their reference values $\mathbf{p}_0$ to their aged configuration $\mathbf{p}(t)$ via the physically-motivated scaling laws defined in Eq. (4.18), (4.20) and (4.22). This step maps the microstructural damage onto the continuum mechanical descriptors.

4. *Forward Prediction:* The stress-strain response for the degraded material is simulated numerically using the updated parameter set. Crucially, rather than performing independent phenomenological fits for each specific aged state, the curves are naturally generated through the unified calibration of the microstructural evolution laws.

This methodological approach ensures that the predicted mechanical embrittlement is not an artifact of numerical regression, but a direct deterministic consequence of the physical alterations in the polymer network (i.e., chemi-crystallization and volatile extraction).

4.7 Results and Model Validation

In accordance with the self-contained structure of this work, the results of the parameter identification procedure and the subsequent validation of the evolutionary model are presented in this section.

4.7.1 Fitting of the Unaged Material

The optimization algorithm described in Section 4.4.1 was first applied to the experimental stress-strain data of the unaged LDPE, minimizing the error in terms of engineering stress (First Piola-Kirchhoff) and engineering strain. However, to properly evaluate the goodness of the fit in the finite deformation regime, both the experimental dataset and the numerical predictions were subsequently converted into true stress (Cauchy) and true strain measures. The calibrated parameters, listed in Table 4.2, successfully capture the highly nonlinear response of the material, including the initial viscoelastic relaxation and the strain-stiffening at large deformations. Figure 4.5 compares the converted true mechanical responses, demonstrating the model's capability to accurately reproduce the behavior of the pristine polymer.

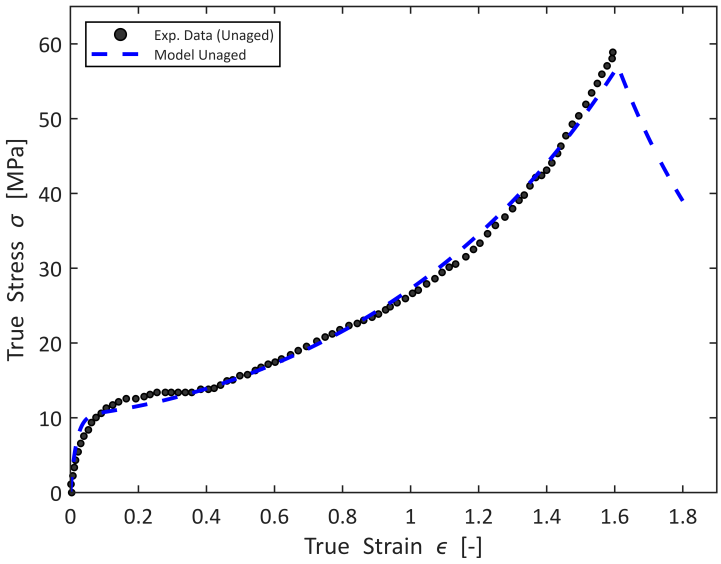

Figure 4.5: Calibration of the constitutive model for the unaged LDPE. The comparison between the experimental data (circles) and the numerical simulation (dashed line) is evaluated in terms of true stress and true strain, following an optimization process performed on the nominal (First Piola-Kirchhoff) parameters.

4.7.2 Prediction of Aged Response

Following the baseline calibration, the predictive capability of the evolutionary framework was assessed. By updating the failure/viscosity parameters based solely on the measured crystallinity fraction and mass loss, the model blindly predicted the stress-strain response of the aged samples.

Figure 4.6 illustrates the model predictions for the different aging times against the respective experimental curves. We can observe how the physically-based evolution laws correctly capture the two main macroscopic effects of photo-oxidation:

- *Stiffening:* The increase in the initial slope (Young's modulus), driven by the chemo-crystallization mechanism (Eq. 4.18).
- *Embrittlement:* The transition from ductile yielding to premature brittle fracture, modeled through the collapse of the fracture toughness G_c towards its atomic limit Γ_0. This decay reflects the suppression of plastic dissipation mechanisms caused by the increasing crystalline constraint.

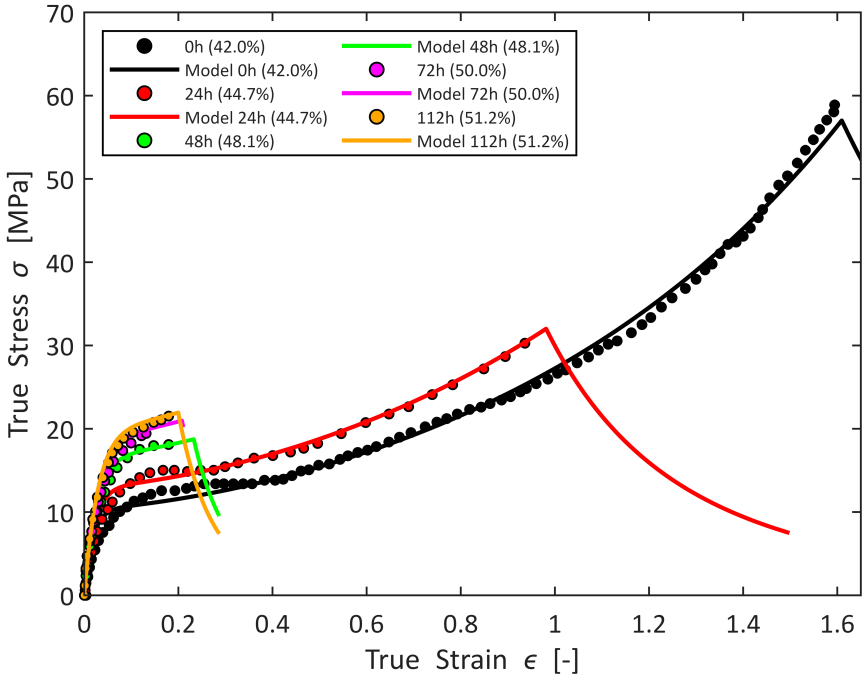

Figure 4.6: Model validation against aged specimens. The solid lines represent the model predictions obtained by evolving the constitutive parameters according to the measured microstructural changes (crystallinity and mass loss), without independent refitting.

Although the overall predictive agreement is highly satisfactory, minor localized deviations from the experimental datasets can be inevitably observed. These slight discrepancies are fundamentally tied to the inherent stochastic nature of the photo-oxidative degradation process. Specifically, aging-induced micro-defects, local microstructural heterogeneities, and the statistical variance of the molecular chain network introduce a natural experimental scatter that transcends the idealized macroscopic continuum formulation.

4.8 Concluding Remarks and Towards 2D/3D Implementation

In this chapter, the numerical framework required to simulate the mechanical response of the photo-oxidized LDPE has been established. Starting from the general thermodynamic principles, the constitutive equations have been specialized for the uniaxial case, allowing for the development of a computationally efficient 1D solver.

The results presented in the previous section highlight two major achievements:

- *Robust Calibration:* The optimization procedure successfully identified a set of material parameters that accurately reproduce the complex, highly non-linear viscoelastic behavior of the unaged polymer.
- *Physical Consistency:* The predictive strategy, based on evolving these parameters according to microstructural measurements (crystallinity and mass loss), demonstrated that the macroscopic embrittlement is not a random phenomenon but a deterministic consequence of the chemical degradation. This validates the physical basis of the proposed constitutive model.

While the current 1D implementation provides essential insights into the material's constitutive behavior, it is intrinsically limited to homogeneous deformation states. To investigate the fracture process in realistic components, where complex stress states and geometric singularities (such as crack tips) are present, a multi-dimensional analysis is required. Consequently, the natural progression of this work involves the implementation of the general 3D constitutive theory (presented in Section 4) into a commercial Finite Element solver. Specifically, the formulation is suitable for implementation as a User Element subroutine (UEL) or a User Material subroutine (UMAT) within the Abaqus/Standard environment. This extension, which relies on the same thermodynamic potentials validated here but utilizes the full 3D weak form, will allow for the simulation of crack propagation and damage evolution in 2D and 3D domains, setting the stage for the structural integrity assessment of complex aged components.

Part II

The Atomic Oxygen Challenge: Degradation Kinetics in Space Environment

Chapter 5

Theorethical Background on Space Environment

5.1 Space Environment Challenges

The space environment represents one of the most hostile operating scenarios for polymeric materials. Upon leaving the Earth's protective atmosphere, spacecraft surfaces are exposed to a complex combination of environmental stressors that act synergistically to degrade material properties [143, 144]. From a design perspective, the selection of materials for LEO and VLEO applications requires a rigorous assessment of the specific environmental constituents that define this regime. Unlike higher orbits, LEO is characterized by a unique interaction between the spacecraft and the residual atmosphere, creating a distinct hierarchy of degradation threats:

- *Atomic Oxygen:* Being the predominant species in LEO altitudes (approximately 200-700 km), AO acts as a powerful oxidizing agent and is considered as the most damaging species for externaly exposed polymeric materials. Upon impact, it promotes the erosion of organic materials, leading to continuous mass loss and surface recession.

- *UV and Ionizing Radiation:* The unshielded exposure to solar UV radiation and charged particles (electrons, protons) provides sufficient energy to break primary covalent bonds (such as C–C and C–H). This process triggers *photo-oxidation* and chain scission mechanisms, which ultimately degrade the mechanical and optical properties of the polymer.

- *High Vacuum and Thermal Cycling:* The absence of pressure induces the *outgassing* of volatile components, leading to potential contamination of nearby sensitive surfaces (e.g., sensors and solar arrays). Furthermore, the rapid

alternation between sunlight and shadow causes extreme thermal expansion and contraction, generating cyclic mechanical stresses that can induce microcracking and fatigue.

- *Plasma and Micrometeoroids:* The environment also includes space plasma, which can cause surface charging and arcing, as well as micrometeoroids and orbital debris, which pose a physical threat of hypervelocity impacts.

It is imperative to understand that in the actual flight environment, these factors do not act in isolation. Instead, they exhibit a strong synergistic effect [144, 145], where the combined degradation is significantly more severe than the sum of the individual contributions. The synergistic effect of these environmental loads is a governing factor in defining the structural integrity, dependability, and service life of materials deployed in space applications To fully comprehend these complex synergistic mechanisms, in-flight materials exposure experiments have been historically conducted on platforms like the Space Shuttle and the International Space Station (ISS) [146, 147]. However, due to the high cost and limited availability of such flight opportunities, as well as the necessity for accelerated testing to simulate years of operation, the scientific community relies heavily on ground simulation systems. While these facilities are essential to systematically isolate specific degradation factors and validate predictive models before orbital deployment, accurately recreating the synergistic effects of in-flight operational conditions is notoriously complex. Consequently, developing high-fidelity ground simulations that faithfully replicate the harsh space environment remains one of the most pressing challenges in the current aerospace engineering landscape.

5.2 The Dominance of Atomic Oxygen

While all the aforementioned factors contribute to aging, in the specific context of LEO missions targeted in this second part of the thesis, the degradation mechanism is definitively dominated by atomic oxygen. Unlike the diffusive bulk degradation typical of molecular oxygen or UV radiation (analyzed in Part I), AO attack is a surface-limited phenomenon characterized by a distinct dual nature:

- *Chemical Oxidation:* AO is a highly reactive radical that instantly oxidizes organic bonds upon contact.

- *Physical Erosion:* Due to the high orbital velocity (≈ 8 km/s), oxygen atoms impinge on the spacecraft surfaces with high translational energies of approximately $4.5 - 5$ eV. This is accompanied by massive fluxes on the order of 10^{13}–10^{15} $[\frac{atoms}{cm^2 \cdot s}]$, causing physical sputtering and mass removal [143].

This high kinetic energy is sufficient to overcome the activation barriers of most organic bonds, resulting in a rapid oxidative decomposition known as *"erosive oxidation"*. Fundamentally, this regime differs from the previously modeled terrestrial scenario. In terrestrial aging, mass loss occurs gradually through the egress of internal volatiles, leaving behind a structurally altered but physically present bulk material. In contrast, AO erosion involves the complete and immediate gasification of the exposed surface. The highly reactive atomic oxygen breaks the polymer chains upon impact, producing volatile byproducts (typically CO, CO_2, and H_2O) that instantly desorb, thereby driving a continuous macroscopic surface recession. To quantify this susceptibility, the primary metric used is the *Erosion Yield (E_y)*, defined as the volume of material removed per incident oxygen atom (cm^3/atom). For standard, unprotected aerospace polymers (e.g., Kapton®), experimental observations confirm that E_y acts essentially as an intrinsic material property. Consequently, under a constant orbital flux, these materials exhibit a *linear mass loss* behavior: as long as the material exists, the surface recedes at a steady [148, 149]. At the microscopic scale, however, this recession is rarely uniform. The directional nature of the impact (ram direction) typically leads to the development of a characteristic *"carpet-like" texture*, composed of microscopic cones or peaks aligned with the velocity vector [143, 149]. This roughening implies that the local erosion rate is influenced by surface heterogeneities, a phenomenon that can degrade optical properties (absorptance/emittance) even before structural failure occurs.

Given this aggressive environment, standard organic polymers require advanced protection strategies to survive long-term missions. This necessity drives the development of hybrid materials, such as POSS nanocomposites, capable of forming self-passivating silica layers that arrest the erosion process [150–152]. The following chapter will specifically model the erosion kinetics and its mitigation for this particular class of materials.

5.3 Reference Aerospace Polymers and Critical Vulnerabilities

To quantify the degradation phenomena modeled in this part of the thesis, it is essential to first identify the standard class of materials currently utilized in LEO/VLEO missions. As reviewed by Wright [77] and Grossman et al. [143], the aerospace sector relies heavily on a diverse range of polymer families, including epoxies, fluorocarbons, polyurethanes, and silicones, for functional applications ranging from adhesives and conformal and thermal control coatings to thermal blankets foams, elastomers, plastic components and fibers. Their use also extends to specialized functions, like anti- misting additives for fuel, and as the basis for

advanced nanocomposite materials. Consequently, these polymer materials are employed as lubricants, insulating paints, temperature control cladding, printed circuit boards, optical fiber materials for optoelectronic devices, and as the matrix for high-strength composite materials in spacecraft. However, the material selection process is governed by a critical trade-off between functional performance (specifically dielectric and thermal properties) and long-term environmental durability. To fully appreciate this trade-off, it is worth detailing the primary polymeric families that sustain the aerospace ecosystem, each selected for highly specific functional roles:

- *Epoxy Resins:* These represent the standard matrix for structural carbon-fiber reinforced polymers (CFRP). Their excellent adhesion, dimensional stability, and mechanical rigidity make them indispensable for primary load-bearing structures in both aircraft fuselages and satellite buses.

- *Fluoropolymers:* Often utilized in conjunction with Polyimides in Multi-Layer Insulation (MLI) blankets, Teflon-based coatings are highly valued for their chemical inertness, extremely low friction, and tailored thermo-optical properties (such as low solar absorptance and high thermal emittance) required for thermal radiators.

- *Polyolefins (e.g., LDPE):* Although characterized by a lower thermal resistance compared to high-performance engineering plastics, Polyethylene-based materials have gained significant traction for radiation shielding. Due to their high hydrogen density, they are exceptionally effective at mitigating Galactic Cosmic Rays (GCRs) and solar energetic particles [77–79], often outperforming traditional aluminum shielding in protecting onboard electronics and crew. As previously discussed in the context of Laurenzi et al. [80], the structural integrity of these polymers under harsh space conditions is paramount. Consequently, LDPE is frequently employed as a fundamental model material to isolate and understand the baseline degradation kinetics before scaling predictive models to more complex systems.

Within this extensive landscape, one specific material has established itself as the backbone of space insulation and thermal control: *Polyimide (PI)*, most notably represented by the commercial product *Kapton*®.

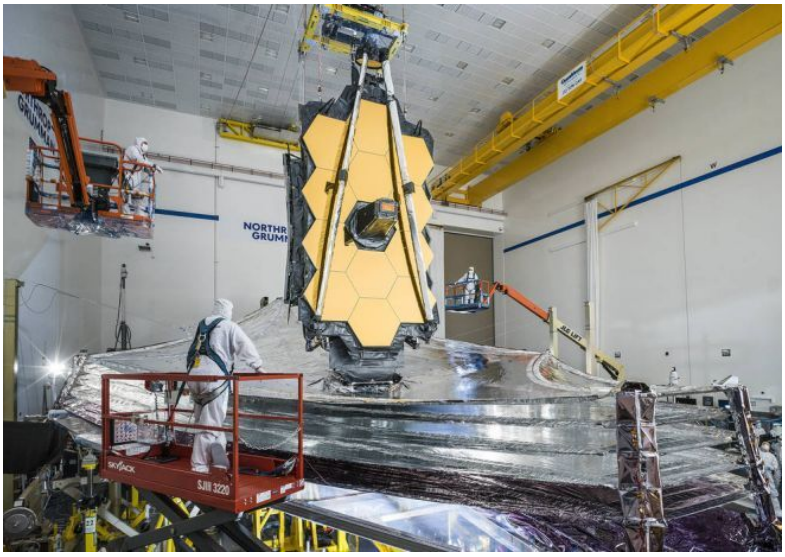

Figure 5.1: The sunshield of the James Webb Space Telescope (JWST), demonstrating a critical application of high-performance polymers in space structures. The membranes are composed of Kapton polyimide relied upon for its thermal stability but requiring specialized coatings for environmental protection.

Since its commercialization by DuPont in the late 1960s, Kapton has been selected as the primary dielectric insulation for wire and cabling in approximately 70 major commercial and military programs worldwide. Its dominance in the aerospace sector stems from an unrivaled combination of properties that address the specific challenges of the vacuum environment:

- *Extreme Thermal Stability:* Kapton creates a stable operating window unavailable to most other organic materials. It remains functional across a massive temperature range, from cryogenic conditions as low as $-269°C$ (4 K) up to $+400°C$. Crucially, unlike many thermoplastics, it has no melting point and does not burn, maintaining its physical integrity even during temporary thermal spikes.

- *Vacuum Compatibility:* In the hard vacuum of space, many materials release volatile compounds (outgassing) that can contaminate sensitive optics and sensors. Polyimides exhibit excellent low-outgassing characteristics, making them safe for sensitive payloads.

- *Radiation and Chemical Resistance:* The chemical structure of the imide ring provides inherent resistance to ionizing radiation and solvents, ensuring long-term durability in orbit.

The most iconic application of this material is visible on nearly every satellite: the gold-colored MLI blankets. These "thermal blankets" protect the spacecraft from the intense solar heat and the freezing cold of deep space. A prime example of this application is found in the JWST, shown in Figure 5.1. Its massive sunshield consists of five thin layers of Kapton (coated with aluminum and doped silicon) designed to separate the hot side (facing the Sun, $\approx 85°C$) from the cold side (facing deep space, $\approx -233°C$), effectively attenuating heat by over a million times. This historical success has cemented Polyimide as the reference material for LEO applications. However, despite its exceptional bulk characteristics, Kapton remains the universal benchmark for susceptibility to AO. Unprotected polyimide demonstrates a high and linear erosion yield ($E_y \approx 3.0 \times 10^{-24}$ cm^3/atom) in the LEO environment. While this predictable degradation provides an ideal baseline for assessing the efficacy of POSS-based protective strategies, its inherent vulnerability to AO attack represents a critical limitation. This severe degradation specifically motivates the development of the nanocomposites addressed in this work, making it essential to first establish the fundamental mechanisms of AO protection.

5.4 Principles of Protection against Atomic Oxygen

Given the severity of the erosion rates for pure organic polymers, long-duration LEO missions require robust protection strategies capable of arresting this mass loss. The primary engineering challenge lies in imparting environmental survivability to these materials without compromising the intrinsic lightweight, flexible, or dielectric properties that make polymers indispensable for spaceflight. Historically, protection strategies have been categorized into two main approaches: external surface coatings and bulk material modification.

5.4.1 Passive Surface Coatings

The traditional approach to prevent erosion involves shielding the polymer with a thin, chemically inert inorganic layer. Common coating materials include Silica (SiO_2), Alumina (Al_2O_3), or Indium Tin Oxide, often applied via sputtering or vapor [153]. While these coatings are effective as long as they remain pristine, they suffer from a critical vulnerability known as *undercutting*. Due to thermal cycling mismatch, debris impact, or manufacturing imperfections, these thin films inevitably develop pinholes or cracks. Atomic oxygen, behaving as a diffusive fluid, penetrates these defects and erodes the underlying soft polymer. This creates large subsurface cavities, phenomena extensively modeled via Monte Carlo simulations [154], that eventually lead to the structural collapse of the unsupported coating,

accelerating failure as observed in retrieved Hubble Space Telescope hardware [155, 156].

5.4.2 Bulk Modification: The Hybrid Approach

To overcome the fragility of surface coatings, the state-of-the-art has shifted towards *Organic-Inorganic Hybrid materials*, specifically polymer nanocomposites. In this "bulk protection" strategy, the protective element is not a superficial skin but is dispersed intrinsically throughout the material volume. This ensures that if the surface is damaged (e.g., by micrometeoroids), the material retains its self-healing capability [150, 157]. Among the various fillers investigated, *POSS (Polyhedral Oligomeric Silsesquioxane)* represents the most promising candidate due to its molecular-level dispersion and specific reactivity with atomic oxygen.

The Self-Passivation Mechanism

The protection mechanism of POSS-based nanocomposites relies on the concept of *differential reactivity* of the constituents exposed to the LEO environment:

- *Organic Matrix:* The carbon-based polymer backbone reacts with AO to form volatile species (CO, CO_2, H_2O) which instantly desorb and leave the surface.
- *Inorganic Cages (Silicon-based):* The silicon-oxygen core of the POSS cage reacts with AO to form non-volatile, solid oxides (SiO_2).

Percolation and Physical Barrier Formation

The interplay between these two reactions leads to a dynamic surface evolution. As the organic matrix is preferentially eroded ("scavenged"), the non-volatile inorganic particles are left behind. These residual silica structures accumulate on the receding front, progressively building an in-situ *Passivation Layer* (often referred to as the silica "ash" layer).

The fundamental physical hypothesis driving the modeling in the next chapter is that of geometric percolation. Initially, the erosion proceeds linearly. However, once the surface density of these accumulating particles reaches a critical threshold (percolation threshold), they coalesce to form a continuous, interlocking physical barrier. This barrier effectively shields the underlying bulk from further AO attack, transitioning the material system from an active linear erosion regime to a stable, passive state.

Chapter 6

A Computational Percolation Framework for Atomic Oxygen Erosion in POSS-Nanocomposites

This chapter presents the theoretical framework developed to describe the erosion kinetics of POSS-filled polymers in the LEO environment. Unlike empirical approaches that rely on simple, empirical curve-fitting of mass loss data, a physics-based model is proposed here. The formulation treats the problem as a *moving boundary problem*, where the growth of a protective silica layer competes with the diffusive ingress of atomic oxygen. The model is derived from first principles of mass transport and reaction kinetics, adapting the classical Stefan and Deal-Grove theories [158] to the specific chemistry of hybrid organic-inorganic composites.

6.1 Introduction and Objectives

As established in the previous chapter, the survivability of POSS-enhanced polymers in LEO is fundamentally driven by their ability to form a stable silica passivation layer. While section 5.4 described the phenomenology of this protective mechanism, illustrating how the in-situ formed SiO_2 acts as a robust diffusion barrier to shield the virgin material from atomic oxygen, translating this capability into a predictive engineering model remains a distinct challenge. The primary objective of this chapter is to formulate a mathematical framework capable of predicting the total mass loss and the recession depth of POSS-filled polymers as a function of the environmental fluence. By moving beyond empirical curve-fitting, we aim to link

the macroscopic erosion kinetics directly to the microstructural parameters defined in the previous analysis: specifically, the POSS-filler concentration, the volume fraction, and the erosion depth measured on the material.

6.2 Reference Experimental Framework

To derive a consistent analytical model, we must first define the geometric and chemical features of the dispersed phase. Unlike traditional macroscopic fillers, POSS molecules act as distinct nanoscopic entities that can be modeled as quasi-spherical particles [159, 160]. A schematic representation of the characteristic cage-like architecture of the POSS molecule, including its possible integration into the polymer matrix, either as a pendant side-group or directly incorporated into the main-chain, is illustrated in Figure 6.1.

For the purpose of the mathematical derivation presented in Section 6.4, the POSS molecule is characterized by the following intrinsic properties:

- *Geometry:* A cage-like nanostructure with a diameter typically in the range of 1.5–3.0 nm (including the organic corona) [161, 162].

- *Stoichiometry:* Defined by the general hybrid formula $(RSiO_{1.5})_n$. The inorganic core $(Si - O)$ represents the "ash precursors" that will survive the atomic oxygen attack, while the organic corona (R) determines the initial volume occupancy and compatibility with the matrix, whether the POSS cage is incorporated into the polymer main chain or attached as a pendant side group.

This precise geometric definition allows us to treat the erosion process not as a continuum chemical reaction, but as a discrete *geometric coverage problem*, where the survival of the material depends on the projected area of the exposed inorganic cages.

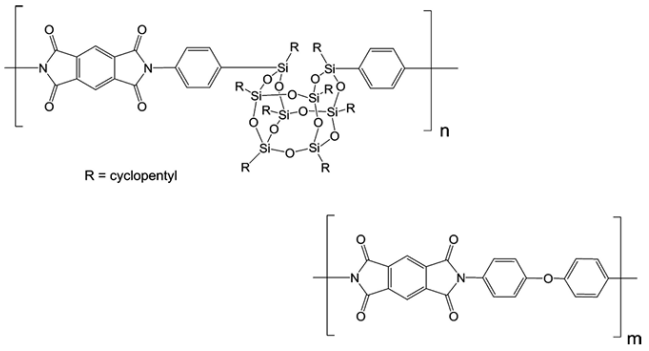

(a) Main-chain (MC) incorporation

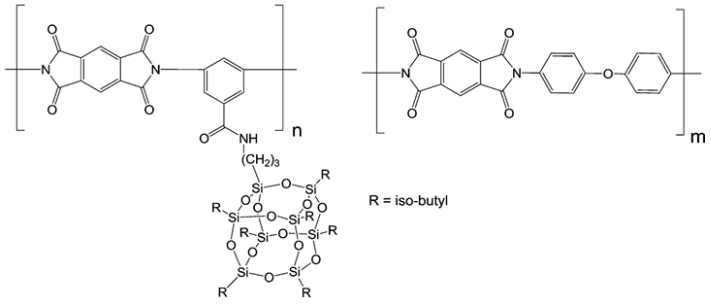

(b) Pendant side-chain (SC) attachment

Figure 6.1: Schematic representation of POSS macromolecular architectures within a polymer matrix. (a) Main-chain (MC) incorporation, where the inorganic POSS cage is directly integrated into the polymer backbone as a structural segment. (b) Pendant side-chain (SC) attachment, where the cage is tethered to the primary chain via a functionalized organic spacer. In both configurations, the rigid inorganic core (Si-O) serves as the primary ash precursor for the silica passivation layer, while the surrounding organic corona dictates the initial steric hindrance and matrix compatibility. Retrieved from Minton et al. [150]

Before applying the mathematical model, it is essential to analyze the qualitative consistency of the experimental data collected from different exposure environments. To ensure a robust validation, the erosion kinetics were monitored in two distinct scenarios: direct LEO exposure and accelerated ground-based simulation. Figure 6.2 presents the cumulative mass loss (for unit of area) trends for both datasets.

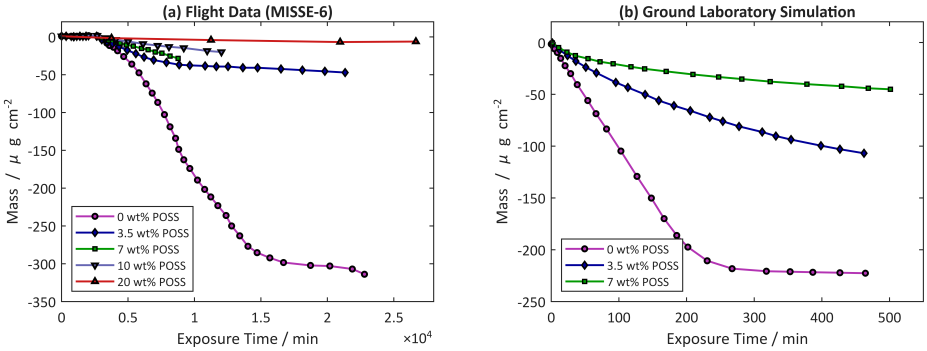

Figure 6.2: Experimental erosion kinetics overview. Comparison of mass loss trends in (a) real LEO environment (MISSE-6 flight data) and (b) ground-based laboratory simulation. Both environments clearly exhibit the transition from linear erosion (for pure polymer) to self-passivating non-linear behavior (for nanocomposites). Retrieved from Minton et al. [150]

The mass loss measurements, presented in Figure 6.2, reveal two distinctly different kinetic regimes depending on the material composition.

- *Linear Erosion of Pristine Polyimide:* The control samples (0 % POSS) exhibit a linear mass loss trend throughout the entire exposure duration. As shown in the experimental dataset, the erosion proceeds at a constant rate (approximately linear slope), confirming that the pristine polymer undergoes continuous degradation without the formation of any protective surface layer. This linear slope also provides the experimental basis for the determination of the parameter R_0 defined as the initial erosion rate of the pristine material. This constant mass loss behavior aligns with the reaction-limited regime described in the theoretical analysis, where the absence of inorganic precursors prevents the "blocking" mechanism from taking place. It is crucial to observe that the change in slope (plateau) detectable in the final stages of the 0% sample exposure does not indicate a kinetic stabilization. Instead, it simply signifies that the polymer film has been *completely eroded* (sample burn-through) at that specific fluence, effectively marking the structural end-of-life of the specimen.
- *Non-Linear Passivation of Nanocomposites:* In strong contrast, the POSS-reinforced samples (3.5, 7, 10, 20 %) display a marked non-linear behavior.
  - Transient Phase: In the initial stages, the mass loss increases, but the rate (slope) rapidly decelerates.
  - Saturation Phase: As the exposure fluence increases, the curves tend to flatten out, asymptotically approaching a plateau.

This deceleration confirms the self-passivating nature of the material (intrinsic to the POSS-polyimide system and not an artifact of a specific testing facility): the accumulation of the silica layer progressively hinders the oxygen flux, shifting the system from a reaction-controlled to a diffusion-controlled regime. Notably, the "flattening" of the curve occurs earlier and more abruptly for higher POSS loadings (e.g., 20 %), suggesting that the protective efficiency is strictly dependent on the filler concentration.

6.3 State of the Art in Erosion Modeling

While the experimental effectiveness of POSS is well-documented [152, 163, 164], the theoretical modeling of its erosion kinetics has historically followed two divergent paths, leaving a gap for engineering-oriented analytical solutions.

At the simplest level, initial mission sizing often relies on phenomenological empirical models. These approaches are based on fitting experimental data with decay functions, typically describing the reduction in erosion yield (E_y) via exponential laws of the form $E_y(F) = E_{y,0}e^{-\beta F} + E_{y,\infty}$, where F is the accumulated fluence. While practically useful for interpolation within a specific dataset, these models lack predictive power outside their calibration range. Crucially, they do not explicitly account for material formulation parameters, such as filler loading or particle size, effectively treating the nanocomposite as a "black box." To investigate the fundamental origins of degradation, researchers have attempted to scale down to the nanoscopic level using Molecular Dynamics (MD) simulations with reactive force fields (ReaxFF). Notable studies by Wei et al. [165] and Zhou et al. [166] successfully elucidated the atomistic pathways of bond scission and pyrolysis, identifying CO and OH as the dominant reaction products. However, despite their high chemical fidelity, these simulations are inherently restricted to extremely short timescales ($t < 40$ ps) and nanometer-length domains. Consequently, while invaluable for understanding *how* a bond breaks, direct extrapolation from MD to the realistic lifespan of engineering components remains computationally impractical. On the opposite end of the spectrum, researchers have developed high-fidelity computational schemes to simulate the atom-by-atom interaction over large domains. Notable examples include the Monte Carlo codes developed by Tagawa et al. [154, 167]. Complementing these efforts, at larger scales, Li et al. [168] developed a Monte Carlo statistical model specifically to simulate the undercutting process associated with AO erosion of polyimide films. Their model successfully reproduced experimentally observed erosion morphologies at diverse orbital incidence angles, demonstrating that increasing AO fluence leads to deeper and wider undercutting features. The simulations further predicted maximum penetration depths on the

order of tens of micrometers, with erosion depth exceeding width at normal incidence and becoming more comparable at higher orbital angles. In the realm of analytical modeling, Chen et al. [145] proposed a unified kinetic framework based on chain reaction theory and fractal geometry. While this approach represents a significant step forward by solving differential mass-balance equations, it is limited by an extensive reliance on fitting constants. The model requires the calibration of multiple fractal kinetic parameters against existing experimental data to reproduce the erosion curves. Consequently, it does not provide a direct predictive link between the *a priori* material formulation (e.g., filler volume fraction) and the erosion resistance, limiting its utility as a pure design tool for new materials. These simulations accurately capture the physics of scattering, surface roughening, and the stochastic nature of "scavenging" the organic matrix. However, despite these capabilities, they present significant limitations for engineering applications. First, these methods are computationally expensive and ill-suited for rapid design optimization. They require substantial calculation time to simulate meaningful timescales and physical domains, making them impractical for conducting extensive sensitivity analyses on filler content. Second, while such models capture important geometric aspects of AO erosion, they do not explicitly account for the coupled evolution of chemical composition and mechanical response.

Collectively, these studies underscore a *critical unmet need*: the absence of a multiscale, thermodynamically and physics consistent modeling framework that can bridge experimentally observed chemical degradation mechanisms with macroscopic mechanical behavior under prolonged AO exposure. Addressing this gap is essential for enabling predictive design, lifetime assessment, and risk mitigation strategies for polymer-based spacecraft components operating in LEO and VLEO environments. Consequently, there exists a clear need for an intermediate approach: a physics-based semi-analytical model. Such a model should retain the connection to the microstructure (characteristic of Monte Carlo methods) but offer the closed-form solvability of empirical equations. The percolation framework proposed in this thesis aims to fill this gap, providing a direct correlation between the initial filler volume fraction of POSS and the final eroded depth measured in the material after the accomplishment of the mission.

6.4 Physical and Mathematical Description of the Problem

As analyzed in the previous sections, experimental observations on POSS-polyimides exposed to LEO reveal a self-passivating behavior. The erosion rate, initially high, decreases over time as a stable inorganic layer forms on the surface. Hence, from a physical point of view we can identfy a phenomena of surface erosion with barrier formation. To model this phenomenon, we assume the material system consists of two distinct dynamic domains separated by a moving interface that we define as $z = h(t)$:

1. The Passivating Silica Layer S_iO_2 $(0 \leq z \leq h(t))$: An amorphous silica-rich scale formed by the oxidation of the POSS cages contained in different positions of the base polymer chains. It acts as a diffusive barrier for the incoming oxygen.

2. The Virgin Polymer $(z > h(t))$: The unreacted nanocomposite bulk.

Figure 6.3 provides a schematic illustration of this physical model, highlighting the interface evolution between the protective silica scale and the underlying bulk material.

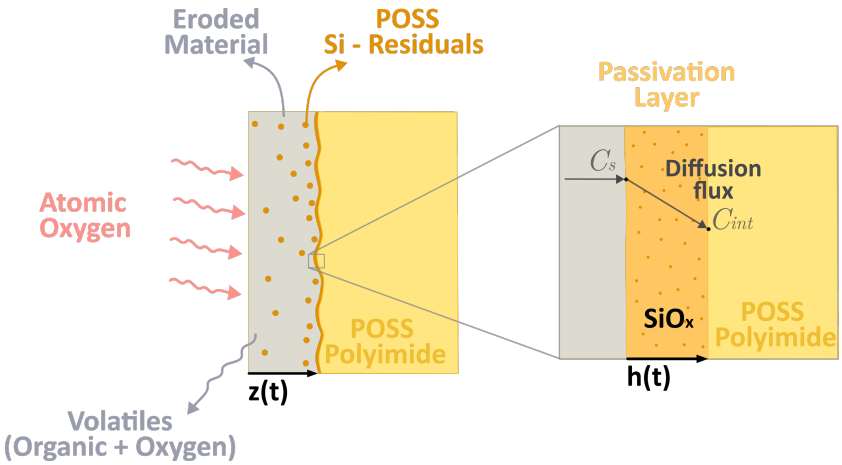

Figure 6.3: Schematic representation of the physical model adopted for POSS-based nanocomposites erosion. The system is idealized as a two-layer structure: the growing passivation layer (amorphous silica, SiO_2) and the underlying virgin polymer bulk. The moving boundary $z = h(t)$ represents the oxidation front, which progresses into the material as the polymer matrix is consumed, governed by the diffusion of atomic oxygen through the silica barrier.

The erosion process is governed by two competing mechanisms occurring in series:

1. *Diffusion:* AO must diffuse from the exposed surface ($z = 0$) through the growing silica layer to reach the reaction front.

2. *Reaction:* At the interface $z = h(t)$, AO reacts with the organic matrix, releasing volatile products and leaving behind new inorganic silica residues that thicken the barrier.

6.4.1 Fundamental Assumptions

The erosion process is mathematically formulated as a phase transition, one-dimensional moving boundary problem (classically known as a Stefan problem). Specifically, the model relies on four fundamental assumptions, justified by the physicochemical timescales and the specific geometry of the interaction:

- *1D approximation:* Given the spatial uniformity of the incident AO flux and the planar geometry of the sample (where the thickness is orders of magnitude smaller than the lateral dimensions), edge effects are neglected [145, 156, 169]. The erosion and passivation processes are assumed to occur exclusively along the direction perpendicular to the exposed surface (z-axis). The problem is thus reduced to a single spatial dimension, describing the evolution of the interface position $h(t)$.

- *Inert Barrier & Localized Reaction:* The silica layer formed during exposure is assumed to be chemically inert towards atomic oxygen. Consequently, no consumption of oxygen occurs within the bulk of the oxide scale ("No Reaction in the Bulk"). The chemical reaction is strictly localized at the moving interface $z = h(t)$, where the diffusing oxygen meets the virgin polymer.

- *Quasi-Steady-State (QSS) Approximation:* This assumption relies on the separation of timescales. The characteristic time of oxygen diffusion across the thin silica layer is orders of magnitude smaller than the characteristic time of the passivation layer growth) [158, 170, 171]. Mathematically, this implies that the oxygen concentration field relaxes instantaneously to the changing thickness $h(t)$. Under this condition, the accumulation of oxygen within the layer is negligible, resulting in a linear concentration profile across the barrier. This simplification allows us to treat the diffusion process as a sequence of steady-state snapshots rather than a full transient problem.

- *Stoichiometric Silicon Mass Conservation:* The growth of the barrier is governed by the strict conservation of Silicon atoms. Unlike the organic backbone

of the polymer, which volatilizes upon reaction with atomic oxygen (forming CO, CO_2, etc.), the inorganic silicon cores of the POSS cages are non-volatile. Consequently, *for every unit volume of polymer eroded, a specific volume of silica is inevitably produced.* This relationship holds true because the POSS filler is assumed to be homogeneously dispersed: the erosion of the matrix exposes a fixed number of Si atoms per unit depth, which immediately oxidize to form the SiO_2 network. This stoichiometric conversion factor depends solely on the material densities and the initial filler loading: higher loadings result in a larger volume of oxide available to form the protective scale. This assumption establishes the physical link between the microscopic chemical reaction rate and the macroscopic velocity of the moving interface.

In the following section, these assumptions are translated into a system of mass balance equations, globally accounting for the transport and consumption of the three active species: the atomic oxygen (diffusing species), the Silica (passivating species), and the polyimide matrix (reacting species).

6.4.2 Oxygen Mass Balance and Transport

Let $C_{ox}(z,t)$ denote the molar concentration of atomic oxygen diffusing through the passivating silica layer. The spatial domain of the problem extends from the exposed outer surface ($z = 0$), where the concentration is assumed constant at C_s, to the moving interface with the virgin polymer ($z = h(t)$), where the concentration is denoted as C_{int}.

The spatio-temporal evolution of the oxygen concentration within this domain is governed by the general principle of mass conservation:

$$\frac{\partial C_{ox}}{\partial t} = -\nabla \cdot \mathbf{J}_{ox} + R_{ox} \tag{6.1}$$

where:

- $\mathbf{J}_{ox}$ represents the flux vector of the diffusing species (atomic oxygen);
- R_{ox} is the net volumetric generation or consumption rate of oxygen within the domain (inside the layer);
- $\nabla \cdot (\cdot)$ denotes the divergence operator.

Considering first the 1D assumption, the equation is specialized as:

$$\frac{\partial C_{ox}}{\partial t} = -\frac{\partial J_{ox}}{\partial z} + r_{ox} \tag{6.2}$$

Applying the QSS approximation, the transient term vanishes ($\partial C_{ox}/\partial t \approx 0$), as the characteristic timescale of diffusion is negligible compared to that of the layer

growth. Furthermore, consistent with the assumption of a chemically inert silica barrier where the reaction is localized exclusively at the interface, the volumetric reaction rate within the silica layer domain is null ($r_{ox} = 0$). Consequently, the mass balance equation simplifies to a steady-state condition where the diffusive flux is spatially uniform:

$$\frac{\partial J_{ox}}{\partial z} = 0 \implies J_{ox}(z) = \text{constant} \tag{6.3}$$

At this point, to relate the diffusive flux to the concentration gradient, we consider Fick's first law:

$$J_{ox} = -D_{\text{eff}}(P)\ \frac{\partial C_{ox}}{\partial z} \tag{6.4}$$

Here, $D_{\text{eff}}(P)$ denotes the effective diffusivity of oxygen through the silica layer. It is crucial to note that this parameter is considered functionally dependent on the initial POSS mass fraction (P). Consistent with classical transport theories in heterogeneous media [172, 173], the interconnectivity of the inorganic phase governs the macroscopic diffusivity: as the filler loading increases, the diffusion paths become increasingly tortuous or blocked. This dependence constitutes the core hypothesis of the geometric percolation model developed in the subsequent sections. Combining the steady-state condition derived previously ($J_{ox} = \text{constant}$) with Eq.(6.4) implies that the concentration gradient ($\partial C_{ox}/\partial z$) must also be constant across the layer. This confirms the linear concentration profile assumed by the Deal-Grove model, representing a constant drop in oxygen potential from the surface to the interface.

To derive the explicit magnitude of this flux, we integrate Eq.(6.4) over the layer thickness $h(t)$, imposing the boundary conditions $C_{ox}(z = 0) = C_s$ (constant surface concentration) and $C_{ox}(z = h(t)) = C_{int}$ (interface concentration):

$$J_{ox} \int_0^{h(t)} dz = -D_{\text{eff}}(P) \int_{C_s}^{C_{int}} dC_{ox} \tag{6.5}$$

Solving the integral yields:

$$J_{ox} \cdot h(t) = D_{\text{eff}}(P) \cdot (C_s - C_{int}) \tag{6.6}$$

Rearranging for the flux, we obtain the governing equation for the diffusion-limited regime:

$$\textbf{(Diffusive Flux)} \quad \boxed{J_{ox} = D_{\text{eff}}(P)\frac{C_s - C_{int}}{h(t)}} \tag{6.7}$$

This relationship mathematically demonstrates the self-passivating nature of the process: as the barrier thickness $h(t)$ increases, the flux of oxidizing species reaching the polymer interface decreases inversely, progressively slowing down the erosion rate.

6.4.3 Interface Reaction Kinetics

At the moving interface ($z = h(t)$), the arriving atomic oxygen is consumed by the oxidative degradation of the polymer matrix. Assuming a first-order reaction kinetics with respect to the interfacial oxygen concentration:

$$\boxed{J_{reac} = k_{reac} \cdot C_{int}} \quad \textbf{(Reactive flux)} \tag{6.8}$$

where k_{reac} represents the intrinsic reaction rate constant of the virgin polymer. Imposing the continuity of flux at the interface, a fundamental step in the Deal-Grove derivation requires that, under QSS conditions, the rate of oxygen arriving by diffusion must equal the rate of oxygen consumed by the reaction ($J_{ox} = J_{reac} = J_{tot}$). By equating Eq. (6.7) and Eq. (6.8), we can isolate the unknown interface concentration C_{int}:

$$D_{\text{eff}}(P)\ \frac{C_s - C_{int}}{h(t)} = k_{reac} \cdot C_{int} \implies C_{int} = \frac{C_s}{1 + \frac{k_{reac} \cdot h(t)}{D_{\text{eff}}(P)}} \tag{6.9}$$

Substituting this expression back into the reactive flux equation (6.8), we obtain the constitutive Deal-Grove type equation for the total erosion flux:

$$\boxed{J_{tot} = \frac{C_s}{\frac{1}{k_{reac}} + \frac{h(t)}{D_{\text{eff}}(P)}}} \quad \textbf{(Total flux conservation)} \tag{6.10}$$

This formulation highlights a direct analogy with electrical circuits: the erosion process is driven by a potential difference (oxygen concentration, analogous to voltage) and impeded by two resistances in series:

- *Chemical Resistance* ($R_{chem} = 1/k_{reac}$): dominant when the layer is thin (reaction-limited regime).
- *Diffusive Resistance* ($R_{diff} = h(t)/D_{\text{eff}}(P)$): dominant as the layer grows (diffusion-limited regime).

6.4.4 Evolution of the Passivation Layer

The evolution of the barrier thickness is governed by the mass balance at the moving interface. The growth rate of the silica layer is considered directly proportional to the flux of oxygen (and so to the amount of atomic oxygen atoms) reacting at the interface with the polymer. Let Ω denote the volumetric conversion factor (representing the volume of silica formed per mole of oxygen consumed). The kinematic relationship for the interface evolution, mathematically known as the Stefan condition for a moving boundary problem [158, 174], is expressed as:

$$\frac{dh}{dt} = \Omega \cdot J_{tot} \tag{6.11}$$

By substituting the expression derived for the total flux (Eq.6.10) into this kinematic condition, we obtain the governing ODE that describes the rate of growth of the passivation layer:

$$\frac{dh}{dt} = \frac{\Omega \cdot C_s}{\frac{1}{k_{reac}} + \frac{h(t)}{D_{\text{eff}}(P)}} \tag{6.12}$$

While Eq. (6.12) describes the microscopic evolution of the layer thickness $h(t)$, experimental measurements typically quantify the macroscopic mass loss of the sample. The following section will bridge this gap, establishing the analytical link between the theoretical variable $h(t)$ and the experimentally observable mass loss.

6.5 Experimental Correlation and Scaling

The experimental datasets available for validation, derived from both MISSE-6 flight exposure and ground-based laboratory simulations, primarily quantify the erosion process via gravimetric measurements. Specifically, the data report the cumulative mass loss per unit area, denoted as $\Delta m(t)$ $[\mu g/cm^2]$, rather than the direct evolution of the passivation layer thickness $h(t)$. Consequently, to validate the governing ODE derived in the previous section, it is necessary to establish a rigorous scaling relation. This formulation must link the theoretical geometric variable $h(t)$ (the growth of the oxide scale) to the experimental gravimetric observable $\Delta m(t)$ (the net mass removed from the sample).

6.5.1 The Scaling Factor S

The thickness of the generated silica layer $h(t)$ is related to the specific mass lost through a stoichiometric conversion factor. The derivation of this scaling coefficient proceeds as follows:

1. *POSS Mass Fraction:* The total mass (not specific) of POSS cages involved in the erosion process (M_{POSS}) is proportional to the total mass lost by the polymer (M_{lost}) via the initial weight percentage P:

$$M_{POSS} = M_{lost} \cdot P \tag{6.13}$$

2. *Stoichiometric Conversion:* Upon oxidation, the organic groups surrounding the POSS cage degrades, leaving behind an inorganic silica residue (SiO_2). The mass of silica formed (M_{SiO_2}) is related to the reacting POSS mass by the stoichiometric yield factor ψ (defined as the ratio of molecular weights MW_{SiO_2}/MW_{POSS}):

$$M_{SiO_2} = M_{POSS} \cdot \psi = (M_{lost} \cdot P) \cdot \psi \tag{6.14}$$

3. *Volume of the Layer:* Assuming the silica forms a layer with density ρ_{SiO_2}, the volume of the generated oxide scale is:

$$V_{SiO_2} = \frac{M_{SiO_2}}{\rho_{SiO_2}} \tag{6.15}$$

4. *Thickness Calculation:* Considering a sample surface area A, the thickness $h(t)$ is obtained by dividing the volume by the area. Substituting the expression for the specific mass loss per unit area $m_{loss} = M_{lost}/A$, we obtain:

$$h(t) = \frac{V_{SiO_2}}{A} = \frac{M_{SiO_2}}{\rho_{SiO_2} \cdot A} = \frac{M_{POSS} \cdot \psi}{\rho_{SiO_2} \cdot A} = \frac{M_{lost} \cdot P \cdot \psi}{\rho_{SiO_2} \cdot A} = \frac{(m_{loss} \cdot A) \cdot P \cdot \psi}{\rho_{SiO_2} \cdot A} \tag{6.16}$$

Simplifying the area A, we arrive at the final linear relationship:

$$h(t) = \underbrace{\left(\frac{\psi}{\rho_{SiO_2}}\right)}_{S} \cdot P \cdot |m_{loss}(t)| \tag{6.17}$$

where P is the mass percentage of POSS (e.g., 0.07 for 7 wt%). The resulting scaling factor S [cm^3/g] accounts for the density differences and the chemical yield of the oxidation reaction, allowing to account for the transformation from reacted POSS mass to generated Silica layer.

$$S = \frac{Stoichiometric\ yield\ (\psi)}{Silica\ density\ (\rho_{SiO_2})} \tag{6.18}$$

To implement the scaling relation (Eq. 6.17), and to obtain a physical consistent value for this scaling factor, specific physical constants related to the material system must be defined.

- Silica Density (ρ_{SiO_2}): The passivating layer is assumed to be amorphous silica formed by oxidative degradation. We adopt the standard density value for vitreous silica:

$$\rho_{SiO_2} \approx 2.2, \mathrm{g/cm^3} \tag{6.19}$$

- Stoichiometric Yield ψ: This parameter represents the mass efficiency of the conversion from the organosilicon cage to the inorganic oxide. It is defined as the ratio of the molecular weight of the silica produced to the molecular weight of the initial POSS cage:

$$\psi = \frac{\text{Mass of } SiO_2 \text{ formed}}{\text{Mass of POSS reacted}} \tag{6.20}$$

Considering for this specific study the oxidation of the octaisobutyl-POSS cage, the reaction can be idealized as:

$$Si_8O_{12}R_8 + O_{atomic} \longrightarrow 8SiO_2 + \text{volatile products} \tag{6.21}$$

During the oxidation reaction, when AO impacts the POSS cages, it consumes all the organic groups R, leaving only an inorganic nucleus that captures oxygen to become a stable Silica compound (SiO_2) The calculation of the molar masses proceeds as follows:

1. *Final Mass of Silica ($8 \cdot SiO_2$):* Using the standard atomic weights ($MW_{Si} \approx 28.08\,\text{g/mol}$ and $MW_O \approx 16$ [g/mol]), the molecular weight of a single silica unit is:

$$MW_{SiO_2} \approx 28.08 + 2 \cdot (16) = 60.08 \text{ [g/mol]} \tag{6.22}$$

   Since each POSS cage contains 8 Silicon atoms, the total inorganic mass produced (assuming that all the Silicon from the POSS transforms into the passivate layer) is:

$$\text{Total Inorganic Mass} = 8 \cdot 60.08 = 480.64 \text{ [g/mol]} \tag{6.23}$$

2. *Initial POSS Mass:* The initial mass depends on the specific type of POSS used in the composite. For this analysis, we assume an average molecular weight value of:

$$MW_{POSS} \approx 977 \text{ [g/mol]} \tag{6.24}$$

By combining these values, we obtain the yield factor ψ:

$$\boxed{\psi = \frac{\text{Mass of } SiO_2 \text{ formed}}{\text{Mass of POSS reacted}} = \frac{8 \cdot MW_{SiO_2}}{MW_{POSS}} = \frac{480.64}{977} \approx 0.49} \tag{6.25}$$

This result implies that for each gram of POSS that reacts, approximately half a gram of Silica compound remains on the surface, while the other half escapes as volatile species.

Finally, substituting this yield into the definition of the scaling factor:

$$S = \frac{\psi}{\rho_{SiO_2}} = \frac{0.49}{2.2} \approx 0.22 \text{ [cm}^3\text{/g]} \tag{6.26}$$

This parameter S allows the direct conversion of the gravimetric mass loss into the passivation layer thickness $h(t)$.

It is worth to note that throughout this analytical derivation, the passivating layer is idealized as pure, fully dense amorphous silica (SiO_2). In reality, as extensively documented in experimental LEO flight data and ground-based AO simulations, the oxide scale formed on POSS-nanocomposites is a complex, sub-stoichiometric silicon oxide (SiO_x, where x typically ranges between 1.8 and 2.0). Furthermore, this layer may contain trace amounts of unreacted organic residuals, localized porosity, or micro-cracks induced by internal stresses during the conversion process. Consequently, while the stoichiometric assumption of perfect SiO_2 provides a robust and necessary mathematical closure for the model, the calculated thickness $h(t)$ should be interpreted as an "effective" equivalent thickness rather than an absolute morphological measurement.

6.6 The Governing ODE for Mass Loss

Substituting the geometric scaling relation derived in Eq. (6.17) into the growth rate equation Eq. (6.12), we bridge the gap between the microscopic thickness and the macroscopic mass loss. The resulting, updated ODE describing the erosion kinetics is:

$$S \cdot P \cdot \frac{dm_{loss}}{dt} = \frac{\Omega \cdot C_s}{\frac{1}{k_{reac}} + \frac{S \cdot P \cdot |m_{loss}(t)|}{D_{\text{eff}}(P)}} \tag{6.27}$$

By rearranging the terms and isolating the time derivative of the mass loss, we obtain the explicit form:

$$\frac{dm_{loss}}{dt} = \frac{1}{S \cdot P} \cdot \left(\frac{\Omega \cdot C_s}{\frac{1}{k_{reac}} + \frac{S \cdot P \cdot |m_{loss}(t)|}{D_{\text{eff}}(P)}} \right) \tag{6.28}$$

To achieve a robust formulation suitable for numerical integration and physical interpretation, we multiply the numerator and denominator by k_{reac} and group the constants into two lumped parameters with distinct physical meanings:

- *Initial Erosion Rate (R_0):*

$$R_0 = \frac{\Omega \cdot C_s \cdot k_{reac}}{S \cdot P} \quad \left[\frac{\mu g}{cm^2 \cdot s} \right] \tag{6.29}$$

  This parameter, mentioned briefly before, denotes the intrinsic erosion rate of the nanocomposite at the onset of exposure ($t \to 0$), before the formation of any protective layer. In this regime, the transport resistance is negligible, and the kinetics are solely limited by the reaction rate constant (k_{reac}) of the atomic oxygen with the organic matrix.
  Mathematical Note: It is important to observe that the stoichiometric volume

term Ω is inherently proportional to the mass fraction P (as the volume of oxide generated depends linearly on the mass of precursor available). Consequently, the terms Ω and P in the ratio effectively cancel out. This mathematical simplification carries a crucial physical meaning: R_0 is **invariant** with respect to the filler loading. It represents the constant, baseline reactivity of the pure polyimide matrix, serving as the fixed thermodynamic reference against which the barrier efficiency is measured.

- *Blocking Power (K):*

$$K = \frac{k_{reac} \cdot S \cdot P}{D_{\text{eff}}(P)} \quad \left[\frac{cm^2}{\mu g}\right] \tag{6.30}$$

This parameter is the key metric of the barrier efficiency. From a physical perspective, it embodies the concept of a modified *Damköhler number* (Da), a dimensionless group that compares the speed of the chemical reaction to the speed of diffusion.

  - *Physical Meaning:* It answers the question: "Is the process limited by how fast the oxygen reacts or by how fast it arrives at the interface?"
  - *Interpretation:* Based on its definition, a high value of K indicates that diffusion is much slower than the surface reaction. As will be shown in the governing ODE below, this parameter acts as a bottleneck, successfully "choking" the erosion process and forcing the system into a safe, diffusion-limited regime.

Substituting these parameters into the Eq. 6.28, the governing ODE takes the form:

$$\frac{dm_{loss}}{dt} = \frac{R_0}{1 + K \cdot |m_{loss}(t)|} \tag{6.31}$$

This equation is mathematically isomorphic to the classical *Deal-Grove model*, originally derived for the thermal oxidation of silicon [158]. In our context, the equation captures the self-passivating nature of the erosion process through a non-linear feedback mechanism:

- As the cumulative mass loss $m_{loss}(t)$ increases, it acts as a proxy for the growing thickness of the silica barrier.
- Consequently, the denominator $(1 + K \cdot |m_{loss}(t)|)$ grows linearly, forcing the instantaneous erosion rate (dm/dt) to decay hyperbolically.

This structure ensures a continuous physical transition from an initial *linear regime* (reaction-controlled, where $dm/dt \approx R_0$) to a long-term *parabolic regime* (diffusion-controlled, where $dm/dt \propto t^{-1/2}$), consistent with the transport theories for barrier formation [158, 175].

6.7 Physical Interpretation of Transport: The Percolation Model

The lumped parameter K (blocking power) defined in the governing equation, as mentioned before, is not merely a fitting coefficient, but it encapsulates the transport properties of the evolving oxide scale. Recalling its definition:

$$K = \frac{k_{reac} \cdot S \cdot P}{D_{\text{eff}}(P)} \tag{6.32}$$

it is evident that for a fixed chemical reactivity (k_{reac}), any variation in K (for fixed type of material, and so for fixed S) is directly driven by changes in the effective diffusivity $D_{\text{eff}}(P)$. Theoretically, this relationship allows us to "un-lump" the experimental results and isolate the diffusivity:

$$D_{\text{eff}}(P) = \frac{k_{reac} \cdot S \cdot P}{K} \tag{6.33}$$

To evaluate this expression quantitatively, a value for the intrinsic microscopic reaction rate k_{reac} is required. However, this parameter is not directly observable in standard erosion tests. To overcome this limitation, we introduce a physically-based approximation. We observe that the macroscopic initial erosion rate (R_0), defined previously, is directly proportional to the intrinsic reactivity of the polymer matrix. Consequently, we can employ R_0 as a macroscopic proxy for the reaction term k_{reac}.

Substituting R_0 into Eq. (6.33), we define an "Operational Effective Diffusivity" (D^*_{eff}):

$$\boxed{D^*_{\text{eff}}(P) \approx \frac{R_0 \cdot S \cdot P}{K}} \tag{6.34}$$

While this value may differ from the absolute diffusion coefficient by a constant proportionality factor, it preserves the functional dependence on the POSS loading P. This derivation validates the procedure used in the numerical analysis: it allows us to extract the diffusivity trend directly from the experimentally fitted parameter (K) and verify if the material behavior follows the topological predictions of the percolation theory [172, 176, 177].

6.7.1 Effective Diffusivity (D_{eff})

The parameter K extracted via the fitting procedure is a lumped coefficient that effectively describes the "blocking" capability of the layer within the mass-balance framework of the numerical model. However, the diffusivity values internally calculated by the code are expressed in specific "working units" derived from the mass-based formulation of the governing equations. To obtain the true physical

effective diffusivity (D_{eff}) in standard units (cm^2/s), a dimensional conversion is necessary to translate the problem from the mass domain to the spatial (thickness) domain. The conversion logic relies on comparing the definition of the blocking power K used in the numerical solver against its theoretical thermodynamic counterpart. In the numerical implementation, K is defined as a function of the initial mass erosion rate R_0:

$$K = \frac{R_0 \cdot S \cdot P}{D^*_{\text{eff}}(P)} \tag{6.35}$$

Conversely, following the strict physical derivation based on Fickian diffusion and reaction kinetics, the same relationship is expressed as a function of the linear reaction velocity constant k_{reac}:

$$K = \frac{k_{reac} \cdot S \cdot P}{D_{\text{eff}}(P)} \tag{6.36}$$

By equating these two expressions, we can isolate the relationship between the model parameters and the physical quantities:

$$D_{\text{eff}}(P) = D^*_{\text{eff}}(P) \left(\frac{k_{reac}}{R_0} \right) \tag{6.37}$$

We recognize that the initial mass loss rate R_0 can be approximated as the product of the linear reaction velocity and the polymer density (ρ_{poly}), i.e., $R_0 \approx k_{reac} \cdot \rho_{poly}$. This implies that the transition from the mass-based rate to the linear recession velocity is governed by the inverse of the material density. Consequently, by substituting this relationship into the equality derived above, and introducing a time conversion factor of 60 to transition from the operational minutes (used for R_0) to the standard seconds, the actual physical effective diffusivity is obtained via the following formula:

$$D_{\text{eff}}(P) = \frac{D^*_{\text{eff}}(P)}{\rho_{poly} \cdot 60} \tag{6.38}$$

This conversion formula establishes the theoretical bridge between the numerical model and the physical domain. Once the blocking power K is calibrated against the experimental mass-loss data, Eq. (6.38) can be applied to extract the actual transport properties of the nanocomposite and properly evaluate the percolation trends.

6.7.2 Percolation Theory and Tortuosity

Physically, the dependence of the diffusivity on the POSS mass fraction P is governed by the topological structure of the passivation layer, and specifically by the connectivity of evolving the silica network. The inorganic silica domains formed by the oxidation of POSS cages act as impermeable obstacles embedded within the matrix. However, the efficiency of this barrier is not linear but depends on the spatial distribution of the precursors:

- *Low Loading (Isolated Regime):* At low POSS concentrations, the molecular cages are spatially isolated within the bulk. When AO attacks, they convert into discrete SiO_2 domains, but the polymer matrix situated between these islands remains exposed. In this regime, the erosion is merely slowed down by the reduction of available surface area, but oxygen can still easily bypass the obstacles.

- *High Loading (Coalescence Regime):* As the concentration increases, the inter-cage distance decreases significantly. When oxidized, the proximity of the precursors facilitates their interaction, leading to oxidative crosslinking. In this state, the generating silica compounds effectively "melt" together, eliminating the interstitial voids and forming a continuous, coherent inorganic shield.

As the initial loading P increases towards the percolation threshold, the system transitions from the isolated regime to the crosslinked regime. This forces the diffusing atomic oxygen to follow increasingly tortuous paths to bypass the coalescing silica network, drastically reducing the effective diffusivity, consistent with the general principles of the percolation [178].

While percolation dictates the geometry of the obstacles, the quantitative reduction in diffusivity is best described by the *Free Volume Theory* [179, 180]. According to this model, the introduction of impermeable fillers linearly reduces the fractional free volume available for diffusion. Mathematically, this dependence translates into an exponential decay of the diffusivity coefficient, a trend widely observed in polymer nanocomposites [181]:

$$D_{\text{eff}}(P) = D_0 \cdot e^{(-\beta \cdot P)} \tag{6.39}$$

where:

- D_0 represents the intrinsic diffusivity reference.

- β is the tortuosity coefficient, a parameter that describes how effectively the specific POSS architecture blocks the diffusion paths (a higher β indicates a more abrupt cutoff of oxygen flux).

In the subsequent sections, the back-calculated physical diffusivity values will be correlated with the POSS volume fraction. A non-linear regression analysis will be performed using Eq. (6.39) to extract these constitutive parameters (D_0 and β) for both flight and laboratory regimes, thereby validating the physical framework and powering the predictive algorithm.

6.7.3 Physicochemical Justification of the Exponential Law

While percolation theory describes the geometric obstruction caused by the silica network (the transition from isolated islands to a connected barrier), the steepness of the exponential decay observed in our data is consistent with the Free Volume Theory applied to transport kinetics [179, 180]. According to this framework, the diffusivity depends exponentially on the available fractional free volume. In our nanocomposite, the rapid consumption of this free volume, and the consequent exponential drop in permeability, is driven by two specific physicochemical mechanisms:

1. *Self-Healing Kinetics:* During oxidation, surface silanol groups (Si-OH) are generated. At high concentrations, the probability of two reactive groups meeting increases exponentially as the average distance reduces, triggering rapid condensation reactions ($\text{Si-OH} + \text{HO-Si} \rightarrow \text{Si-O-Si} + \text{H}_2\text{O}$). As observed in X-ray photoelectron spectroscopy (XPS) studies on POSS-polyimides by Verker et al. [182], this chemically driven mechanism allows the surface to "heal" defects, close pores, and crosslink into a coherent silicate network faster than the atomic oxygen can penetrate the bulk, effectively reducing the available volume for diffusion [150].

2. *Thermodynamical Densification:* The AO flux provides the kinetic energy to compact the surface layer. While low loadings leave interstitial voids due to carbon volatilization, high loadings allow the structure to collapse into a compact, glassy SiO_2 layer (vitrification). As noted in literature [183], the gas permeability of such a dense glassy layer is orders of magnitude lower than that of a porous oxide, justifying the sharp jump in protection efficiency captured by the coefficient β.

These mechanisms act synergistically with the geometric tortuosity to produce the characteristic exponential blocking behavior defined in the model.
This theoretical framework provides a clear validation criterion: if the Deal-Grove model is physically consistent, the diffusivity values extracted from the experimental fitting of K must align with the exponential trend predicted by Eq. (6.39), confirming the synergistic action of the mechanisms described above.

6.8 Numerical Implementation and Validation Strategy

To validate the theoretical framework, the governing ODE derived in Eq. (6.31) was solved numerically and calibrated against the experimental datasets described in Section 6.2. The implementation was performed in the MATLAB environment, adopting a robust single-parameter optimization strategy to ensure the physical consistency of the results. Unlike standard empirical fitting approaches where all coefficients are treated as free variables, our physical model imposes strict constraints based on the material properties. Consistent with the matrix homogeneity assumption, the baseline erosion rate (R_0) of the nanocomposite is assumed to be identical to that of the pristine polymer. Therefore, this parameter is fixed *a priori* based on the well-documented erosion yield of pure Kapton/Polyimide in the LEO environment. Based on the extensive experimental database provided by Minton and NASA reports [148–150] for LEO exposure, we adopted the fixed value:

$$R_0^{\text{flight}} = 0.0257 \quad \left[\frac{\mu\text{g}}{\text{cm}^2 \cdot \text{min}}\right] \tag{6.40}$$

Conversely, for the ground laboratory simulation, a theoretical value is not applicable since the atomic oxygen flux is facility-dependent and significantly accelerated compared to flight conditions. To determine the correct input parameter, we performed an experimental calibration directly on the test batch. Leveraging the mathematical invariance derived in Eq. (6.29), which establishes that the intrinsic erosion rate R_0 is independent of the filler loading, we isolated the reaction kinetics of the pristine matrix. Specifically, R_0^{lab} was calculated as the linear regression slope of the mass loss curve for the 0 wt% POSS control sample during the initial exposure phase. This procedure yielded a value of:

$$R_0^{\text{lab}} = \frac{dm_{loss,0\%}}{dt} \approx 0.9929 \quad \left[\frac{\mu\text{g}}{\text{cm}^2 \cdot \text{min}}\right] \tag{6.41}$$

This experimentally derived rate, being approximately two orders of magnitude higher than the flight rate, correctly captures the accelerated nature of the ground testing environment and serves as the baseline input for all nanocomposite simulations. Consequently, the optimization problem is reduced to identifying the unique unknown parameter: the blocking power K, which captures the specific protective efficiency of the POSS loading.

Since the governing ODE is non-linear with respect to the accumulated mass loss, the solution was computed via numerical integration using an adaptive step-size Runge-Kutta (4,5) method (specifically the Dormand-Prince pair). The validation procedure follows these steps for each dataset:

1. *Forward Simulation:* For a trial value of K, the solver integrates the rate equation over the exposure time domain:

$$\frac{dm}{dt} = -\frac{R_0}{1 + K \cdot |m_{loss}(t)|}, \quad m_{loss}(0) = 0 \tag{6.42}$$

   generating the theoretical mass loss curve $m_{sim}(t)$.

2. *Objective Function:* The algorithm calculates the discrepancy between the numerical prediction $m_{sim}(t)$ and the experimental data points $m_{exp}(t)$. The objective function $\mathcal{E}(K)$ is defined as the Mean Squared Error (MSE):

$$\mathcal{E}(K) = \frac{1}{N} \sum_{i=1}^{N} \left(m_{sim}(t_i; K) - m_{exp}(t_i) \right)^2 \tag{6.43}$$

   where N is the number of experimental observations.

3. *Optimization:* The optimal value of K is identified by minimizing $\mathcal{E}(K)$ using a bounded scalar minimization algorithm, which combines golden-section search and parabolic interpolation. This method ensures that the extracted parameter lies within a physically meaningful range ($K \geq 0$) and converges to the global minimum of the error surface.

Once the optimal blocking power K is determined for each POSS weight fraction P, the operational effective diffusivity $D^*_{\text{eff}}(P)$ is "un-lumped" from the aggregate parameter using the inverted definition derived in Eq. (6.30):

$$D^*_{\text{eff}}(P) = \frac{R_0 \cdot S \cdot P}{K} \tag{6.44}$$

As established in Section 6.7.1, this operational value is subsequently converted into the true physical diffusivity D_{eff} (expressed in cm^2/s) by accounting for the polymer density and the temporal unit conversion. The resulting set of discrete physical diffusivity values is then analyzed to validate the model. Specifically, the procedure involves:

1. *Trend Analysis:* The extracted $D_{\text{eff}}(P)$ values are plotted against the filler percentage P to inspect the functional dependence of the transport property on the loading.

2. *Constitutive Calibration:* A non-linear regression analysis is performed on these empirical points using the theoretical percolation law defined in Eq. (6.39). This step aims to verify if the exponential model can accurately capture the observed decay and to calibrate the constitutive parameters:

- D_0: The intrinsic diffusivity reference.
- β: The tortuosity coefficient characterizing the barrier efficiency.

The quality of this secondary fit serves as the final confirmation of the link between the macroscopic erosion protection and the microscopic percolation topology.

Upon determining the constitutive parameters of the percolation law for both the flight and the laboratory datasets, the modeling framework transitions from an "inverse characterization tool" to a "forward predictive tool". To rigorously validate the theory, a predictive algorithm was implemented to simulate the erosion behavior of the nanocomposites based solely on their initial material formulation, without relying on individual experimental data points for local fitting. The predictive workflow operates according to the following scheme:

1. *Input Definition:* The user defines the environmental condition (Flight or Lab flux, determining also R_0^{lab}) and the specific filler loading (P).
2. *Property Estimation:* Instead of fitting K, the code utilizes the calibrated percolation law (Eq. (6.39)) to compute the true effective diffusivity D_{eff} *a priori*.
3. *Parameter Re-lumping:* The predicted physical diffusivity is converted back into the model's operational parameter, the blocking power K, via the inverse geometric relationship.
4. *Blind Simulation:* The governing ODE is integrated using this predicted K.

The comparison between these numerical predictions and the experimental mass loss histories serves as the ultimate validation of the framework. A high degree of correlation confirms that the model successfully captures the multiscale physics, bridging the gap between the microscopic percolation topology and the macroscopic erosion resistance.

However, the true engineering potential of this computational tool extends far beyond the mere reproduction of the primary experimental dataset. To demonstrate this, the framework was deployed to forecast the material's behavior under a separate ground-testing campaign previously conducted by the same research group [184]. Remarkably, the percolation law derived from the first environment demonstrated exceptional transferability: it successfully predicted the experimental mass loss in this new framework without requiring any further tuning or recalibration of the parameters. This blind predictive capability represents a critical achievement; it proves that the code is intrinsically rooted in the physical mechanisms of degradation rather than being phenomenologically fitted to a specific test. Consequently, it establishes the model as a highly robust, predictive engineering tool capable of anticipating material performance across different operational envelopes.

6.9 Results and Model Validation

Following the validation strategy outlined in the previous section, the governing ODE was calibrated against the experimental datasets to extract the transport properties of the passivation layer. With R_0 fixed, the numerical solver was employed to identify the optimal blocking power K for each nanocomposite loading. The parameter extraction was performed by minimizing the discrepancy between the numerical solution of the ODE and the experimental datasets.

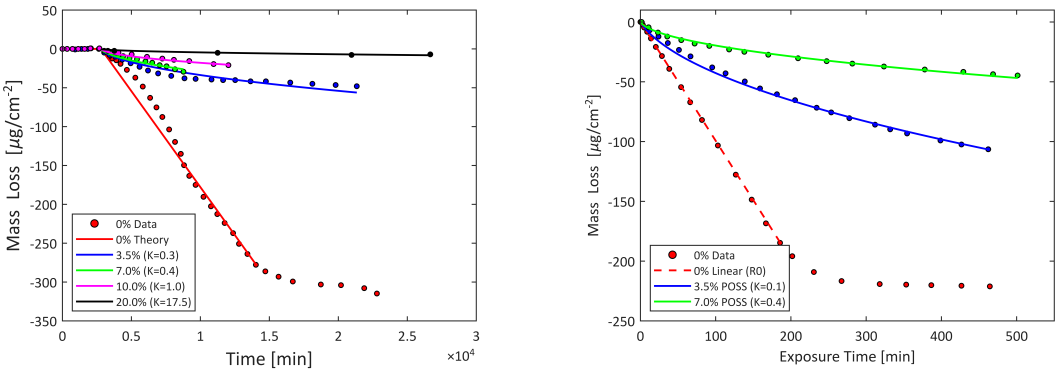

(a) Flight data (MISSE-6). Model fitting against long-duration space exposure. Note the accurate prediction of the saturation plateau for 10 wt% and 20 wt% samples.

(b) Laboratory data. Model fitting against high-flux ground simulation. The inset highlights the initial linear erosion phase before passivation occurs.

Figure 6.4: Numerical reconstruction of erosion kinetics. Comparison between the calibrated analytical model (solid lines) and experimental mass loss data (symbols) in two distinct environments. The model successfully scales from the low-flux flight regime (a) to the high-flux laboratory regime (b).

Figure 6.4 presents the comparison between the numerical solutions and the experimental datasets. The visual agreement confirms the robustness of the physical model:

1. *Regime Transition:* The model naturally captures the transition from the reaction-limited regime (linear initial phase) to the diffusion-limited regime (saturation).
2. *Passivation Onset:* The "knee" of the curve, representing the percolation of the silica network, is accurately reproduced for all filler fractions.
3. *Long-term Stability:* The saturation levels at high fluences are correctly predicted without the need for additional empirical decay terms.

6.9.1 Extraction of Physical Transport Properties

Applying the dimensional conversion defined in Section 6.7.1 to the fitted parameters K, using the density of the virgin polymer ($\rho_{poly} \approx 1.42\,\mathrm{g/cm^3}$), we obtained the physical effective diffusivity values (D_{eff}) summarized in Table 6.1.

Table 6.1: Extraction of physical transport properties. The true effective diffusivity (D_{eff}) is back-calculated from the operational blocking power. The difference in orders of magnitude between Flight and Lab environments reflects the highly accelerated nature of the ground simulation.

	Flight (MISSE-6)		**Lab (High Flux)**	
POSS Loading (wt%)	$K_{(calibrated)}$ [$\mathrm{cm^2/\mu g}$]	$D_{\mathbf{eff}}$ [$10^{-18}\mathrm{cm^2/s}$]	$K_{(calibrated)}$ [$\mathrm{cm^2/\mu g}$]	$D_{\mathbf{eff}}$ [$10^{-15}\mathrm{cm^2/s}$]
3.5	0.32	6.58	0.06	3.45
7.0	0.46	9.22	0.41	1.04
10.0	1.39	4.36	–	–
20.0	17.48	0.29	–	–

The magnitude of these back-calculated transport properties provides a strong *a posteriori* validation of the model's physical soundness. As illustrated in the results:

- *Absolute Magnitude:* The extracted values are dramatically lower than the typical diffusion coefficients of gases (such as oxygen) in pristine glassy polymers, which generally fall in the 10^{-8} to $10^{-11}\,\mathrm{cm^2/s}$ range. Reaching values in the order of $10^{-15}\,\mathrm{cm^2/s}$ (and down to $10^{-18}\,\mathrm{cm^2/s}$) confirms that the transport mechanism is no longer governed by a polymeric matrix. Instead, it proves that the atomic oxygen is diffusing through a dense, inorganic silica (SiO_2) passivation layer, with the surface effectively behaving as an impermeable ceramic glass.

- *Environmental Dependence (Lab vs. Flight):* The model elegantly captures the thermodynamic difference between the two exposure environments. The laboratory values ($\sim 10^{-15}\,\mathrm{cm^2/s}$) are representative of an accelerated, high-energy testing facility. In this regime, the rapid oxygen bombardment, coupled with localized thermal effects, likely generates a more stressed, amorphous, and comparatively porous oxide layer. Conversely, the flight data from MISSE-6 ($\sim 10^{-18}\,\mathrm{cm^2/s}$) reflect a prolonged, low-flux exposure in the authentic LEO environment. The slow degradation rate and extreme thermal cycling allow for the formation of a highly relaxed, tightly packed, and defect-free silica network, minimizing the diffusivity.

- *Network Tightening:* Within each respective environment, the progressive drop in diffusivity as the POSS loading increases (e.g., dropping from 6.58×10^{-18} at 3.5 wt% to $0.29 \times 10^{-18}\,\mathrm{cm}^2/\mathrm{s}$ at 20 wt% in flight conditions) confirms the topological predictions. Higher filler concentrations lead to a highly tortuous and tight percolative network that progressively chokes the transport phenomena, confirming the transition toward an absolute barrier.

This quantitative agreement confirms that the parameters extracted via the mass-based numerical fitting are not merely mathematical artifacts, but represent real physical changes in the material's transport architecture.

6.9.2 Constitutive Calibration of the Percolation Law

As anticipated, the final validation of the physical framework involves correlating the extracted diffusivity values (D_{eff}) with the POSS filler loading (P). To this end, the back-calculated diffusivity values were plotted against the POSS volume fraction, and a non-linear regression analysis was performed using the exponential percolation law derived previously (Eq. 6.39).

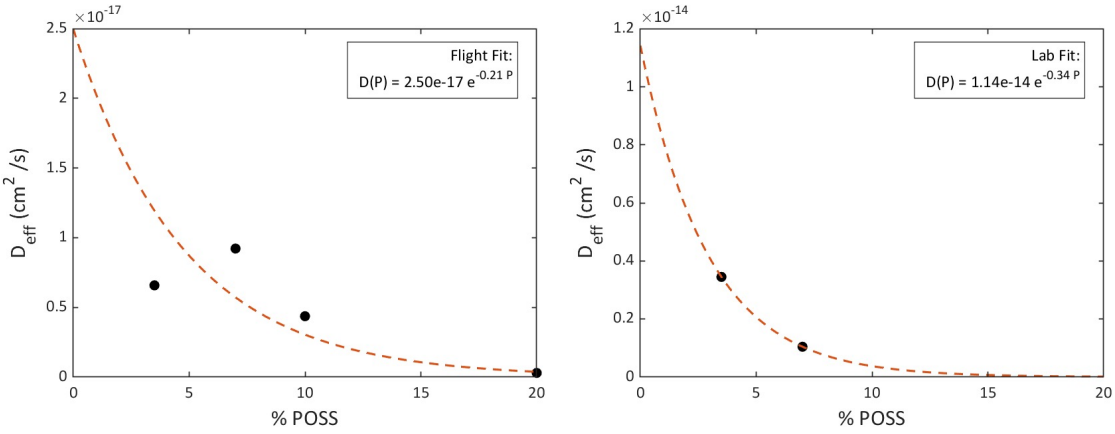

(a) Flight Regime **(b)** Lab Regime

Figure 6.5: Validation of the percolation law. The experimentally extracted diffusivity values (symbols) align with the theoretical percolation curve (solid line). The sharp decay in diffusivity confirms that the protection mechanism is driven by the geometric closure of diffusion paths (tortuosity) rather than chemical kinetics alone.

Figure 6.5 illustrates the agreement between the extracted data points and the theoretical percolation curve. The regression analysis yielded the constitutive parameters summarized below in Table 6.2.

Table 6.2: Constitutive parameters of the percolation law calibrated on the extracted diffusivity data.

Parameter	Flight Regime (LEO)	Lab Regime (High Flux)
D_0 [cm^2/s]	2.50×10^{-17}	1.14×10^{-14}
Critical Exponent (β) [–]	0.21	0.34

These calibrated parameters constitute the *"genetic code"* of the material's durability. They are now used to power the predictive algorithm, allowing for the simulation of any arbitrary filler loading without further experimental calibration.

6.9.3 Validation of Model Predictions

As a first verification step, the code was run to reconstruct the mass loss curves of the primary experimental campaigns (MISSE-6 and the 2012 high-flux ground simulation). It is important to note that the curves presented in this preliminary phase are generated continuously purely from the POSS volume fraction via the generalized percolation law, rather than through individual point-by-point numerical fitting. While this demonstrates the excellent mathematical continuity of the framework, it represents a *self-consistency check* rather than a pure prediction, given that the underlying constitutive parameters (D_0, β) were calibrated on this very dataset. Figure 6.6 compares the model reconstructions with the primary experimental data.

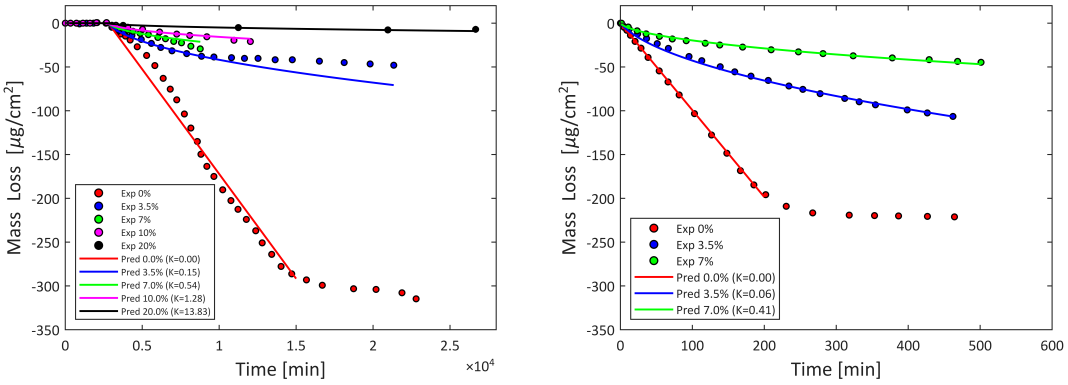

(a) Flight data (MISSE-6). **(b) Laboratory data.**

Figure 6.6: Self-consistency reconstruction. Comparison between the percolation-based model output (solid lines) and the primary experimental data (symbols) used for calibration. The model smoothly captures the erosion kinetics across all filler loadings without requiring local parameter tuning.

The expected agreement between the continuous percolation framework and the experimental reality confirms that the algorithm reliably translates the topological state of the material into the correct mass-loss kinetics. Furthermore, it is important to observe a distinct difference in the data quality between the two environments. While the ground laboratory tests were performed under strictly controlled steady-state conditions, resulting in smooth, monotonic mass loss curves with high correlation coefficients, the in-flight data (MISSE-6) exhibits noticeable stochastic deviations. These fluctuations are not attributable to model inaccuracies but are intrinsic consequences of the variable LEO environment. Unlike the constant flux of the ground source, the orbital exposure, as explained in detail in Chapter 5 is subject to:

- *Thermal Cycling:* The day-night orbital transitions induce periodic thermal expansion and contraction, potentially triggering micro-cracking in the brittle silica layer.

- *Flux Variability:* The atomic oxygen fluence varies with solar activity and orbital drag, unlike the fixed flux of the calibration facility.

- *Wake Effects:* Minor oscillations in the spacecraft attitude can temporarily alter the incidence angle.

Consequently, the deviations observed in the flight data (Figure 6.6a) represent environmental noise rather than constitutive behavior. The proposed model successfully captures the *macroscopic mean trend* of the erosion process, effectively filtering out these short-term stochastic perturbations.

While successfully reconstructing the training dataset is a fundamental prerequisite, the true benchmark of an engineering predictive framework lies in its capability to forecast material behavior under novel, untested conditions. To evaluate this absolute transferability, the computational tool was deployed to simulate a completely independent high-flux ground-testing campaign reported by Qian et al. [184] in 2016.

Crucially, the algorithm was fed exclusively with the boundary conditions of the new facility and the physical properties of the materials, while the topological "genetic code" governing the passivation (the D_0 and β parameters extracted from the 2012 lab data) was kept strictly locked. Figure 6.7 overlays the independent 2016 experimental data points onto the purely forward-predictive curves generated by the model.

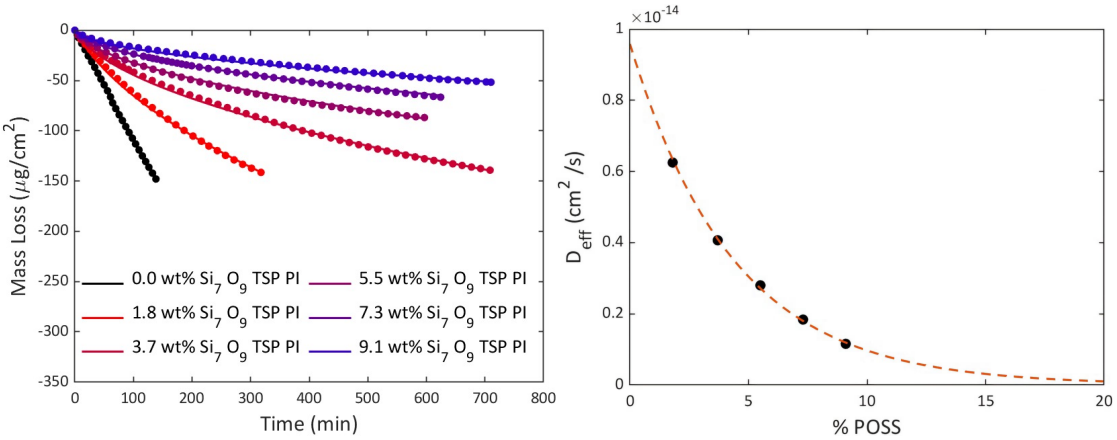

(a) Erosion kinetics. **(b) Transport properties validation.**

Figure 6.7: Blind validation against independent ground tests. Comparison between the forward-predictive model output and the independent experimental dataset [184]. (a) Macroscopic mass loss reconstruction without localized parameter tuning. (b) The effective diffusivity values extracted from the independent 2016 campaign perfectly align with the theoretical percolation curve defined by the 2012 calibration.

This absolute predictive capability is further corroborated by analyzing the underlying physical transport properties. As shown in Figure 6.7b, the effective diffusivities extracted *a posteriori* from the independent 2016 experimental campaign align perfectly with the theoretical percolation curve generated using the constitutive parameters (D_0, β) calibrated on the 2012 dataset.

The excellent agreement between the numerical predictions and the external dataset, both in terms of macroscopic mass loss and internal transport kinetics—definitively validates the theoretical framework. It demonstrates that the topological parameters extracted via the percolation law successfully capture the intrinsic physical mechanisms of the silica barrier formation, rather than being mere empirical constants tied to a single calibration setup. By accurately coupling the material's invariant internal topology with the specific environmental boundary conditions of the new facility, the model reliably forecasts the erosion behavior. This confirms the framework as a highly robust, predictive engineering tool, capable of anticipating material performance across different aerospace environments.

6.9.4 Evolution of the Silica Passivation Layer Thickness

A critical aspect of the model validation is translating the gravimetric mass loss into a physical dimension representing the protective barrier. Since the mass loss values are normalized per unit area, it is possible to evaluate the instantaneous thickness of the silica layer (SiO_2) formed during the oxidation process. Based on the stoichiometric conservation of silicon atoms derived in the governing equations, the time-evolution of the passivation layer thickness $h(t)$ is given by:

$$h(t) = S \cdot P \cdot |m_{loss}(t)| \tag{6.45}$$

Where:

- S is the specific conversion factor relating the volume of oxide formed to the mass of polymer eroded.
- P is the POSS mass fraction (loading).
- $|m_{loss}(t)|$ is the absolute value of the cumulative mass loss per unit area.

Applying this relationship to the experimental dataset at the end of the exposure period, we obtain the characteristic thickness values reported in Table 6.3.

POSS Loading [**wt%**]	**Total Mass Loss** [$\mu g/cm^2$]	**Final Layer Thickness** h [**nm**]
3.5	-78.37	**172.41**
7.0	-42.70	**93.94**
10.0	-28.11	**61.85**
20.0	-8.69	**19.13**

Table 6.3: Calculated thickness of the passivation layer for different POSS loadings at the end of exposure for the fligth test.

Consistent with the inverse correlation discussed previously, the 3.5 wt% sample (blue line) exhibits the steepest growth and reaches the highest final value. In contrast, the 20 wt% sample (black line) stabilizes almost immediately at a very low thickness value, confirming that a high density of nucleation sites allows for the rapid formation of a thin, yet highly efficient, protective shield.

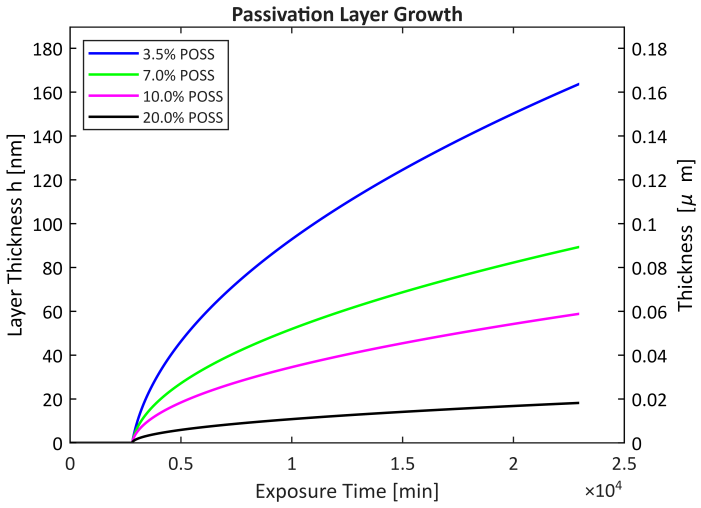

Figure 6.8: Time evolution of the calculated silica passivation layer thickness $h(t)$. The asymptotic behavior confirms the diffusion-limited nature of the protective mechanism, while the vertical offset between curves highlights that lower POSS loadings require a thicker interaction zone to achieve effective passivation.

The analysis of these results and the growth curves reveals three fundamental physical behaviors governing the protection mechanism:

1. *Self-Limiting Kinetics (Diffusion Control):* The growth profile of $h(t)$ is not linear but exhibits a parabolic-like trajectory. This confirms that the process is *diffusion-limited*: as the silica layer forms, it progressively hinders the permeation of atomic oxygen to the underlying polymer. The thicker the layer becomes, the slower the subsequent growth rate, effectively stabilizing the material over time.

2. *Inverse Correlation (Scavenging Efficiency):* A counter-intuitive but physically consistent phenomenon is observed: *lower POSS loadings result in thicker passivation layers.* For the 3.5 wt% sample, a significant amount of the organic matrix must be eroded to "scavenge" and accumulate enough silicon atoms to form a continuous shield, resulting in a thick layer (≈ 172 nm) and high mass loss. Conversely, higher loadings provide a denser reservoir of silicon.

3. *Efficiency at High Loadings:* As the POSS content increases (e.g., 20 wt%), the mean distance between inorganic cages decreases. Upon exposure, these cages rapidly coalesce to form a dense, protective barrier with minimal polymer consumption. Consequently, the 20% sample exhibits the highest erosion

resistance while forming the thinnest final oxide layer ($\approx 19\,\text{nm}$), demonstrating that a thinner, rapidly formed barrier is more efficient than a thicker one formed through extensive degradation.

6.9.5 Dynamic Transition of the Erosion Mechanism

To further elucidate the physical kinetics driving the erosion process, the model allows for the deconvolution of the total erosion resistance into its two constituent components. Recall that the governing differential equation implies a "resistance-in-series" model, where the total resistance to mass loss (R_{tot}) is the sum of the intrinsic chemical reaction resistance (R_{chem}) and the evolving diffusion barrier resistance (R_{diff}):

$$R_{tot}(t) = \underbrace{\frac{1}{R_0}}_{R_{chem}} + \underbrace{\frac{h(t)}{D_{\text{eff}}(P)}}_{R_{diff}} \tag{6.46}$$

Figure 6.9 presents the temporal evolution of these resistances (left panels) and the relative dominance of the erosion mechanism (right panels) for the simulated POSS loadings. The visualization adopts a color-coded scheme:

- *Red Region (Reaction Limited):* Represents the phase where the erosion is governed by the chemical reactivity of the polymer ($R_{chem} \gg R_{diff}$).

- *Green Region (Diffusion Limited):* Represents the phase where the silica barrier has formed, and the process is throttled by the oxygen transport through the oxide layer ($R_{diff} \gg R_{chem}$).

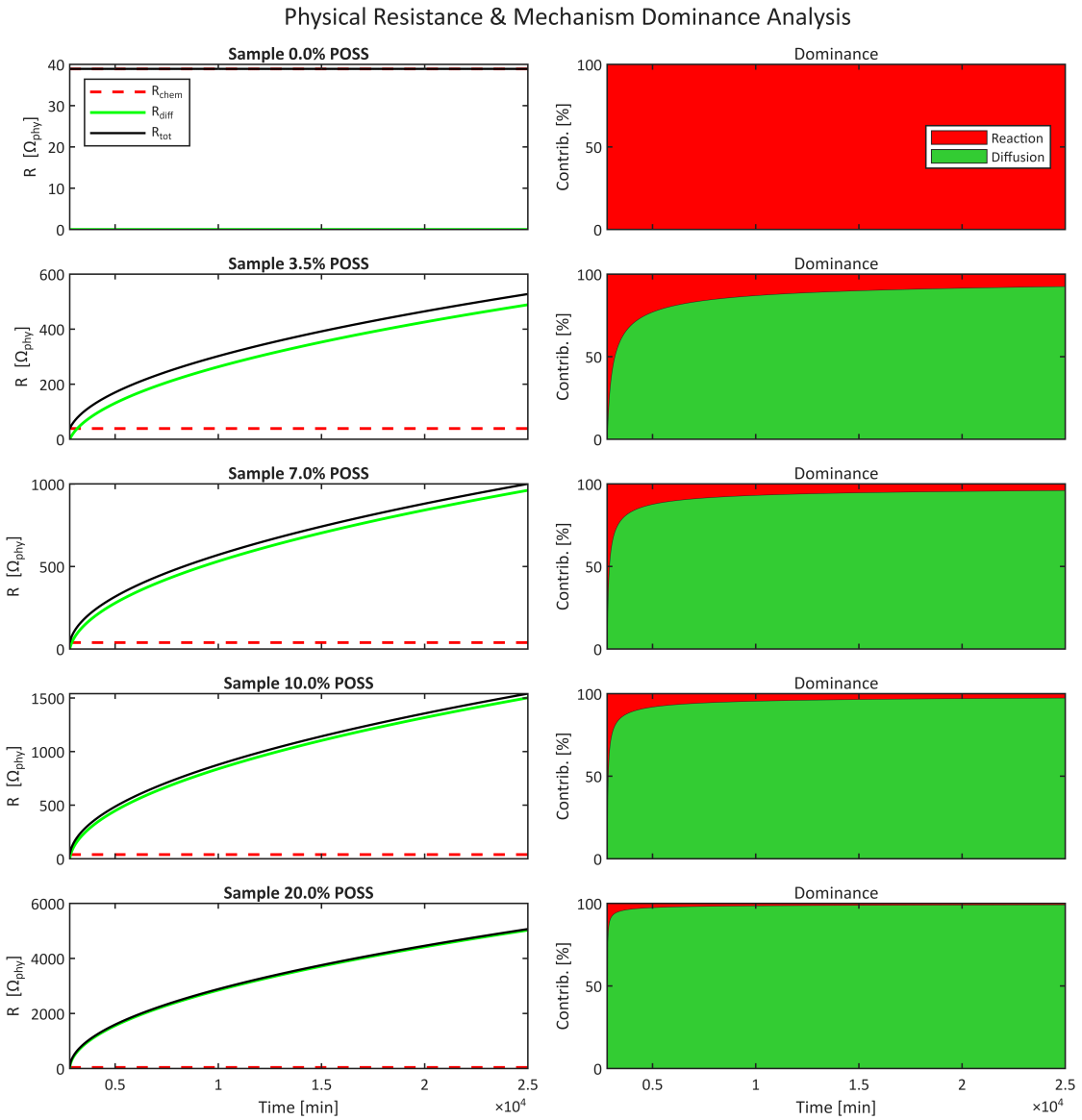

Figure 6.9: Evolution of the protection mechanism for varying POSS loadings. Left graphs show the breakdown of physical resistance (Red dashed: Chemical; Green solid: Diffusive; Black: Total). Right graphs show the percentage contribution of each mechanism, highlighting the transition from a reaction-controlled regime to a diffusion-controlled regime.

The graphical results highlight distinct behaviors depending on the filler content:

1. *Pristine Polyimide (0% POSS):* As expected, the control sample (top-left) exhibits a constant, purely resistive behavior dominated entirely by the chemical

reaction (Red Area $\approx 100\%$). Since no inorganic layer forms ($R_{diff} \approx 0$), the total resistance remains low and constant, resulting in the linear mass loss observed experimentally.

2. *Transition Phase (Low Loadings - 3.5%):* For the 3.5% sample (top-right), the process begins in the reaction-limited regime. However, as the silica network nucleates, the diffusion resistance (green line) progressively increases. The crossover point, where the diffusion resistance exceeds the reaction resistance, marks the effective onset of passivation. The gradual expansion of the green area explains the slow bending of the mass loss curve observed in the previous section.

3. *Instant Passivation (High Loadings - 10% & 20%):* At higher loadings (bottom panels), the transition is abrupt. The high density of POSS cages leads to a rapid coalescence of the barrier. Consequently, the diffusion resistance (R_{diff}) skyrockets almost immediately, rendering the chemical reaction resistance negligible within the first few minutes of exposure. This confirms that for high-loading nanocomposites, the material stability is almost entirely determined by the transport properties of the silica layer rather than the chemical nature of the polymer matrix.

6.10 Concluding Remarks and Model Applicability

This Part of the thesis presented a comprehensive study on the atomic oxygen erosion resistance of POSS-polyimide nanocomposites, combining experimental testing in both ground laboratory and LEO/VLEO environments with a predictive physics-based numerical model. The experimental campaign confirmed that the inclusion of POSS induces a "self-passivation" mechanism, where the oxidative degradation of the organic cage leads to the formation of a coherent silica-rich barrier.

6.10.1 Predictive Capabilities and Engineering Value

A central outcome of this work is the development of a predictive model based on *percolation theory* and *free volume* kinetics. While the derivation of the constitutive parameters (β, D_0, K) requires an initial experimental calibration on a representative dataset, the proposed framework offers substantial advantages over a purely experimental "trial-and-error" approach. Once calibrated, the model transcends simple data fitting to become a powerful *design optimization tool*, offering three critical engineering capabilities:

1. *Virtual Prototyping (Interpolation):* The constitutive law allows for the simulation of intermediate filler fractions (e.g., 5.2 wt%) that were not physically synthesized. This enables the identification of the optimal filler loading, balancing erosion resistance with mechanical constraints (e.g., embrittlement), without the cost and time associated with manufacturing and testing every possible formulation.

2. *Predictive Capability and Chemo-Mechanical Baseline:* The framework effectively transitions from an initial calibrative step to a fully predictive tool: a single calibration performed on ground laboratory data is sufficient to accurately forecast the degradation response of the same class of materials under different exposure conditions. This predictive capability establishes a robust baseline for future model evolutions, ultimately aiming to forecast the in-orbit (LEO) behavior of these nanocomposites relying solely on accelerated ground testing. Furthermore, from a computational modeling perspective, successfully characterizing the environmentally-induced degradation is a fundamental stepping stone toward developing a comprehensive chemo-mechanical constitutive framework, capable of integrating the synergistic effects of simultaneous mechanical and thermal stress conditions into the predictive analysis.

3. *Temporal Extrapolation (End-of-Life Prediction):* By capturing the physics of barrier saturation (the transition from reaction-controlled to diffusion-controlled kinetics), the model can project long-term erosion trends. This capability allows for the estimation of the material's End-of-Life state after typical mission durations relying only on short-term exposure data, significantly accelerating the material qualification process.

In conclusion, this work demonstrates that while experimental characterization remains fundamental, integrating it with a percolation-based predictive model transforms the testing process from a descriptive analysis into a predictive engineering methodology for the design of next-generation space materials.

Chapter 7

General Conclusions

7.1 Synthesis of the Research: From Bulk to Surface Degradation

The primary objective of this master's thesis was to advance the predictive modeling of polymer degradation by overcoming the limitations of classical kinetic theories and phenomenological/empirical models. Standard engineering approaches typically rely on simplified assumptions, such as the Arrhenius law for thermal aging or linear erosion rates for erosion, which fail to capture the complex, non-linear dependencies observed in nanometric and nanostructured materials. This research addressed this gap through a two-fold investigation, distinguishing between bulk chemical evolution (Part I) and surface physical recession (Part II). Although applied to different environmental contexts, both parts share a common methodological philosophy: the transition from empirical curve-fitting to physics-based semi-analytical modeling. Part I focused on the terrestrial photo-oxidation of LDPE nanometric films. Here, the investigation challenged both the classic DLO theory and the classic homogeneized diffusion ones. By analyzing the anomalous thickness dependency of degradation in the nanometric regime, we demonstrated that the limiting factor is not the ingress of reactants (oxygen), but the egress of reaction products. This led to the formulation of the Volatile Trapping Hypothesis, proving that the local accumulation of byproducts creates a thermodynamic inhibition that governs the macroscopic material lifespan. Crucially, this chemical insight was not left as an isolated kinetic study; it served as the state variable driving a novel chemo-mechanical constitutive model. Computationally, this was achieved by developing a fully coupled multiphysics framework. The transient spatial distribution of the oxidative degree was explicitly mapped onto the mechanical domain to degrade the local fracture toughness of the material. By integrating this oxidation-dependent degradation function into a phase-field fracture model, we successfully bridged the

gap between microscopic molecular scission and the macroscopic embrittlement and failure observed in engineering components. Part II shifted the focus to the Space Environment (LEO/VLEO), specifically addressing the atomic oxygen erosion of POSS-nanocomposites. Moving beyond linear, empirical mass-loss models, we established a predictive framework based on geometric percolation theory. This model successfully captures the self-passivation mechanism of POSS-filled polymers, describing how the dynamic accumulation of an inorganic silica network creates a physical barrier that arrests surface recession. In conclusion, this thesis establishes that true predictive capability in polymer degradation cannot rely solely on phenomenological observations. Accurate durability forecasting requires coupling fundamental chemical kinetics with physical transport mechanisms, be it the transient diffusion of oxidants through a stressed bulk polymer or the topological percolation of an inorganic barrier during active surface erosion. By bridging these microscopic physics with macroscopic structural responses, this research provides a generalized framework for the design of next-generation, degradation-resistant engineering materials tailored for extreme aerospace environments.

7.2 Main Conclusions on Photo-Oxidative Degradation

The investigation conducted on Low-Density Polyethylene films provided new insights into the kinetics of degradation in geometrically confined systems. The key findings can be summarized as follows:

- *Failure of Standard DLO Theory:* It is demonstrated that in ultra-thin films ($<$ 200 nm), oxygen saturation is instantaneous and homogeneous. Consequently, the observed thickness dependency cannot be attributed to oxygen starvation, as postulated by classical Diffusion-Limited Oxidation models.
- *Validation of the Volatile Trapping Hypothesis:* The proposed model successfully linked the degradation rate to the local concentration of volatile byproducts. We proved that in thicker films (or deeper layers), the difficult egress of these species creates a local thermodynamic inhibition (Le Chatelier effect) that slows down the forward reaction.
- *Predictive Capability:* The semi-analytical model, calibrated on experimental mass loss data, successfully reproduced the non-linear thickness effect, identifying a specific set of physical parameters that govern the competition between chemical generation and diffusive removal.
- *Constitutive Modeling and Embrittlement:* We successfully implemented a thermodynamically consistent chemo-mechanical framework that couples the aging

state to the material's free energy. By adopting a viscoelastic model combined with a phase-field approach (AT1), the simulation accurately reproduced the experimentally observed transition from a ductile, necking-dominated failure in virgin samples to a brittle, elastic-fracture behavior in aged ones, without relying on ad-hoc decay functions calibrated for each aging state.

7.3 Main Conclusions on Atomic Oxygen Erosion

The research on AO interaction with POSS-based nanocomposites led to the development of a robust tool for lifetime prediction in LEO. The principal conclusions are:

- *Limitations of Linear Models:* We confirmed that while pure polymers exhibit linear erosion, hybrid nanocomposites follow a non-linear asymptotic behavior that cannot be described by a constant Erosion Yield (E_y).
- *The Percolation Mechanism:* The developed mathematical framework effectively describes the formation of the protective silica layer as a geometric percolation problem. The model demonstrates that surface passivation occurs only when the accumulation of inorganic fillers reaches a critical surface density, forming a continuous network.
- *Design Optimization:* The model provides a direct correlation between the initial filler loading (P) and the total eroded depth. This allows for the optimization of material formulation, minimizing the filler content required to achieve passivation within a specific mission timeframe.

7.4 Future Perspectives

While this thesis establishes a solid foundation for modeling degradation kinetics and provides a generalized framework for the design of next-generation materials tailored for extreme aerospace environments, several avenues for future research remain open to further bridge the gap between material science and structural engineering:

- *Synergistic Degradation Modeling:* The current frameworks successfully isolate and mathematically describe UV and AO degradation mechanisms. However, the LEO environment presents a highly coupled stress scenario. A comprehensive model is required to investigate the synergistic effects, where UV radiation embrittles the bulk material and generates surface radicals, potentially altering the AO erosion yield or compromising the formation and stability of the silica passivation layer.

- *Advanced Chemo-Mechanical Coupling for Passivating Systems:* While this work successfully formulated and implemented a coupled chemo-mechanical damage model for LDPE undergoing photo-oxidation, future efforts should extend this multiphysics approach to nanocomposites and self-passivating systems. Specifically, the scalar damage variables governing erosion (z) and percolation could be integrated into a continuum mechanics framework to study the structural integrity of the SiO_2 glassy layer. Predicting stress-induced or thermal-cycling-induced micro-cracking of this brittle layer is crucial, as fracture would re-expose the pristine underlying polymer to AO. Furthermore, this generalized coupling could be readily adapted to evaluate other high-performance aerospace polymers that share similar passivation physics, such as Novastrat® polyimides.
- *Extension to 3D Complex Geometries:* Both numerical models currently operate on 1D domains (representing film thickness or surface recession). Transitioning the numerical implementation to a fully coupled 3D Finite Element scheme would allow for the simulation of realistic, complex spacecraft components. This geometric expansion is essential to account for localized stress concentrations, 3D diffusion pathways, and directional environmental boundary conditions, such as dynamic orbital shadowing and non-uniform solar irradiation.

Bibliography

[1] Milan Bukvić, Saša Milojević, Sandra Gajević, Momčilo Đorđević, and Blaža Stojanović. «Production technologies and application of polymer composites in engineering: a review». In: *Polymers* 17.16 (2025), p. 2187 (cit. on p. 1).

[2] LC Hollaway. «A review of the present and future utilisation of FRP composites in the civil infrastructure with reference to their important in-service properties». In: *Construction and building materials* 24.12 (2010), pp. 2419–2445 (cit. on p. 1).

[3] Klaus Friedrich and Abdulhakim A Almajid. «Manufacturing aspects of advanced polymer composites for automotive applications». In: *Applied Composite Materials* 20.2 (2013), pp. 107–128 (cit. on p. 1).

[4] Manfred F Maitz. «Applications of synthetic polymers in clinical medicine». In: *Biosurface and biotribology* 1.3 (2015), pp. 161–176 (cit. on p. 1).

[5] Dipen Kumar Rajak, Durgesh D Pagar, Pradeep L Menezes, and Emanoil Linul. «Fiber-reinforced polymer composites: Manufacturing, properties, and applications». In: *Polymers* 11.10 (2019), p. 1667 (cit. on p. 1).

[6] Peter JT Morris. *The American synthetic rubber research program*. University of Pennsylvania Press, 2017 (cit. on p. 1).

[7] Jeffrey L Meikle. *American plastic: a cultural history*. Rutgers University Press, 1995 (cit. on p. 1).

[8] Amar K Mohanty, Singaravelu Vivekanandhan, Jean-Mathieu Pin, and Manjusri Misra. «Composites from renewable and sustainable resources: Challenges and innovations». In: *Science* 362.6414 (2018), pp. 536–542 (cit. on p. 2).

[9] Jin Zhang, Venkata S Chevali, Hao Wang, and Chun-Hui Wang. «Current status of carbon fibre and carbon fibre composites recycling». In: *Composites Part B: Engineering* 193 (2020), p. 108053 (cit. on p. 2).

[10] Rittin Abraham Kurien, D Philip Selvaraj, M Sekar, and Chacko Preno Koshy. «Green composite materials for green technology in the automotive industry». In: *IOP conference series: materials science and engineering*. Vol. 872. 1. IOP Publishing. 2020, p. 012064 (cit. on p. 2).

[11] Soraia Pimenta and Silvestre T Pinho. «Recycling carbon fibre reinforced polymers for structural applications: Technology review and market outlook». In: *Waste management* 31.2 (2011), pp. 378–392 (cit. on p. 2).

[12] Myer Kutz. *Handbook of environmental degradation of materials*. William Andrew, 2018 (cit. on p. 2).

[13] Philip A Schweitzer et al. *Fundamentals of corrosion: mechanisms, causes, and preventative methods*. CRC press, 2009 (cit. on p. 2).

[14] Donald R Paul and Lioyd M Robeson. «Polymer nanotechnology: nanocomposites». In: *Polymer* 49.15 (2008), pp. 3187–3204 (cit. on pp. 2, 5).

[15] Suprakas Sinha Ray and Masami Okamoto. «Polymer/layered silicate nanocomposites: a review from preparation to processing». In: *Progress in polymer science* 28.11 (2003), pp. 1539–1641 (cit. on p. 2).

[16] Fengge Gao. *Advances in polymer nanocomposites: types and applications*. Elsevier, 2012 (cit. on p. 2).

[17] Trevor William Clyne and Derek Hull. *An introduction to composite materials*. Cambridge university press, 2019 (cit. on p. 3).

[18] PD Mangalgiri. «Composite materials for aerospace applications». In: *Bulletin of Materials Science* 22.3 (1999), pp. 657–664 (cit. on p. 3).

[19] Adrian P Mouritz. *Introduction to aerospace materials*. Elsevier, 2012 (cit. on p. 3).

[20] Pankar K Mallick. *Fiber-reinforced composites: materials, manufacturing, and design*. CRC press, 2007 (cit. on p. 3).

[21] Jean-Pierre Pascault and Roberto JJ Williams. «Thermosetting polymers». In: *Handbook of polymer synthesis, characterization, and processing* (2013), pp. 519–533 (cit. on p. 3).

[22] Flake C Campbell Jr. *Manufacturing processes for advanced composites*. elsevier, 2003 (cit. on p. 3).

[23] Stephen J Pickering. «Recycling technologies for thermoset composite materials—current status». In: *Composites Part A: applied science and manufacturing* 37.8 (2006), pp. 1206–1215 (cit. on p. 3).

[24] Norman Gerard McCrum, C Paul Buckley, and Clive B Bucknall. *Principles of polymer engineering*. Oxford University Press, 1997 (cit. on p. 4).

[25] Klaus Friedrich and Alois K Schlarb. *Tribology of polymeric nanocomposites: friction and wear of bulk materials and coatings*. Vol. 55. Elsevier, 2011 (cit. on p. 4).

[26] Paul M Hergenrother. «The use, design, synthesis, and properties of high performance/high temperature polymers: an overview». In: *High Performance Polymers* 15.1 (2003), pp. 3–45 (cit. on pp. 4, 6).

[27] Johannes Karl Fink. *High performance polymers*. William Andrew, 2014 (cit. on p. 4).

[28] Derek Hull. «An Introduction to Composite Materials». In: *Cambridge University Press* 198 (1996), p. l (cit. on p. 4).

[29] William D Callister Jr and David G Rethwisch. *Materials science and engineering: an introduction*. John wiley & sons, 2020 (cit. on p. 4).

[30] Jeffrey Jordan, Karl I Jacob, Rina Tannenbaum, Mohammed A Sharaf, and Iwona Jasiuk. «Experimental trends in polymer nanocomposites—a review». In: *Materials science and engineering: A* 393.1-2 (2005), pp. 1–11 (cit. on p. 4).

[31] Wolfram Schnabel. *Polymer degradation: principles and practical applications*. Walter de Gruyter GmbH & Co KG, 1981 (cit. on p. 5).

[32] Dorel Feldman and Alla Barbalata. *Synthetic polymers: technology, properties, applications*. Springer Science & Business Media, 1996 (cit. on p. 5).

[33] Hans-Henning Kausch. *Polymer fracture*. Vol. 2. Springer Science & Business Media, 2012 (cit. on pp. 5, 7).

[34] Krzysztof Pielichowski, James Njuguna, and Tomasz M Majka. *Thermal degradation of polymeric materials*. Elsevier, 2022 (cit. on p. 5).

[35] Sudip Ray and Ralph P Cooney. «Thermal degradation of polymer and polymer composites». In: *Handbook of environmental degradation of materials*. Elsevier, 2018, pp. 185–206 (cit. on p. 5).

[36] David C Wright. *Environmental stress cracking of plastics*. iSmithers Rapra Publishing, 1996 (cit. on p. 6).

[37] Bronwyn Laycock, Melissa Nikolić, John M Colwell, Emilie Gauthier, Peter Halley, Steven Bottle, and Graeme George. «Lifetime prediction of biodegradable polymers». In: *Progress in Polymer Science* 71 (2017), pp. 144–189 (cit. on p. 6).

[38] Charles M Hansen. *Hansen solubility parameters: a user's handbook*. CRC press, 2007 (cit. on p. 6).

[39] Philip A Schweitzer. *Corrosion of polymers and elastomers*. CRC Press, 2006 (cit. on p. 6).

[40] Nathalie Lucas, Christian Bienaime, Christian Belloy, Michele Queneudec, Francoise Silvestre, and Jose-Edmundo Nava-Saucedo. «Polymer biodegradation: Mechanisms and estimation techniques–A review». In: *Chemosphere* 73.4 (2008), pp. 429–442 (cit. on p. 6).

[41] Jan F Rabek. *Photodegradation of polymers: physical characteristics and applications*. Springer Science & Business Media, 2012 (cit. on pp. 7, 37).

[42] Mathew C Celina. «Review of polymer oxidation and its relationship with materials performance and lifetime prediction». In: *Polymer Degradation and Stability* 98.12 (2013), pp. 2419–2429 (cit. on pp. 8, 38, 55).

[43] Kenneth T Gillen and Roger L Clough. «Time-temperature-dose rate superposition: a methodology for extrapolating accelerated radiation aging data to low dose rate conditions». In: *Polymer Degradation and Stability* 24.2 (1989), pp. 137–168 (cit. on p. 8).

[44] Gerhard A Holzapfel. *Nonlinear solid mechanics: a continuum approach for engineering science*. 2002 (cit. on p. 13).

[45] Morton E Gurtin, Eliot Fried, and Lallit Anand. *The mechanics and thermodynamics of continua*. Cambridge university press, 2010 (cit. on pp. 13, 55).

[46] Michael J. Borden, Thomas J.R. Hughes, Chad M. Landis, Amin Anvari, and Isaac J. Lee. «A phase-field formulation for fracture in ductile materials: Finite deformation balance law derivation, plastic degradation, and stress triaxiality effects». In: *Computer Methods in Applied Mechanics and Engineering* 312 (2016). Phase Field Approaches to Fracture, pp. 130–166. ISSN: 0045-7825. DOI: https://doi.org/10.1016/j.cma.2016.09.005. URL: https://www.sciencedirect.com/science/article/pii/S0045782516311069 (cit. on pp. 13, 16).

[47] Christian Miehe and Lisa-Marie Schänzel. «Phase field modeling of fracture in rubbery polymers. Part I: Finite elasticity coupled with brittle failure». In: *Journal of the Mechanics and Physics of Solids* 65 (2014), pp. 93–113. ISSN: 0022-5096. DOI: https://doi.org/10.1016/j.jmps.2013.06.007. URL: https://www.sciencedirect.com/science/article/pii/S0022509613001191 (cit. on p. 13).

[48] G.A. Francfort and J.-J. Marigo. «Revisiting brittle fracture as an energy minimization problem». In: *Journal of the Mechanics and Physics of Solids* 46.8 (1998), pp. 1319–1342. ISSN: 0022-5096. DOI: https://doi.org/10.1016/S0022-5096(98)00034-9. URL: https://www.sciencedirect.com/science/article/pii/S0022509698000349 (cit. on p. 13).

[49] Aimane Najmeddine and Maryam Shakiba. «Physics and chemistry-based phase-field constitutive framework for thermo-chemically aged elastomer». In: *International Journal of Mechanical Sciences* 262 (2024), p. 108721 (cit. on pp. 16, 42, 55).

[50] Tushar Kanti Mandal, Abhinav Gupta, Vinh Phu Nguyen, Rajib Chowdhury, and Alban de Vaucorbeil. «A length scale insensitive phase field model for brittle fracture of hyperelastic solids». In: *Engineering Fracture Mechanics* 236 (2020), p. 107196 (cit. on pp. 17, 57).

[51] Bernard D Coleman and Walter Noll. «The thermodynamics of elastic materials with heat conduction and viscosity». In: *The foundations of mechanics and thermodynamics: Selected papers*. Springer, 1974, pp. 145–156 (cit. on p. 18).

[52] Morton E Gurtin. *An introduction to continuum mechanics*. Vol. 158. Academic press, 1982 (cit. on p. 18).

[53] Richard M Christensen. *Theory of viscoelasticity*. Courier Corporation, 2013 (cit. on p. 19).

[54] John D Ferry and Henry S Myers. «Viscoelastic properties of polymers». In: *Journal of The Electrochemical Society* 108.7 (1961), p. 142C (cit. on p. 20).

[55] JL Bolland and Geoffrey Gee. «Kinetic studies in the chemistry of rubber and related materials. III. Thermochemistry and mechanisms of olefin oxidation». In: *Transactions of the Faraday Society* 42 (1946), pp. 244–252 (cit. on p. 31).

[56] JL Bolland and Geoffrey Gee. «Kinetic Studies in the Chemistry of Rubber and Related Materials. III. Thermochemistry and Mechanisms of Olefin Oxidation». In: *Rubber Chemistry and Technology* 20.3 (1947), pp. 617–626 (cit. on p. 31).

[57] Andrew Fairbrother, Hsiang-Chun Hsueh, Jae Hyun Kim, Deborah Jacobs, Lakesha Perry, David Goodwin, Christopher White, Stephanie Watson, and Li-Piin Sung. «Temperature and light intensity effects on photodegradation of high-density polyethylene». In: *Polymer degradation and stability* 165 (2019), pp. 153–160 (cit. on p. 31).

[58] Graeme A George and Mathew Celina. «Homogeneous and heterogeneous oxidation of polypropylene». In: *Handbook of polymer degradation*. CRC Press, 2000, pp. 299–302 (cit. on pp. 31, 38).

[59] Pieter Gijsman, Guido Meijers, and Giacomo Vitarelli. «Comparison of the UV-degradation chemistry of polypropylene, polyethylene, polyamide 6 and polybutylene terephthalate». In: *Polymer Degradation and Stability* 65.3 (1999), pp. 433–441 (cit. on p. 31).

[60] Ana K Rodriguez, Bilal Mansoor, Georges Ayoub, Xavier Colin, and Amine A Benzerga. «Effect of UV-aging on the mechanical and fracture behavior of low density polyethylene». In: *Polymer Degradation and Stability* 180 (2020), p. 109185 (cit. on pp. 32, 33).

[61] Saleh A Jabarin and Elizabeth A Lofgren. «Photooxidative effects on properties and structure of high-density polyethylene». In: *Journal of Applied Polymer Science* 53.4 (1994), pp. 411–423 (cit. on p. 34).

[62] MS Rabello and JR White. «Crystallization and melting behaviour of photodegraded polypropylene—I. Chemi-crystallization». In: *Polymer* 38.26 (1997), pp. 6379–6387 (cit. on p. 34).

[63] Aimane Najmeddine, Zhen Xu, Gehui Liu, Zacary L. Croft, Guoliang Liu, Alan R. Esker, and Maryam Shakiba. «Physics and chemistry-based constitutive modeling of photo-oxidative aging in semi-crystalline polymers». In: *International Journal of Solids and Structures* 239-240 (2022), p. 111427. ISSN: 0020-7683. DOI: https://doi.org/10.1016/j.ijsolstr.2022.111427. URL: https://www.sciencedirect.com/science/article/pii/S0020768322000051 (cit. on pp. 34, 38–40, 43, 51, 52, 55, 66–68).

[64] A. Omazic, G. Oreski, M. Halwachs, G.C. Eder, C. Hirschl, L. Neumaier, G. Pinter, and M. Erceg. «Relation between degradation of polymeric components in crystalline silicon PV module and climatic conditions: A literature review». In: *Solar Energy Materials and Solar Cells* 192 (2019), pp. 123–133. ISSN: 0927-0248. DOI: https://doi.org/10.1016/j.solmat.2018.12.027. URL: https://www.sciencedirect.com/science/article/pii/S0927024818305956 (cit. on p. 36).

[65] E. Espí, A. Salmerón, A. Fontecha, Y. García, and A. I. Real. «PLastic Films for Agricultural Applications». In: *Journal of Plastic Film & Sheeting* 22.2 (2006), pp. 85–102. DOI: 10.1177/8756087906064220. eprint: https://doi.org/10.1177/8756087906064220. URL: https://doi.org/10.1177/8756087906064220 (cit. on p. 36).

[66] P.A. Dilara and D. Briassoulis. «Degradation and Stabilization of Low-density Polyethylene Films used as Greenhouse Covering Materials». In: *Journal of Agricultural Engineering Research* 76.4 (2000), pp. 309–321. ISSN: 0021-8634. DOI: https://doi.org/10.1006/jaer.1999.0513. URL: https://www.sciencedirect.com/science/article/pii/S0021863499905139 (cit. on p. 36).

[67] Sixi Zha, Hui-qing Lan, and Hui Huang. «Review on lifetime predictions of polyethylene pipes: Limitations and trends». In: *International Journal of Pressure Vessels and Piping* 198 (2022), p. 104663 (cit. on p. 36).

[68] Lieke de Rouw. «A Systematic Review on the Materials used in Medical Plastic Packages and the Influence of Recycling on the Mechanical Properties of Plastics». In: () (cit. on p. 36).

[69] Giovanni Mazzanti. «Issues and Challenges for HVDC Extruded Cable Systems». In: *Energies* 14.15 (2021). ISSN: 1996-1073. DOI: 10.3390/en14154504. URL: https://www.mdpi.com/1996-1073/14/15/4504 (cit. on p. 36).

[70] George Chen, Miao Hao, Zhiqiang Xu, Alun Vaughan, Junzheng Cao, and Haitian Wang. «Review of high voltage direct current cables». In: *CSEE Journal of Power and Energy Systems* 1.2 (2015), pp. 9–21 (cit. on p. 36).

[71] Zhonglei Li and Boxue Du. «Polymeric insulation for high-voltage dc extruded cables: challenges and development directions». In: *IEEE Electrical Insulation Magazine* 34.6 (2018), pp. 30–43 (cit. on p. 36).

[72] Boyuan Liang, Rui Lan, Qian Zang, Zhen Liu, Lin Tian, Zhaochen Wang, and Guochang Li. «Influence of Thermal Aging on Dielectric Properties of High Voltage Cable Insulation Layer». In: *Coatings* 13.3 (2023). ISSN: 2079-6412. DOI: 10.3390/coatings13030527. URL: https://www.mdpi.com/2079-6412/13/3/527 (cit. on p. 36).

[73] Amir Masoud Pourrahimi, Claire Pitois, and Amirhossein Abbasi. «XLPE high voltage insulation; A link between DC conductivity and microstructure». In: *Polymer Testing* 131 (2024), p. 108330. ISSN: 0142-9418. DOI: https://doi.org/10.1016/j.polymertesting.2024.108330. URL: https://www.sciencedirect.com/science/article/pii/S0142941824000072 (cit. on p. 36).

[74] Pierangiola Bracco, Anuj Bellare, Alessandro Bistolfi, and Saverio Affatato. «Ultra-High Molecular Weight Polyethylene: Influence of the Chemical, Physical and Mechanical Properties on the Wear Behavior. A Review». In: *Materials* 10.7 (2017). ISSN: 1996-1944. DOI: 10.3390/ma10070791. URL: https://www.mdpi.com/1996-1944/10/7/791 (cit. on p. 36).

[75] BH Currier, DW Van Citters, JH Currier, and JP Collier. «In vivo oxidation in remelted highly cross-linked retrievals». In: *JBJS* 92.14 (2010), pp. 2409–2418 (cit. on pp. 37, 44).

[76] Keith K Wannomae, Shayan Bhattacharyya, Andrew Freiberg, Daniel Estok, William H Harris, and Orhun Muratoglu. «In vivo oxidation of retrieved cross-linked ultra–high-molecular-weight polyethylene acetabular components with residual free radicals». In: *The Journal of arthroplasty* 21.7 (2006), pp. 1005–1011 (cit. on p. 37).

[77] W.W Wright. «Polymers in aerospace applications». In: *Materials & Design* 12.4 (1991), pp. 222–227. ISSN: 0261-3069. DOI: https://doi.org/10.1016/0261-3069(91)90169-5. URL: https://www.sciencedirect.com/science/article/pii/0261306991901695 (cit. on pp. 37, 82, 83).

[78] Sheila A Thibeault, Catharine C Fay, Sharon E Lowther, Kevin D Earle, Godfrey Sauti, Jin Ho Kang, Cheol Park, and Amelia M McMullen. *Radiation Shielding Materials Containing Hydrogen, Boron, and Nitrogen: Systematic Computational and Experimental Study*. Tech. rep. 2012 (cit. on pp. 37, 83).

[79] Elisa Toto, Lucia Lambertini, Susanna Laurenzi, and Maria Gabriella Santonicola. «Recent Advances and Challenges in Polymer-Based Materials for Space Radiation Shielding». In: *Polymers* 16.3 (2024). ISSN: 2073-4360. DOI: 10.3390/polym16030382. URL: https://www.mdpi.com/2073-4360/16/3/382 (cit. on pp. 37, 83).

[80] Susanna Laurenzi, Gianluca de Zanet, and M. Gabriella Santonicola. «Numerical investigation of radiation shielding properties of polyethylene-based nanocomposite materials in different space environments». In: *Acta Astronautica* 170 (2020), pp. 530–538. ISSN: 0094-5765. DOI: 10.1016/j.actaastro.2020.02.027. URL: https://www.sciencedirect.com/science/article/pii/S0094576520300898 (cit. on pp. 37, 83).

[81] Bruno Fayolle, Emmanuel Richaud, Xavier Colin, and Jacques Verdu. «Degradation-induced embrittlement in semi-crystalline polymers having their amorphous phase in rubbery state». In: *Journal of materials science* 43.22 (2008), pp. 6999–7012 (cit. on p. 37).

[82] Yu-Chieh Hsu, Michael P Weir, Rowan W Truss, Christopher J Garvey, Timothy M Nicholson, and Peter J Halley. «A fundamental study on photo-oxidative degradation of linear low density polyethylene films at embrittlement». In: *Polymer* 53.12 (2012), pp. 2385–2393 (cit. on p. 37).

[83] Víctor H Rolón-Garrido, Matthias Kruse, and Manfred H Wagner. «Size exclusion chromatography of photo-oxidated LDPE by triple detection and its relation to rheological behavior». In: *Polymer Degradation and Stability* 111 (2015), pp. 46–54 (cit. on p. 37).

[84] Keven Alkhoury and Shawn A Chester. «A chemo-thermo-mechanically coupled theory of photo-reacting polymers: Application to modeling photo-degradation with irradiation-driven heat transfer». In: *Journal of the Mechanics and Physics of Solids* 197 (2025), p. 106050 (cit. on p. 37).

[85] Shabnam Konica and Trisha Sain. «A thermodynamically consistent chemo-mechanically coupled large deformation model for polymer oxidation». In: *Journal of the Mechanics and Physics of Solids* 137 (2020), p. 103858 (cit. on pp. 37, 55).

[86] Maryam Shakiba, Masoud K Darabi, and Rashid K Abu Al-Rub. «A thermodynamic framework for constitutive modeling of coupled moisture-mechanical induced damage in partially saturated viscous porous media». In: *Mechanics of Materials* 96 (2016), pp. 53–75 (cit. on p. 37).

[87] L Audouin, V Langlois, J Verdu, and JCM De Bruijn. «Role of oxygen diffusion in polymer ageing: kinetic and mechanical aspects». In: *Journal of Materials science* 29.3 (1994), pp. 569–583 (cit. on p. 38).

[88] JONATHAN Tireau, LAETITIA Van Schoors, K Benzarti, and X Colin. «Environmental ageing of carbon black-filled polyethylene sheaths employed in civil engineering». In: *J. Nanostruct. Polym. Nanocompos* 5 (2009), pp. 94–100 (cit. on p. 38).

[89] Hsiang-Chun Hsueh, Jae Hyun Kim, Sara Orski, Andrew Fairbrother, Deborah Jacobs, Lakesha Perry, Donald Hunston, Christopher White, and Lipiin Sung. «Micro and macroscopic mechanical behaviors of high-density polyethylene under UV irradiation and temperature». In: *Polymer degradation and stability* 174 (2020), p. 109098 (cit. on p. 43).

[90] Andreia C Tavares, Joseane V Gulmine, Carlos M Lepienski, and Leni Akcelrud. «The effect of accelerated aging on the surface mechanical properties of polyethylene». In: *Polymer Degradation and Stability* 81.2 (2003), pp. 367–373 (cit. on p. 43).

[91] JV Gulmine, PR Janissek, HM Heise, and L Akcelrud. «Degradation profile of polyethylene after artificial accelerated weathering». In: *Polymer degradation and stability* 79.3 (2003), pp. 385–397 (cit. on p. 43).

[92] X Han and J Pans. *The effective diffusion coefficient of degrading polymers*. Woodhead Publishing: Cambridge, UK, 2015 (cit. on p. 44).

[93] MA Pereira, OC Pires, M Mota, and MM16136588 Alves. «Anaerobic biodegradation of oleic and palmitic acids: evidence of mass transfer limitations caused by long chain fatty acid accumulation onto the anaerobic sludge». In: *Biotechnology and bioengineering* 92.1 (2005), pp. 15–23 (cit. on p. 44).

[94] Dennis Kopljar. «Development and investigation of gas-diffusion electrodes for the electrochemical reduction of CO2». PhD thesis. Dissertation, Stuttgart¦ Universität Stuttgart, 2023, 2023 (cit. on p. 44).

[95] EG Prout and Frederick C Tompkins. «The thermal decomposition of potassium permanganate». In: *Transactions of the Faraday Society* 40 (1944), pp. 488–498 (cit. on p. 47).

[96] Andrew Knox Galwey and Michael E Brown. *Thermal decomposition of ionic solids: chemical properties and reactivities of ionic crystalline phases*. Vol. 86. Elsevier, 1999 (cit. on p. 47).

[97] Octave Levenspiel. *Chemical reaction engineering*. John wiley & sons, 1998 (cit. on p. 49).

[98] N Khelidj, X Colin, L Audouin, and J Verdu. «Oxidation of polyethylene under irradiation at low temperature and low dose rate. Part II. Generalization of the kinetic model». In: *Polymer Degradation and Stability* 91.7 (2006), pp. 1598–1605 (cit. on p. 51).

[99] Erastus H Lee. «Elastic-plastic deformation at finite strains». In: (1969) (cit. on p. 54).

[100] Stefanie Reese and Sanjay Govindjee. «A theory of finite viscoelasticity and numerical aspects». In: *International journal of solids and structures* 35.26-27 (1998), pp. 3455–3482 (cit. on p. 54).

[101] Jorgen S Bergström and Mary C Boyce. «Constitutive modeling of the large strain time-dependent behavior of elastomers». In: *Journal of the Mechanics and Physics of Solids* 46.5 (1998), pp. 931–954 (cit. on pp. 54, 62).

[102] Shawn A Chester and Lallit Anand. «A coupled theory of fluid permeation and large deformations for elastomeric materials». In: *Journal of the Mechanics and Physics of Solids* 58.11 (2010), pp. 1879–1906 (cit. on p. 55).

[103] Shawn A Chester. «A constitutive model for coupled fluid permeation and large viscoelastic deformation in polymeric gels». In: *Soft Matter* 8.31 (2012), pp. 8223–8233 (cit. on p. 55).

[104] Shawn A Chester and Lallit Anand. «A thermo-mechanically coupled theory for fluid permeation in elastomeric materials: application to thermally responsive gels». In: *Journal of the Mechanics and Physics of Solids* 59.10 (2011), pp. 1978–2006 (cit. on p. 55).

[105] Mostafa Baghani, Reza Naghdabadi, Jamal Arghavani, and Saeed Sohrabpour¦ «A thermodynamically-consistent 3 D constitutive model for shape memory polymers». In: *International Journal of Plasticity* 35 (2012), pp. 13–30 (cit. on p. 55).

[106] Haedong Park, Philip Harrison, Zaoyang Guo, Myoung-Gue Lee, and Woong-Ryeol Yu. «Three-dimensional constitutive model for shape memory polymers using multiplicative decomposition of the deformation gradient and shape memory strains». In: *Mechanics of Materials* 93 (2016), pp. 43–62 (cit. on p. 55).

[107] Yunxin Li, Yuhao He, and Zishun Liu. «A viscoelastic constitutive model for shape memory polymers based on multiplicative decompositions of the deformation gradient». In: *International Journal of Plasticity* 91 (2017), pp. 300–317 (cit. on p. 55).

[108] Yiheng Xue, Jincheng Lei, and Zishun Liu. «A thermodynamic constitutive model for shape memory polymers based on phase transition». In: *Polymer* 243 (2022), p. 124623 (cit. on p. 55).

[109] L Rezaei, G Scalet, M Peigney, and A Azoug. «Coupling between viscoelasticity and soft elasticity in main-chain nematic Liquid Crystal Elastomers». In: *Journal of the Mechanics and Physics of Solids* 187 (2024), p. 105612 (cit. on p. 55).

[110] Haohui Zhang and Yuhang Hu. «A constitutive model that couples light propagation direction and deformation for photo-responsive polymers and polymeric gels». In: *Journal of the Mechanics and Physics of Solids* 191 (2024), p. 105786 (cit. on p. 55).

[111] Suming Li. «Hydrolytic degradation characteristics of aliphatic polyesters derived from lactic and glycolic acids». In: *Journal of Biomedical Materials Research: An Official Journal of The Society for Biomaterials, The Japanese Society for Biomaterials, and The Australian Society for Biomaterials* 48.3 (1999), pp. 342–353 (cit. on p. 55).

[112] Moataz A Elsawy, Ki-Hyun Kim, Jae-Woo Park, and Akash Deep. «Hydrolytic degradation of polylactic acid (PLA) and its composites». In: *Renewable and Sustainable Energy Reviews* 79 (2017), pp. 1346–1352 (cit. on p. 55).

[113] André C Vieira, Rui M Guedes, and Volnei Tita. «Constitutive modeling of biodegradable polymers: Hydrolytic degradation and time-dependent behavior». In: *International Journal of Solids and Structures* 51.5 (2014), pp. 1164–1174 (cit. on p. 55).

[114] Marco Gigliotti, Loic Olivier, Dinh Quy Vu, Jean-Claude Grandidier, and Marie Christine Lafarie-Frenot. «Local shrinkage and stress induced by thermo-oxidation in composite materials at high temperatures». In: *Journal of the Mechanics and Physics of Solids* 59.3 (2011), pp. 696–712 (cit. on p. 55).

[115] K Chrissafis. «Kinetics of thermal degradation of polymers: complementary use of isoconversional and model-fitting methods». In: *Journal of Thermal Analysis and Calorimetry* 95.1 (2009), pp. 273–283 (cit. on p. 55).

[116] S Belbachir, Fahmi Zaıri, Georges Ayoub, Ulrich Maschke, Moussa Naıt-Abdelaziz, Jean Michel Gloaguen, M Benguediab, and Jean Marc Lefebvre. «Modelling of photodegradation effect on elastic–viscoplastic behaviour of amorphous polylactic acid films». In: *Journal of the Mechanics and Physics of Solids* 58.2 (2010), pp. 241–255 (cit. on p. 55).

[117] Georges Ayoub, AK Rodriguez, B Mansoor, and Xavier Colin. «Modeling the visco-hyperelastic–viscoplastic behavior of photodegraded semi-crystalline low-density polyethylene films». In: *International Journal of Solids and Structures* 204 (2020), pp. 187–198 (cit. on p. 55).

[118] Sharif Alazhary, Mamoon Shaafaey, Hamid Mohammadi, and Roozbeh Dargazany. «Investigation of thermo-oxidative aging of silicone-based adhesives: substantiating separability between environmental and mechanical damages». In: *Journal of Polymer Research* 30.1 (2023), p. 16 (cit. on p. 55).

[119] Clifford Truesdell and Richard Toupin. «The classical field theories». In: *Principles of classical mechanics and field theory/Prinzipien der Klassischen Mechanik und Feldtheorie*. Springer, 1960, pp. 226–858 (cit. on p. 55).

[120] Rong Long, H Jerry Qi, and Martin L Dunn. «Thermodynamics and mechanics of photochemcially reacting polymers». In: *Journal of the Mechanics and Physics of Solids* 61.11 (2013), pp. 2212–2239 (cit. on p. 55).

[121] A Salvadori, R McMeeking, D Grazioli, and M Magri. «A coupled model of transport-reaction-mechanics with trapping. Part I–Small strain analysis». In: *Journal of the Mechanics and Physics of Solids* 114 (2018), pp. 1–30 (cit. on p. 55).

[122] Matteo Arricca, Luigi Cabras, Mattia Serpelloni, Claudia Bonanno, Robert M McMeeking, and Alberto Salvadori. «A coupled model of transport-reaction-mechanics with trapping, Part II: Large strain analysis». In: *Journal of the Mechanics and Physics of Solids* 181 (2023), p. 105425 (cit. on p. 55).

[123] Kristofer K Westbrook, Philip H Kao, Francisco Castro, Yifu Ding, and H Jerry Qi. «A 3D finite deformation constitutive model for amorphous shape memory polymers: a multi-branch modeling approach for nonequilibrium relaxation processes». In: *Mechanics of Materials* 43.12 (2011), pp. 853–869 (cit. on p. 55).

[124] Trisha Sain, Kaspar Loeffel, and Shawn Chester. «A thermo–chemo–mechanically coupled constitutive model for curing of glassy polymers». In: *Journal of the Mechanics and Physics of Solids* 116 (2018), pp. 267–289 (cit. on p. 56).

[125] Farhad Kamarei, Evan Breedlove, and Oscar Lopez-Pamies. «Nucleation and propagation of fracture in viscoelastic elastomers: A complete phase-field theory». In: *arXiv preprint arXiv:2506.16479* (2025) (cit. on pp. 56, 58, 60, 61).

[126] Kim Pham, Hanen Amor, Jean-Jacques Marigo, and Corrado Maurini. «Gradient damage models and their use to approximate brittle fracture». In: *International Journal of Damage Mechanics* 20.4 (2011), pp. 618–652 (cit. on p. 57).

[127] Oscar Lopez-Pamies. «A new I1-based hyperelastic model for rubber elastic materials». In: *Comptes Rendus Mecanique* 338.1 (2010), pp. 3–11 (cit. on pp. 58, 62, 66, 67).

[128] Bernard D Coleman and Morton E Gurtin. «Thermodynamics with internal state variables». In: *The journal of chemical physics* 47.2 (1967), pp. 597–613 (cit. on p. 58).

[129] Hans Ziegler and Christoph Wehrli. «The derivation of constitutive relations from the free energy and the dissipation function». In: *Advances in applied mechanics* 25 (1987), pp. 183–238 (cit. on p. 58).

[130] Aditya Kumar and Oscar Lopez-Pamies. «On the two-potential constitutive modeling of rubber viscoelastic materials». In: *Comptes Rendus Mecanique* 344.2 (2016), pp. 102–112 (cit. on pp. 58, 60, 67).

[131] Souhayl Sadik and Arash Yavari. «Nonlinear anisotropic viscoelasticity». In: *Journal of the Mechanics and Physics of Solids* 182 (2024), p. 105461 (cit. on p. 58).

[132] Masao Doi, Sam F Edwards, and Samuel Frederick Edwards. *The theory of polymer dynamics*. Vol. 73. oxford university press, 1988 (cit. on p. 62).

[133] Ellen M Arruda and Mary C Boyce. «A three-dimensional constitutive model for the large stretch behavior of rubber elastic materials». In: *Journal of the Mechanics and Physics of Solids* 41.2 (1993), pp. 389–412 (cit. on p. 62).

[134] Oon H Yeoh. «Some forms of the strain energy function for rubber». In: *Rubber Chemistry and technology* 66.5 (1993), pp. 754–771 (cit. on p. 66).

[135] Dirk Willem Van Krevelen and Klaas Te Nijenhuis. *Properties of polymers: their correlation with chemical structure; their numerical estimation and prediction from additive group contributions*. Elsevier, 2009 (cit. on p. 68).

[136] Bryan Ellis and Ray Smith. *Polymers: a property database*. CRC press, 2008 (cit. on p. 68).

[137] Irvin M Krieger, Thomas J Dougherty, et al. «A mechanism for non-Newtonian flow in suspensions of rigid spheres». In: *Trans. Soc. Rheol* 3.1 (1959), pp. 137–152 (cit. on p. 70).

[138] Leslie H Sperling. *Introduction to physical polymer science*. John Wiley & Sons, 2015 (cit. on p. 70).

[139] Melvin Mooney. «The viscosity of a concentrated suspension of spherical particles». In: *Journal of colloid science* 6.2 (1951), pp. 162–170 (cit. on p. 70).

[140] Albert Einstein. «Eine neue bestimmung der moleküldimensionen». PhD thesis. ETH Zurich, 1905 (cit. on p. 70).

[141] Graham J Lake and Allen G Thomas. «The strength of highly elastic materials». In: *Proceedings of the Royal Society of London. Series A. Mathematical and Physical Sciences* 300.1460 (1967), pp. 108–119 (cit. on pp. 71, 72).

[142] Martin Kroon, Eskil Andreasson, Viktor Petersson, and Pär AT Olsson. «Experimental and numerical assessment of the work of fracture in injection-moulded low-density polyethylene». In: *Engineering Fracture Mechanics* 192 (2018), pp. 1–11 (cit. on p. 71).

[143] E Grossman and I Gouzman. «Space environment effects on polymers in low earth orbit». In: *Nuclear Instruments and Methods in Physics Research Section B: Beam Interactions with Materials and Atoms* 208 (2003), pp. 48–57 (cit. on pp. 80–82).

[144] Peiyi Tong, Qiang Wei, Ning Hu, and Xueguang Chen. «Asynchronous synergistic damage effect of atomic oxygen and space micro debris on Kapton film». In: *Coatings* 12.2 (2022), p. 179 (cit. on pp. 80, 81).

[145] Laiwen Chen, Zongchen Li, Chun-Hian Lee, and Wang Jiahong. «Unified model for low-Earth-orbital atomic-oxygen and atomic-oxygen/ultraviolet induced erosion of polymeric materials». In: *Aerospace Science and Technology* 53 (2016), pp. 194–206 (cit. on pp. 81, 92, 94).

[146] William H Kinard and Glenna D Martin. «Long duration exposure facility (LDEF) space environments overview». In: *LDEF: 69 Months in Space. First Post-Retrieval Symposium, Part 1*. 1992 (cit. on p. 81).

[147] Kim K deGroh, Joyce A Dever, Donald A Jaworske, Sharon K Miller, Edward A Sechkar, Scott R Panko, et al. «NASA Glenn research center's materials international space station experiments (MISSE 1-7)». In: *International Symposium on SM/MPAC and SEED Experiments*. E-16690. 2008 (cit. on p. 81).

[148] Bruce A Banks, Kim K de Groh, and Sharon K Miller. «Low earth orbital atomic oxygen interactions with spacecraft materials». In: *MRS Online Proceedings Library (OPL)* 851 (2004), NN8–1 (cit. on pp. 82, 107).

[149] Bruce A Banks, Kim K De Groh, Sharon K Rutledge, and Frank J DiFilippo. «Prediction of in-space durability of protected polymers based on ground laboratory thermal energy atomic oxygen». In: *Protection of Materials and Structures from the Low Earth Orbit Space Environment: Proceedings of ICPMSE-3, Third International Space Conference, held in Toronto, Canada, April 25–26, 1996*. Springer. 1999, pp. 89–100 (cit. on pp. 82, 107).

[150] Timothy K Minton et al. «Atomic oxygen effects on POSS polyimides in low earth orbit». In: *ACS applied materials & interfaces* 4.2 (2012), pp. 492–502 (cit. on pp. 82, 86, 89, 90, 106, 107).

[151] René I Gonzalez, Shawn H Phillips, and Gar B Hoflund. «In situ oxygen-atom erosion resistance of polyhedral oligomeric silsesquioxane-siloxane copolymers». In: *Journal of Spacecraft and Rockets* 37.4 (2000), pp. 463–467 (cit. on p. 82).

[152] Sandra J Tomczak, Vandana Vij, Timothy K Minton, Amy L Brunsvold, Darrell Marchant, Michael E Wright, Brian J Petteys, Andrew J Guenthner, and Yandek GR. «POSS polyimides for protection against atomic oxygen erosion». In: *Proceedings of the 10th International Symposium on Materials in a Space Environment*. ESA SP-589. 2005, pp. 19–23 (cit. on pp. 82, 91).

[153] Daniel Khan, Youngjong Cho, Jung Ryul Lee, Hyosang Yoon, Gisu Park, and Jae Gang Kim. «Experimental erosion analysis and computational modeling of SiOx-coated polyimide in atomic oxygen under super-low-Earth-orbit conditions». In: *Aerospace Science and Technology* (2025), p. 110611 (cit. on p. 85).

[154] Masahito Tagawa, Kumiko Yokota, Jorg Heiermann, and Hiroshi Kinoshita. «Monte Carlo simulation of atomic oxygen interactions with coated polymers used in low Earth orbit». In: *Journal of Spacecraft and Rockets* 41.3 (2004), pp. 435–440 (cit. on pp. 85, 91).

[155] Kim K de Groh and Bruce A Banks. «Atomic oxygen undercutting of coatings on polymers used for spacecraft components». In: *Proceedings of the 10th International Symposium on Materials in a Space Environment*. Vol. 1. ESA SP-662. 2008, pp. 15–20 (cit. on p. 86).

[156] Bruce A Banks, Aaron Snyder, Sharon K Miller, Kim K De Groh, and Rikako Demko. «Atomic-oxygen undercutting of protected polymers in low earth orbit». In: *Journal of spacecraft and rockets* 41.3 (2004), pp. 335–339 (cit. on pp. 86, 94).

[157] Amy L Brunsvold, Timothy K Minton, Irina Gouzman, Eitan Grossman, and Rene I Gonzalez. «An investigation of the resistance of POSS polyimide to atomic oxygen attack». In: *Materials in a Space Environment*. Vol. 540. 2003, pp. 153–158 (cit. on p. 86).

[158] Bruce E Deal and AS Grove. «General relationship for the thermal oxidation of silicon». In: *Journal of applied physics* 36.12 (1965), pp. 3770–3778 (cit. on pp. 87, 94, 97, 102).

[159] David B Cordes, Paul D Lickiss, and Franck Rataboul. «Recent developments in the chemistry of cubic polyhedral oligosilsesquioxanes». In: *Chemical reviews* 110.4 (2010), pp. 2081–2173 (cit. on p. 88).

[160] Joseph D Lichtenhan, Yoshiko A Otonari, and Michael J Carr. «Linear hybrid polymer building blocks: methacrylate-functionalized polyhedral oligomeric silsesquioxane monomers and polymers». In: *Macromolecules* 28.24 (1995), pp. 8435–8437 (cit. on p. 88).

[161] Shawn H Phillips, Timothy S Haddad, and Sandra J Tomczak. «Developments in nanoscience: polyhedral oligomeric silsesquioxane (POSS)-polymers». In: *Current Opinion in Solid State and Materials Science* 8.1 (2004), pp. 21–29 (cit. on p. 88).

[162] Shouming Wu, Teruaki Hayakawa, Ryohei Kikuchi, Stephen J Grunzinger, Masa-aki Kakimoto, and Hisao Oikawa. «Synthesis and characterization of semiaromatic polyimides containing POSS in main chain derived from double-decker-shaped silsesquioxane». In: *Macromolecules* 40.16 (2007), pp. 5698–5705 (cit. on p. 88).

[163] R Verker, E Grossman, and N Eliaz. «Erosion of POSS-polyimide films under hypervelocity impact and atomic oxygen: The role of mechanical properties at elevated temperatures». In: *Acta Materialia* 57.4 (2009), pp. 1112–1119 (cit. on p. 91).

[164] Hiroyuki Shimamura and Takashi Nakamura. «Mechanical properties degradation of polyimide films irradiated by atomic oxygen». In: *Polymer Degradation and Stability* 94.9 (2009), pp. 1389–1396 (cit. on p. 91).

[165] Dahai Wei, Fanlin Zeng, and Jianzheng Cui. «Damage and degradation of mechanical properties of polyimide-based materials under atomic oxygen attack: A molecular dynamics simulation study». In: *Computational Materials Science* 243 (2024), p. 113110 (cit. on p. 91).

[166] Shengrui Zhou, Li Zhang, Liang Zou, Bilal Iqbal Ayubi, and Yiwei Wang. «Mechanisms of Atomic Oxygen Erosion in Fluorinated Polyimides Investigated by Molecular Dynamics Simulations». In: *Molecules* 29.18 (2024), p. 4485 (cit. on p. 91).

[167] Masahito Tagawa, Kumiko Yokota, Kazuhiro Kishida, Akio Okamoto, and Timothy K Minton. «Energy dependence of hyperthermal oxygen atom erosion of a fluorocarbon polymer: relevance to space environmental effects». In: *ACS Applied Materials & Interfaces* 2.7 (2010), pp. 1866–1871 (cit. on p. 91).

[168] Guohui Li, Xue Liu, and Tao Li. «Effects of low earth orbit environments on atomic oxygen undercutting of spacecraft polymer films». In: *Composites Part B: Engineering* 44.1 (2013), pp. 60–66 (cit. on p. 91).

[169] James K Baird, H Li, and H Paik. «Low-Earth-orbit atomic oxygen erosion of polymer surfaces». In: *Journal of Spacecraft and Rockets* 35.1 (1998), pp. 62–65 (cit. on p. 94).

[170] Francis J Norton. «Permeation of gaseous oxygen through vitreous silica». In: *Nature* 191.4789 (1961), pp. 701–701 (cit. on p. 94).

[171] John Crank. *The mathematics of diffusion*. Oxford university press, 1979 (cit. on p. 94).

[172] Lawrence E Nielsen. «Models for the permeability of filled polymer systems». In: *Journal of Macromolecular Science—Chemistry* 1.5 (1967), pp. 929–942 (cit. on pp. 96, 103).

[173] E. L. Cussler, S. E. Hughes, W. J. Ward III, and R. Aris. «Barrier membranes». In: *Journal of Membrane Science* 38.2 (1988), pp. 161–174 (cit. on p. 96).

[174] John Crank. «Free and moving boundary problems». In: *(No Title)* (1984) (cit. on p. 97).

[175] Ulick Richardson Evans. *The Corrosion and Oxidation of Metals: Scientific Principles and Practical Applications*. London: Edward Arnold, 1960 (cit. on p. 102).

[176] Dietrich Stauffer and Ammon Aharony. *Introduction to percolation theory*. Taylor & Francis, 2018 (cit. on p. 103).

[177] Scott Kirkpatrick. «Percolation and conduction». In: *Reviews of modern physics* 45.4 (1973), p. 574 (cit. on p. 103).

[178] John W Essam. «Percolation theory». In: *Reports on progress in physics* 43.7 (1980), p. 833 (cit. on p. 105).

[179] Hiroshi Fujita. «Diffusion in polymer-diluent systems». In: *Fortschritte Der Hochpolymeren-Forschung*. Springer, 2006, pp. 1–47 (cit. on pp. 105, 106).

[180] Morrel H Cohen and David Turnbull. «Molecular transport in liquids and glasses». In: *The Journal of Chemical Physics* 31.5 (1959), pp. 1164–1169 (cit. on pp. 105, 106).

[181] DR Paul and WJ Koros. «Effect of heat treatment on the physical properties of a series of polyimides». In: *Journal of Polymer Science: Polymer Physics Edition* 11 (1973) (cit. on p. 105).

[182] Ronen Verker, Eitan Grossman, Irina Gouzman, and Noam Eliaz. «Residual stress effect on degradation of polyimide under simulated hypervelocity space debris and atomic oxygen». In: *Polymer* 48.1 (2007), pp. 19–24 (cit. on p. 106).

[183] Masahito Tagawa and Timothy K Minton. «Mechanistic studies of atomic oxygen reactions with polymers and combined effects with vacuum ultraviolet light». In: *MRS bulletin* 35.1 (2010), pp. 35–40 (cit. on p. 106).

[184] Min Qian, Vanessa J Murray, Wei Wei, Brooks C Marshall, and Timothy K Minton. «Resistance of POSS polyimide blends to hyperthermal atomic oxygen attack». In: *ACS Applied Materials & Interfaces* 8.49 (2016), pp. 33982–33992 (cit. on pp. 109, 114, 115).